UNIVERSITY OF OKLAHOMA

GRADUATE COLLEGE

INTEGRATED CHARACTERIZATION OF THE WOODFORD SHALE IN WEST-CENTRAL OKLAHOMA

A DISSERTATION

SUBMITTED TO THE GRADUATE FACULTY

in partial fulfillment of the requirements for the

Degree of

DOCTOR OF PHILOSOPHY

By

NABANITA GUPTA
Norman, Oklahoma
2012

Table of contents

List of tables

List of figures

Abstract/Introduction

This dissertation focuses on the characterization of unconventional resource-shales for resource evaluation. I have used the Woodford Shale as a primary example for this study. Complex nature or the resource shales and limited understanding about the actual rock properties with field measurements demand integrated characterization of these rocks at multiple scales. In this research, I present a fully integrated characterization including petrophysical, geophysical and geological evaluation of the Woodford Shale in West Central Oklahoma, which opens new facts for understanding this shale as well as other resource shales. I have used a multi-scale dataset collected from multiple sources and ranging from nano-meter scale image analysis through scanning electron microscopic observations, microscopic observations made through petrographic microscope, macroscopic visual observations, laboratory measured petrophysical parameters, well-logs, to surface seismic data for regional characterization.

With growing energy demand and technology advancement, resource-shales are emerging as one of the primary areas for hydrocarbon exploration. Petrophysical properties characterize both physical and mechanical properties and hence, are important for identifying sweet-spots for hydrocarbon exploration. This study attempts to do petrophysical characterization of the Woodford Shale based on petrophysical measurements made on about 300 samples collected from 6 wells located in both hydrocarbon producing and non-producing areas. Crushed rock porosity, bulk density, grain density, mineralogy, acoustic velocities, mercury injection capillary pressure along with total organic carbon content, rock-eval pyrolysis, and Vitrinite reflectance were

measured at the Integrated Core Characterization Center. NMR measurements were made on few samples to track distribution of different fluids in the pore spaces. Visual inspections were made at macroscopic-, microscopic- and scanning electron microscope-scale in order to calibrate rock-petrophysical properties with the actual rock architecture. Wide range of porosity from 1% to 10% indicates different rock types with variable storage capacity. Mineralogy data indicates that the Woodford is a silica-dominated silty shale with small amount of carbonate. Rock-eval analyses indicated that the Woodford Shale in two of the studied well are in the oil window (Ro< 1%) and in rest of the wells are in Dry gas-condensate window (Ro>1.2%). Wells from different maturity provided me an opportunity to analyze changes in petrophysical properties with the changes in thermal maturity. Laboratory measured petrophysical properties were finally analyzed through cluster analyses in order to identify three rock-types characterized by unique reservoir properties.

A set of seismic attributes help to illuminate both stratigraphic and structural features present within the Woodford interval in a regional scale. I used both conventional and recently developed seismic attributes in this study. Petrophysical properties extracted through simultaneous inversion of the pre-stack seismic data allowed me to perform regional characterization of the Woodford Shale in a semi-quantitative manner. Rock types identified through the petrophysical characterization in the previous section were combined with geophysical analyses to build a regional distribution of each rock type. Finally, seismic attributes, production data along with the geologic history indicate that the basin floor depressions are good areas for ductile-brittle rock couplet

containing both hydrocarbon rich intervals and brittle rocks and thus are identified as potential sweet spots in the Woodford Shale.

Detailed analyses of macroscopic, microscopic and submicroscopic sedimentary features combined with the regional geologic history allowed me to build the depositional framework and associated lithofacies distribution for the Woodford Shale in the Anadarko Basin. Petrophysical measurements made on samples collected from each lithofacies present in 6 wells allowed me to correlate petrophysical properties with the geologic framework and identify petrophysical proxies that can be used to track stratigraphic changes especially in the uncored areas. This study reveals that the mineralogy is one of the important tools for tracking the geologic history. Since, mineralogy correlates well with other petrophysical properties it is possible to reasonably predict petrophysical properties of the Woodford Shale based on the geologic framework and vice versa.

Chapter 1

Integrated petrophysical characterization of the Woodford Shale in Oklahoma

Abstract

Heterogeneity of the resource-shale plays and limited knowledge about the shale petrophysical properties demand detailed core-scale characterization in order to understand field-scale measurements that have poor vertical resolution. Analyses of a set of laboratory measured petrophysical properties collected on 300 samples of the Woodford Shale from 6 wells provided an opportunity to track changes in petrophysical properties in response to thermal maturity and their effect on hydrocarbon production. Porosity, bulk density, grain density, mineralogy, acoustic velocities (V_p-fast, V_s-fast and V_s-slow), mercury injection capillary pressure along with total organic carbon content (TOC), Rock-Eval pyrolysis, and vitrinite reflectance were measured. Visual inspections were made at macroscopic-, microscopic- and scanning electron microscope-scale (SEM) in order to calibrate rock-petrophysical properties with the actual rock architecture. Mineralogically, the Woodford Shale is a silica-dominated system with very little carbonate presence. Crossplot of porosity and TOC clearly separate the lower thermal maturity (oil window) samples from higher thermal maturity (wet gas-condensate window) as porosity is lower at lower thermal maturity. Independent observations made through SEM-imaging confirm much lower organic porosity at lower thermal maturity

while organic pores are the dominant pore types in all samples irrespective of thermal maturity. Crack-like pores are only observed at the oil window.

Cluster analyses of TOC, porosity, clay and quartz content revealed three clusters of rocks which could be ranked as good, intermediate and poor in terms of reservoir quality. Good correlations between different petro-types with geological core descriptions, along with the good conformance between different petro-types with production data ascertain the practical applicability of such petro-typing. Petro-types can be upscaled and applied to the uncored interval through calibrating well logs with core measurements. However, limited well-log analyses were performed due to unavailability of field-data.

Introduction

The Woodford Shale has long been known as the source of most of Oklahoma's hydrocarbon reserves until it emerged as resource play following the huge success of the Barnett Shale play in 2005. Geographically the Woodford Shale play can be grouped into 3 regions: Woodford, Cana-Woodford of the Midwest and Barnett Woodford of the Southwest, with estimated technically recoverable resource as 22.21 TCF, 5.72 TCF and 32.15 TCF respectively (EIA, 2011). This study focuses on an area in the Midwest where the shale is reported to produce dry gas, condensate as well as oil and have an average thickness of 200ft.

Despite of the economic success, variability in petrophysical parameters controlling reservoir quality is poorly understood and hence, the exploration activities rely heavily on the history matching. This limits the identification of new sweet spots and

also expansion of exploration activities outside the proven area. Moreover, unlike conventional hydrocarbon prospects, resource-shales serve as the source, seal, and reservoir at the same time, which makes it difficult to identify or rather, define the reservoir unit within this shale. Appropriate petrophysical characterization leads to identification of different rock types with unique petrophysical properties, which eventually help to identify sweet spots and to decide appropriate areas for well placement. As production from these shales requires stimulation through hydraulic fracturing, appropriate petrophysical model would help to predict hydrocarbon reserve as well as areas/intervals with high fracability.

Centimeter-scale vertical heterogeneity of resource-shales limits the use of field-scale measurements and misrepresents the petrophysical characterization of such shales to some extent. Petrophysical characterization based on measured petrophysical properties from representative samples of individual litho/petro-type helps to identify and estimate the range of values for parameters which correlates well with reservoir evaluation attributes such as, gas-in-place and fracability- the two important parameters for the resource-shales. Such laboratory-measurements based analyses require a large data-set, which makes the resource-shale characterization time intensive but still are required for the evaluation of resource-shales.

Swanson (1981), Thomeer (1960; 1983), Amaefule et al. (1993) etc. have developed and successfully applied different rock typing principles to the conventional reservoirs. All of these rock-typing principles are based on the dynamic range of porosity, permeability and variations in their inter-relationships present in the conventional reservoirs. None of these rock-typing principles can be applied to the resource-shales due

to narrow range of porosity and nanodarcy permeability, which are few orders of magnitude smaller than even tight gas sands (Sondergeld et al., 2010). Moreover, it is also difficult either to measure such low permeability or to estimate permeability from porosity-permeability relationship previously observed by Swanson (1981), Thomeer (1960, 1983) etc.. Klinkenberg correction becomes significant at this low permeability, which lead to the erroneous estimation of permeability (Kamath, 1992). Gunter et al. (1997) defined rock types as 'units of rocks deposited under similar geological conditions, undergone similar digenetic processes resulting in unique porosity – permeability relationships, capillary pressure profile and water saturations above free water'. Such rock types are unique geologically and petrophysically and ideally helpful in delineating good reservoir rocks from poor for any kind of reservoir rocks. However, it still relies heavily upon porosity and permeability, which limits its use for the resource-shales.

Despite of all the difficulty, rock typing can be an important tool for the evaluation of resource-shales if the rock types can capture subtle differences in petrophysical properties that may influence production. Sondergeld et al. (2010) documented a set of petrophysical properties (rock composition, total organic carbon content, porosity, saturation, permeability and mechanical properties) impacting the performances of resource-shales. Newsham and Rushing (2001) tried to follow the rock typing principles of Gunter et al. (1997) and proposed a specialized workflow for the evaluation of unconventional reservoir and applied that for the evaluation of tight-gas sandstone; the workflow is named it as "modified PIPM". They defined rock-types in three ways, such as: depositional, petrographic and hydraulic. This rock typing workflow

has limited practical applicability, as it is difficult to correlate these three rock types with one another. Jacobi et al. (2008) proposed a workflow for integrated petrophysical evaluation of shale gas reservoirs; they called it as "expert system". This workflow is focused on the petrophysical evaluation based on well logs and used limited core data, which may not work always, owing to the high variability typical of resource shales. Kale (2009) proposed a core measurement based rock typing workflow for the Barnett Shale. Passey et al. (2010) made an effort to integrate petrophysical and geological characterization of resource shales.

Workflow for the evaluation of resource-shales

Quality reservoir description for the resource-shale system can be built by integrating multi-scale information collected from core, well logs, production data as well as seismic data. Gunter et al., 1997 proposed a three-step workflow for building reservoir description for the conventional reservoirs, which were helpful in identifying significant amount of bypass as well as new reserves. Three steps of this workflow are: (1) define rock types, (2) integrate rock type models with formation evaluation data to define reservoir compartments and flow units, and (3) ultimately use petrophysical models to calibrate seismic data and/or geostatistics in order to build a 3D reservoir descriptions. While these principal steps are also applicable for the evaluation of resource-shales, reservoir assessment for these rocks has to be summarized in a little different way. We can break it into three parts: (A) reservoir descriptions (both storage and flow capacity), (B) description of mechanical properties impacting hydraulic stimulation, and (C) integrating the reservoir description with mechanical properties for locating sweet spot.

Mechanical properties are important as hydrocarbon production from gas shales depend largely on the hydraulic fracturing. Each of these steps can be broken into three parts as mentioned by Gunter et al., 1997.

Reservoir descriptions can be built by starting with rock typing that characterize units of rocks with unique petrophysical properties those were deposited under similar geologic condition and experienced same diagenetic history. Geologic core description helps to build the fine-scale stratigraphy and choose the sampling intervals for laboratory measurements such that it covers all the lithologic changes. Rock-Eval analyses help to identify thermal maturity, S1, S2 and S3 peaks along with the hydrogen, oxygen and carbon concentration (TOC) within organic matter. This provides the background information about the organic matter that is the source of hydrocarbon in the self-sustained resource shale petroleum system. TOC and porosity are two parameters closely associated with reservoir storage capacity of resource shales. Clustering analyses of TOC, porosity, permeability along with parameters those are closely associated with TOC and porosity, and parameters with significant dynamic range can be used to group rocks into different units. Optimum clustering is achieved when the rock types identified at this step is supported by data from independent sources like rock types identified through capillary pressure experiment, and is characterized by unique set of properties identified through microscopic-scale observation, SEM imaging, geologic history. After identifying the rock types, petrophysical properties of the rock types are compared in order to locate best reservoir intervals. Mechanical characterization of the resource-shales is important as hydrocarbon production depends largely on the hydraulic fracturing. Factors like saturation of different fluid phases, wettability of the host rock, presence of natural

fractures also impact the reservoir flow properties and thus need to be considered for reservoir evaluation purposes. Reservoir description, mechanical characterization as well as rock typing can be performed at well-log scale through calibrating well logs with core measurements. Finally, 3D reservoir descriptions can be built calibrating seismic data with petrophysical models.

Study area

The Woodford Shale was deposited in the palaeo-Oklahoma Basin covered by an epeiric sea, during global sea-level transgression (Lambert, 1993; Johnson, 1988) (Figure 1). Different rock types are expected in different parts of the sea (horizontal variability) as well as in different stages of the transgression (vertical variability). Sub-surface cores collected from 6 wells located in both hydrocarbon producing and non-producing areas (approximately 1440 square miles) were used for this study (Figure 2). Thermal maturity of the Woodford Shale in wells 1, 2, 3, and 6 are within dry gas-condensate maturity window whereas wells 4 and 5 are within oil window. Samples are collected from ~200 feet long continuous cores acquired from wells 1 through 3. For well 4, 5, and 6 samples are collected from cores at discrete depth intervals.

About 300 core plugs are collected after careful visual inspection of the cores. Samples are collected at every 2-foot interval in apparently monotonous interval while intermittent samples are collected at places with visual-changes in lithology. At this point it is worth mentioning that sometime it is possible to miss some of the lithologic changes due to dark color of the rock. Sharp changes in petrophysical properties along with inspection of microscopic properties is used in tracking such significant but apparently invisible lithologic changes.

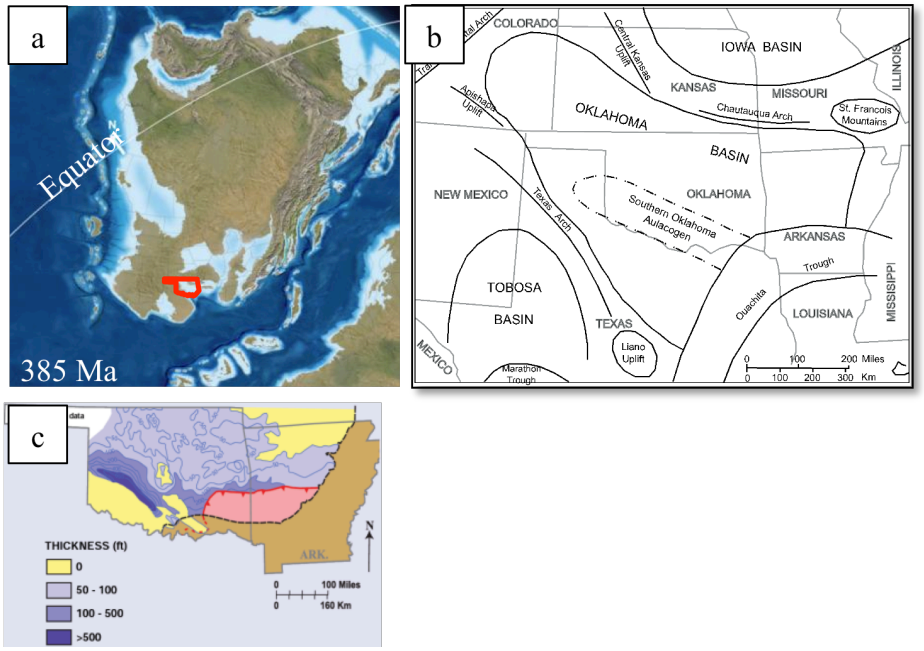

Figure 1: (a) Paleogeography of North America at the beginning of late Devonian (Frasnian). Paleo-location of Oklahoma is marked with red line. Figure is modified from Comer, 2008. (b) Location of the Oklahoma Basin covering a vast area of the Southern Midcontinent during Late Devonian-Early Mississippian time. Oklahoma Basin was later broken into a number of sub-basins due to tectonic activity. Map modified from Johnson, 1988. (c) Isochore map of the Woodford Shale in Oklahoma. Map modified from Comer, 2008.

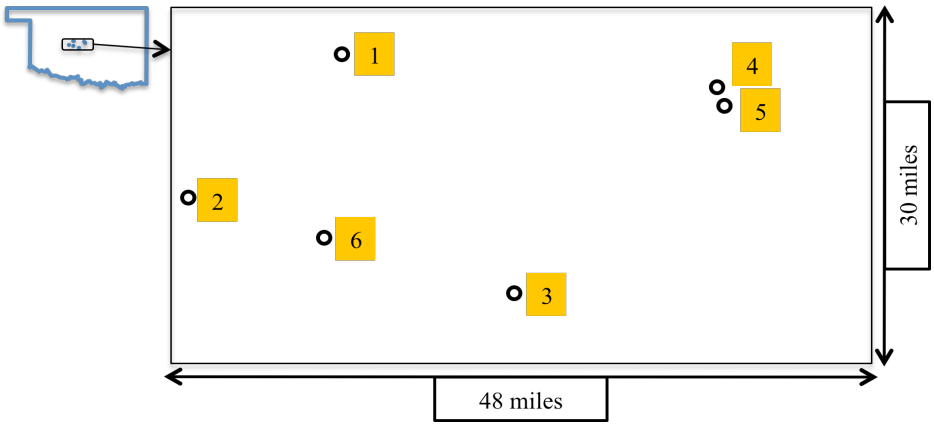

Figure 2: Location of the six colored wells considered in this study.

Laboratory Measurements

A set of petrophysical properties impacting two reservoir assessment categories such as storage capacity and flow capacity are measured: (i) crushed rock porosity (Φ_{He}), (ii) bulk density (ρ_b), (iii) grain density (ρ_g), (iv) mineralogy through Fourier Transform Infra-Red spectroscopy (FTIR), (v) acoustic velocities (V_p-fast, V_s-fast and V_s-slow), (vi) total organic carbon (TOC) content, (vii) Rock-Eval analyses and (viii) mercury injection capillary pressure (MICP) along with microscopic and sub-microscopic inspection of samples through (ix) petrographic microscopic analyses of thin sections, and (x) scanning electron microscopic (SEM) analyses of focused ion beam (FIB) milled samples. Nuclear magnetic resonance (NMR) measurements on few samples have been performed to gain knowledge about shale wettability. Most of these measurements are made at the Integrated Core Characterization Centre (IC^3) at the University of Oklahoma while the organic content (TOC) and Rock-Eval measurements are made at a commercial

laboratory. Dynamic elastic moduli calculated from ultrasonic acoustic velocities provide indirect estimates for rock-mechanical characteristics, which is another important parameter behind the success of resource-shales.

Detail descriptions of how the petrophysical properties are measured can be found in the following:

- $\Phi_{He,}$ ρ_b, and ρ_g in Karastathis (2007), Kale (2009)
- FTIR in Ballard (2007), Matteson and Herron (1993), and Sondergeld and Rai (1993)
- Ultrasonic velocities in Birch (1960), Raina (2010)
- MICP in Kale (2009)

Crushed rock porosity (Φ_{He}): Represent the effective porosity of shales and include the free and capillary bound pore spaces but exclude the spaces occupied by clay bound water.

FTIR mineralogy: The system is set up to identify sixteen common rock forming minerals which are grouped into 5 mineral groups as shown in Table 1.

Ultrasonic measurements: For the current study ultrasonic measurements are performed on horizontal plug. One compressional (V_p-fast) and two shear wave velocities (V_s-fast and V_s-slow) are measured, as shown on Figure 3. Core plugs are subjected to increasing confining pressure from 250 psi to 5000 psi in eight steps and ultrasonic data is collected at each step using ultrasonic pulse transmission technique.

Minerals	Mineral Groups
Quartz	Quartz
Albite	Total Feldspar
Orthoclase Feldspar	
Oligoclase Feldspar	
Calcite	Total Carbonates
Dolomite	
Siderite	
Aragonite	
Chlorite	Total Clays
Illite	
Smectite	
Kaolinite	
Mixed Clays	
Anhydrite	Others
Apatite	
Pyrite	

Table 1: Minerals identified in FTIR

MICP: Along with the capillary pressure, pore throat diameter can be calculated from this measurement, using Washburn equation. The formula states that "the pressure required to force a non-wetting liquid to enter a capillary is inversely proportional to the diameter of the capillary and directly proportional to the surface tension of the liquid and the contact angle with the solid surface". Mathematically it can be expressed as:

$$D=\frac{4\gamma k\cos\theta}{P_{cap}}$$

Where, P_{cap} = capillary pressure (psi), γ = interfacial tension of the non-wetting fluid (dyne/cm), k =0.145, and θ = contact angle (°) between the non-wetting fluid (mercury in this case) and the rock sample, D = pore throat diameter (μm). For mercury, γ = 480 dyne/cm, θ = 145°; hence, knowing the pressure at which intrusion takes place we can find out the pore throat radius. For example, at 60,000 psi mercury enters pores with throat diameters of 3 nm.

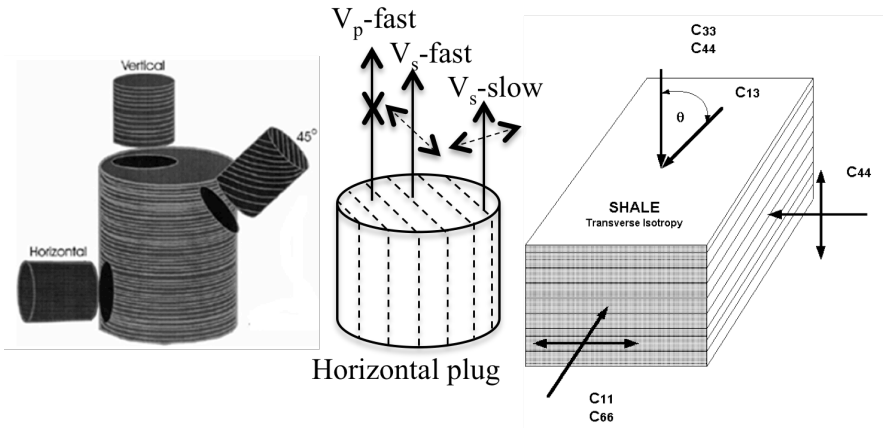

Figure 3: Schematic diagram showing the orientation of core plug. V_p-fast and V_s-fast are fast compressional and shear wave velocities. V_s-slow is the slow shear where the particle movement is perpendicular to the bedding and the wave is travelling parallel to the bedding. The schematic on the right shows the principal directions and the required elastic constants for anisotropic characterization of the shales.

Results

Table 2 summarizes the distribution of the laboratory measured petrophysical properties.

Porosity: Φ_{He} varies between 0% and 10% in the studied wells. Φ_{He} shows a normal distribution, especially when wells with high organic maturity are considered. Porosity of wells within oil window belongs to a different normal distribution. Φ_{He} ranges between 2% and 10% with 6% average in high maturity wells (wells 1, 2, 3, and 6), and ranges between 3% and 5% with 1.6 % average in wells within oil window (wells 4 and 5).

Density: Bulk density varies between 2.2g/cm^3 and 2.9g/cm^3 with 2.4g/cm^3 average. Grain density varies between 2.4g/cm^3 and 3g/cm^3 with 2.6g/cm^3 average.

Mineralogy: Figure 4 summarizes the distributions of 16 minerals as well as the distributions of 5 mineral groups mentioned earlier in Table 1. Individual mineral weight percentages from wells 1 through 6 located in different parts of the basin show overall narrow spread (Figure 4a, b) while quartz and illite show comparatively wider spread (Figure 4a). Despite of the narrow range of mineralogical concentrations, depth plot showing mineralogical variations with depth (Figure 4c) in wells 1 through 3 indicates distinct mineralogic characteristics of these wells. For example, well 3 has higher clay concentration compared to well 1 and 2, clay concentration decreases upward in well 2. Ternary plots indicate that the Woodford Shale is a silica-dominated system with <20% carbonate except few samples (Figure 5a). The highly calcareous samples are located near the boundary of the Woodford Shale and the underlying Hunton Limestone. Figure 5a also shows that wells 3 and 4 are more clayey compared to well 1 and 5 while well 2

has a wider range for clay concentration. Overall, Clay percentage varies between 20% and 70%. Clays are dominantly illite with some mixed clays and little to no kaolinite (Figure 5b). Dolomite and siderite are the dominant carbonate minerals with <40% calcite (Figure 5c). Two most dominate minerals: quartz and total clays are inversely proportional to each other (Figure 4d).

a

Properties	**Well 1**	**Well 2**	**Well 3**	**Well 4**	**Well 5**	**Well 6**
	No. of samples	No. of samples	No. of samples	No. of samples	No. of samples	No. of samples
Φ_{He}	85	17	76	9	11	2
ρ_b	85	17	76	9	11	2
ρ_g,	85	17	76	9	11	2
Mineralogy	85	17	76	9	11	2
Velocity	34	N/A	50	N/A	N/A	N/A
TOC	85	15	71	9	11	2
Rock Eval	85	15	37	9	11	2
MICP	45	16	47	6	5	2

Table 2: (a) Summarizes number of samples used for laboratory measurements, (b) Summary of laboratory measured petrophysical properties for the studied wells.

b

Properties		**Well 1**		**Well 2**		**Well 3**		**Well 4**		**Well 5**		**Well 6**	
		Range	Average	Range	Average	Range	Average	Range	Average	Range	Average	Range	Average
Φ_{He} (%)		4-8.5	6	3-8	6	4-8.5	6	0-4.3	3	2.5-5	3.4	6-8	7
ρ_b (g/cm^3)		2.2-2.65	2.4	2.33-2.7	2.52	2.2-2.7	2.43	2.35-2.54	2.45	2.33-2.45	2.4	2.55-2.56	2.56
ρ_g (g/cm^3)		2.4-3	2.56	2.5-2.8	2.67	2.4-3	2.59	2.39-2.6	2.5	2.39-2.56	2.45	2.69-2.76	2.72
Velocity (km/s)	Vp-fast	3.7-6.35	4.8	N/A	N/A	4-5.7	4.8	N/A	N/A	N/A	N/A	N/A	N/A
	Vs-fast	2.35-3.9	3.03	N/A	N/A	2.6-3.85	3	N/A	N/A	N/A	N/A	N/A	N/A
	Vs-slow	2.2-3.76	2.59	N/A	N/A	1.99-3.7	2.39	N/A	N/A	N/A	N/A	N/A	N/A
TOC (wt.%)		0-9	5.4	0-7.7	2.88	0-13	5.5	5.2-10	7.2	2.9-7	6	0.7-1.24	0.37

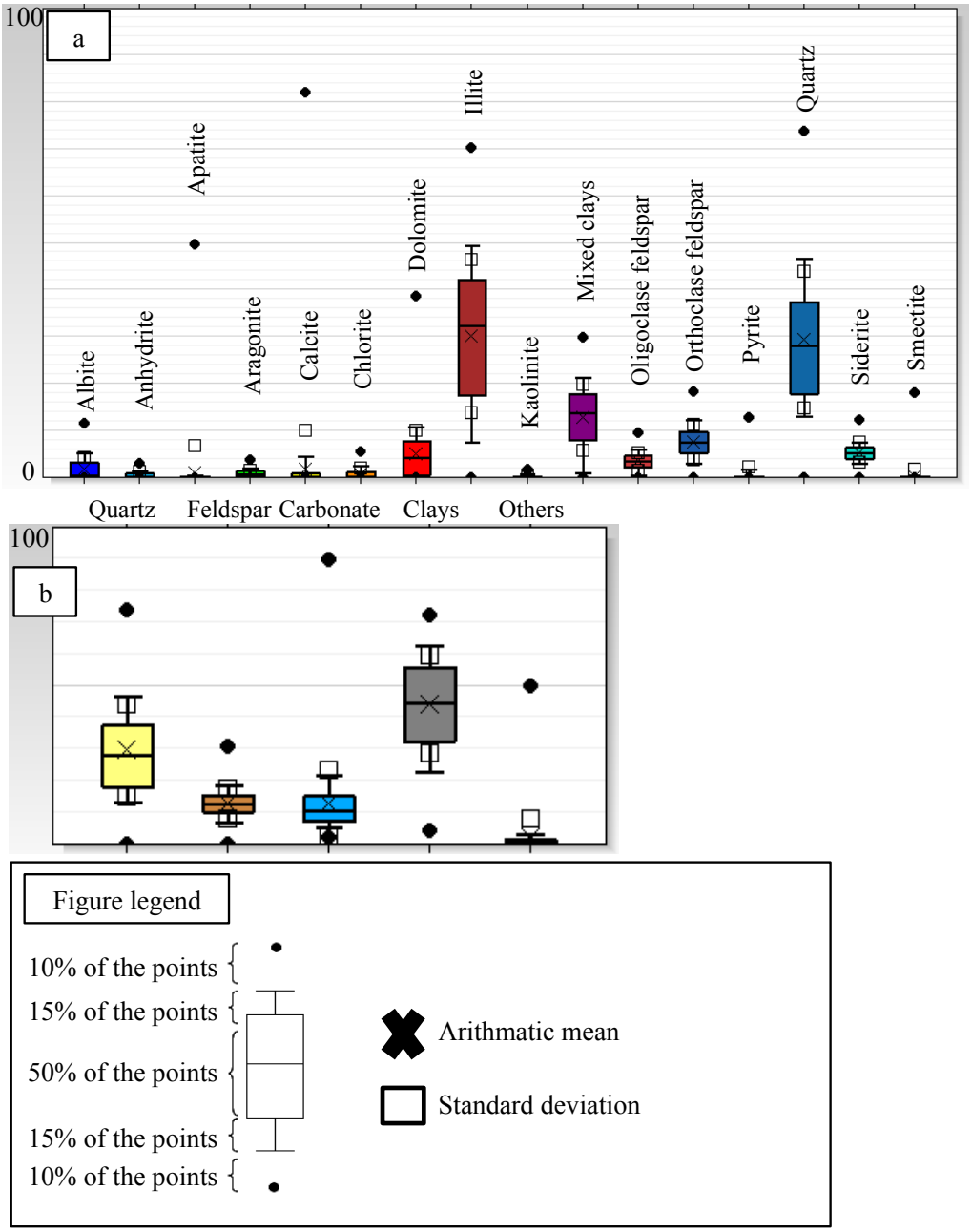

Figure 4: Box-and-whisker plots showing distributions of different minerals measured through FTIR (a). Distributions of 5 group of minerals mentioned in Table 1 (b). (c) Mineralogic variations with depth for well 1, 2, and 3. (d) Crossplot of the two dominant minerals: quartz and clays in the studied wells 1 through 6 indicate that these two parameters are inversely proportional to each other.

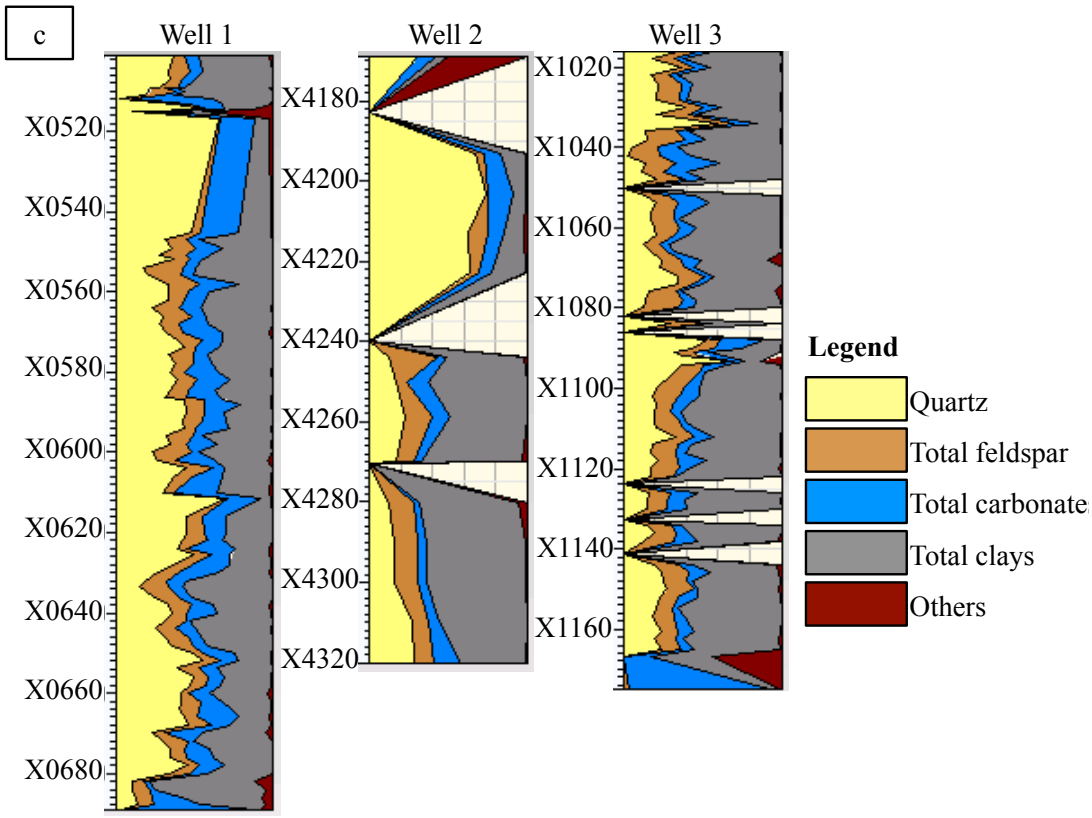
c
Well 1
Well 2
Well 3
X0520
X0540
X0560
X0580
X0600
X0620
X0640
X0660
X0680
X4180
X4200
X4220
X4240
X4260
X4280
X4300
X4320
X1020
X1040
X1060
X1080
X1100
X1120
X1140
X1160
Legend
Quartz
Total feldspar
Total carbonate
Total clays
Others

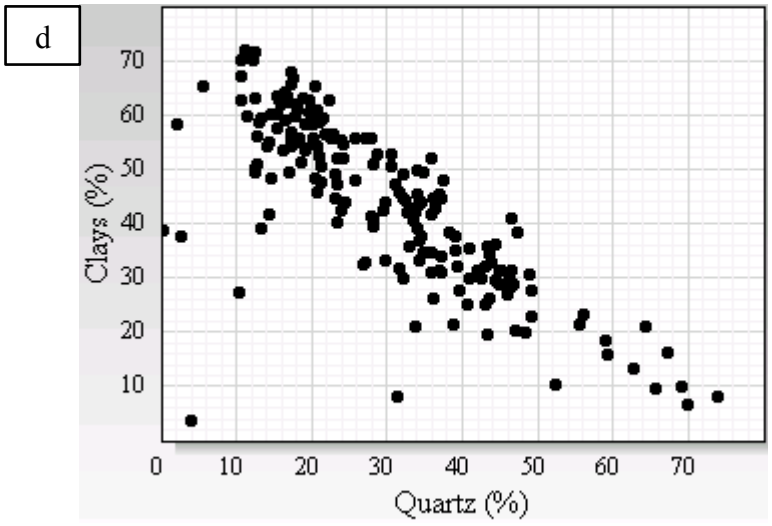
d
Clays (%)
Quartz (%)
10
20
30
40
50
60
70
0
10
20
30
40
50
60
70

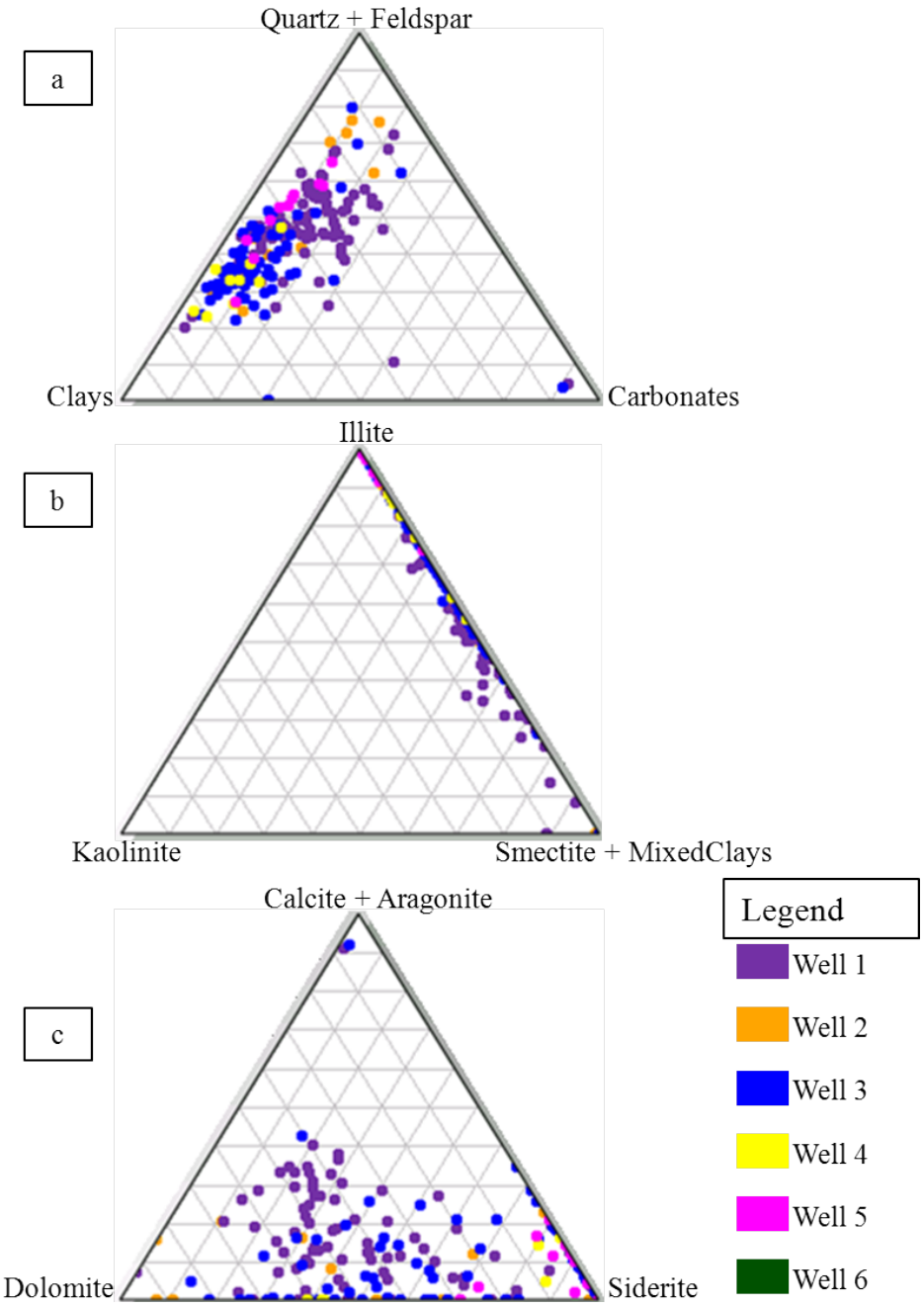

Figure 5: Ternary plots showing distributions of (a) quartz+feldpar, clays, and carbonates. Note, the Woodford is a silica-dominated system with little carbonate. Total carbonate is <20% except for few samples, (b) distributions of different clay minerals, and (c) distributions of different carbonate minerals.

Ultrasonic measurements: Acoustic velocities are measured on samples from wells 1 & 3, as core plugs required for the ultrasonic velocity measurement could be recovered from these two wells only. 84 velocity measurements are performed. The ranges and averages for V_p-fast, V_s-fast and V_s-slow are 3.7km/s to 6.35km/s and 4.79km/s, 2.35km/s to 3.91km/s and 3.01km/s, 1.3km/s to 3.76km/s and 2.48km/s respectively. Ultrasonic velocities show little pressure dependence (Figure 6). Small increase in velocity at low confining pressure (P_c) is most likely due to closures of desiccation cracks. Such characters are observed specially in samples with higher clay concentration.

Only few dynamic elastic moduli are obtained in this study as ultrasonic measurements are performed only on horizontal plug. It was not possible to obtain 3 sets of plugs (horizontal, vertical and 45°) required to measure 5 independent elastic moduli which are needed to fully define the characteristic transverse anisotropy of shales. The fine-scale heterogeneity poses a problem to acquire equivalent core plugs with different orientation and also samples are always biased toward the more competent strata.

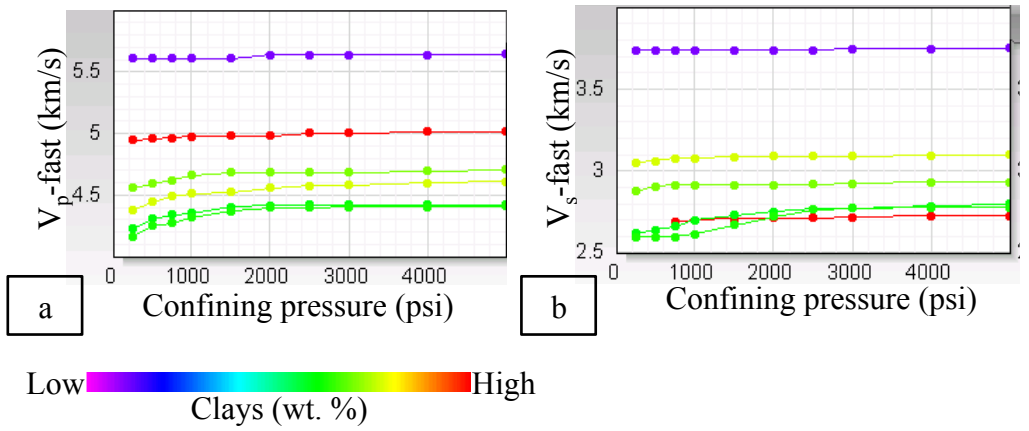

Figure 6: Ultrasonic velocities plotted as a function of confining pressure. Both compressional- and shear-wave velocities (V_p-fast and V_s-fast) exhibit weak dependence on pressure. Different colors represent samples with different clay concentrations. Note, small increase in velocities (primarily compressional) at low confining pressure for samples with higher clay concentrations.

TOC: Total organic carbon (TOC) ranges between 0 wt.% and 14 wt.%. Such concentration of TOC indicates a significant volume fraction of the rock since the density of organic matter ($1 g/cm^3$) is much lower compared to common rock forming minerals (Sondergeld et al., 2010). This implies that the petrophysical properties of organic matter significantly affect the overall rock petrophysical properties. Moreover, SEM imaging has revealed lots of pores within organic matter, which even increases the volume of organic matter for a given TOC weight percent (SEM paper).

Rock-Eval analyses: Rock Eval has been performed on 150 samples. In this experiment, organic matter is pyrolized with step increase in temperature. The amplitudes of S1, S2 and S3 peaks recorded in this experiment are representative of liquid hydrocarbons present in the rock, the amount of convertible kerogen, and the amount of inorganic carbon dioxide released, respectively. The temperature for the highest S2 peak

represents thermal maturity (T_{max}). Average T_{max} for studied wells 1 through 5 are: 467°C, 458°C, 466°C, 439°C and 441°C and equivalent R_o are: 1.25%, 0.99%, 1.23%, 0.74% and 0.78%. T_{max} is converted to equivalent vitrinite reflectance value through equation: R_o (%) = (0.0180*T_{max})-7.16 (Espitalie, 1986). For wells 1, 2 and 3, S2 peaks are either too low or forms a plateau and lack any peak (characteristics of high thermal maturity) (Figure 7) and hence, limited confidence should be given to S2 values and T_{max} derived from this S2 peak. Also quantitative use of these parameters should be limited. Measured R_o for well 1 through 6 are: 1.62%, ~1.6%, 1.67%, 0.54%, 0.54% (Comer, personal communication). Jarvie (1991) mentioned that for high maturity samples microscopic estimation of R_o is more reliable than Rock-Eval analyses. However, such measurements should be made by the same person in order to reduce human error.

Both vitrinite reflectance and average T_{max} values indicate that wells 1 through 3 and 6 are in condensate-wet gas window and wells 4 and 5 are in the oil window; however, over 300ft interval (average thickness of the Woodford Shale in the study area) thermal maturity may vary a bit. Figure 8 indicates that wells 4 and 5 have type II kerogen whereas the high maturity wells falls near the origin and shows a wide range of kerogen type; this plot represents the present day organic matter type. Jarvie et al. (2007) documented that thermal maturity as well as expulsion of hydrocarbon from rocks affect the chemical composition of kerogen and make it difficult, if not impossible, to recognize original kerogen type in highly mature samples. Since, low maturity samples are plotted as type II, starting material for the highly maturity samples are also interpreted to be type II. The facts that type II kerogen results primarily from marine source and the wells 4 and 5 are located near-shore compared to wells 1,2, 3 and 6 which are located deeper marine,

further ensure that starting organic matter in the studied wells is type II. Overall, the wells are grouped into two ranges of maturity: highly mature (wells 1, 2, 3 and 6) and low mature (wells 4 and 5). Original kerogen type has been interpreted as Type II.

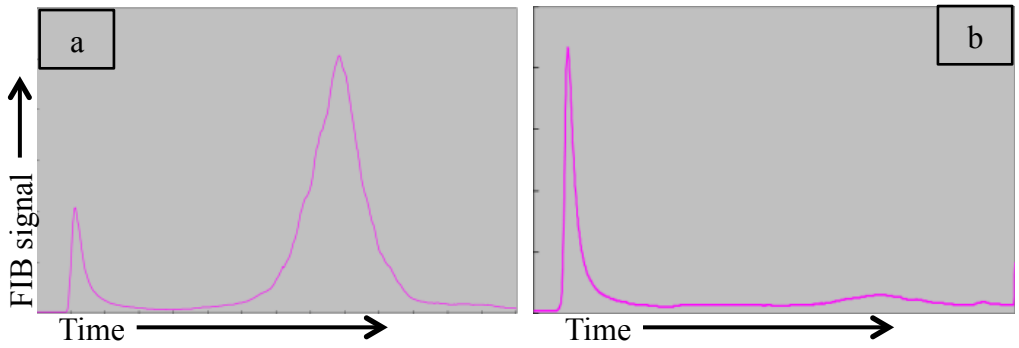

Figure 7: (a) Pyrogram of a sample from well 4, showing distinct S1 and S2 peaks respectively from left to right. (b) Pyrogram from high maturity sample in well 1. Note, the low S2 peak in figure b.

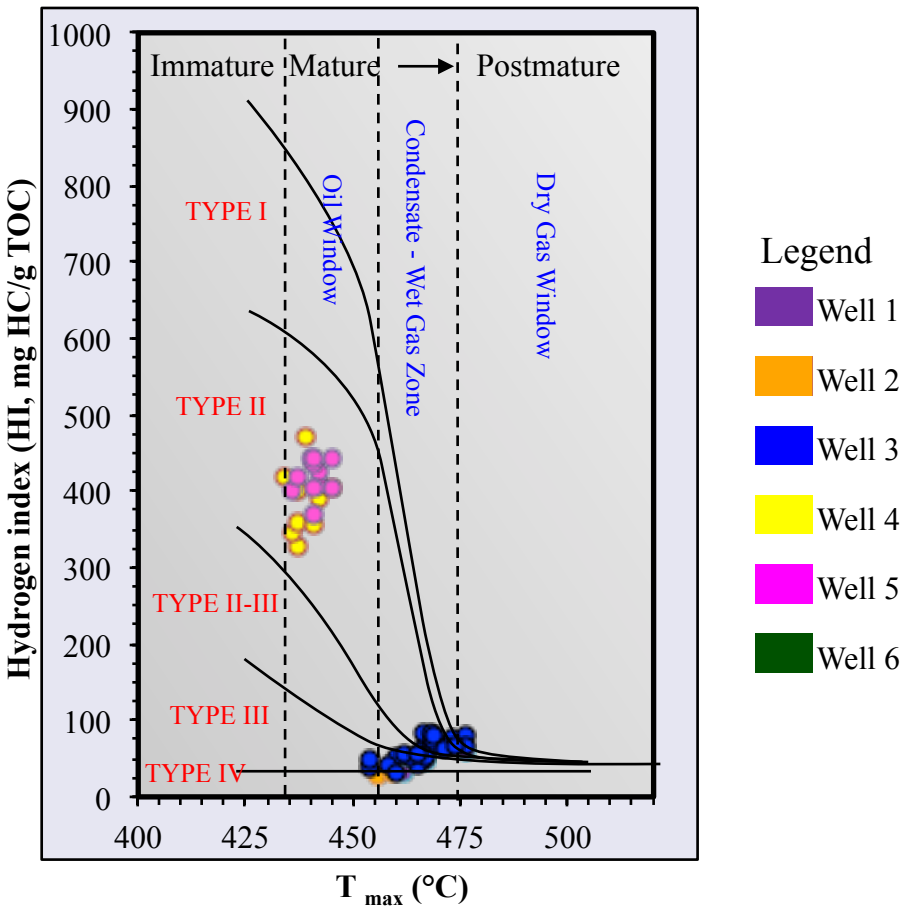

Figure 8: Crossplot of Hydrogen index (HI) and T_{max}. Wells 1 through 3 and 6 are at higher maturity level compared to wells 4 and 5. HI is calculated using the following formula: S2*100/TOC, mg HC/g TOC.

Mercury injection capillary pressure (MICP): MICP measurements show absolutely no mercury intrusion below 10,000-psi confining pressure, indicating pore throats are smaller than 0.01µm. This is equivalent to a matrix permeability of few 100's of nanodarcy. Lack of representative shale sample, appropriate for applying conformance correction (Sigal, 2009) limits the quantitative use of MICP data. This is why emphasis has been placed on analyzing the shape of the capillary pressure curve, even though Hg

injection measurement provides an estimate of the connected pore space. Different shape of the capillary pressure curve represents different pore throat distributions, different pore throat diameters etc. and have been used for rock typing.

Discussions

We will focus our discussion to distinguish critical petrophysical properties and their effect on two critical components of the unconventional resource-shales: (i) storage capacity, and (ii) deliverability. Like any other petroleum system porosity (Φ_{He}) is directly related with storage capacity. On the other hand, hydrocarbon is generated from organic matter within the self-sustained resource-shale petroleum system. Hence, concentration of organic matter (TOC) directly affects potential volume of hydrocarbon present within the system. However, there is no tool to directly measure either porosity in shale or TOC in field-scale and it is impossible to collect core or laboratory data from each well. Here we evaluate any correlation between these two properties and other petrophysical properties such that closely associated parameters can be used to indirectly estimate porosity and TOC.

Crossplot of TOC and Φ_{He} shows porosity increases with TOC (Figure 9). Correlation between TOC and porosity improves when wells with similar thermal maturities are considered. Overall, samples with lower thermal maturity (wells within oil window) contain lower Φ_{He} compared to samples with higher thermal maturity (wet gas–condensate window) as more pore spaces are created within organic matter as more and more hydrocarbon is expelled out with increasing thermal maturity. Good correlation between TOC and porosity is supported by the fact that organic pores are the dominant

pore types in this resource shale, as observed through SEM imaging (SEM paper). Previous authors (Curtis et al., 2011; Loucks et al., 2009; Passey et al., 2010) have observed organic pores as the most dominant pore types in other resource shales as well. Although overall porosity increases with thermal maturity SEM imaging has revealed a more complex nature of this porosity development. Mechanism behind the formation of such organic pores is discussed later.

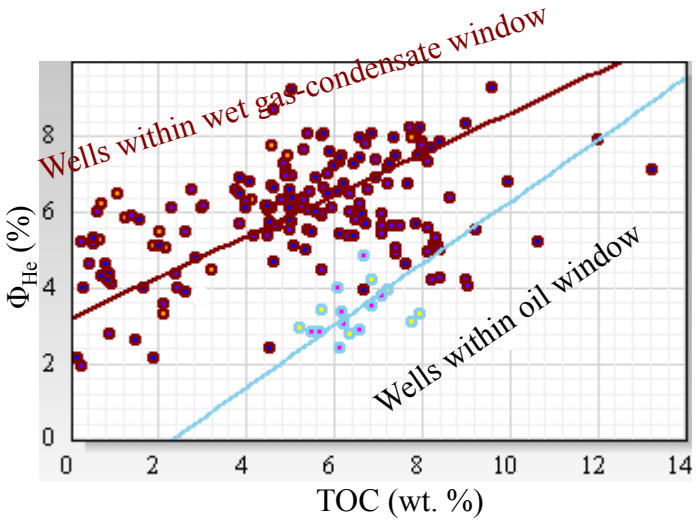

Figure 9: Crossplot of core porosity (Φ_{He}) and TOC indicates good correlation between these two parameters. Red circles represent data from high thermal maturity wells (wells 1, 2, 3, and 6). Cyan points are from low thermal maturity wells (wells 4 and 5). Equations for the red and cyan regression lines, fitted to red and cyan points are: Φ_{He} = 0.54 * TOC + 3.22; Φ_{He} = 0.83* TOC - 1.98.

Crossplots of porosity and mineralogical composition reveal complex relation between porosity and the two dominate minerals: quartz and total clays. Crossplot of Φ_{He} and clays indicates overall increasing Φ_{He} with increasing clay concentration (Figure 10). Similar correlation has been observed in the Barnett Shale (Kale, 2009) and 13 Finger (Raina, 2010). A closer look to the crossplot of porosity and clay indicates two clusters of rocks: (i) rocks with clays<42%, where porosity increases with increasing clay concentration, and (ii) clay concentration>42%, where porosity decreases with increasing clay concentration. The first group of rocks is also characterized by overall high quartz concentration compared to the second group. Crossplot of porosity and quartz (Figure 11) apparently does not indicate any correlation. Correlation between porosity and quartz improves when data is broken into two clusters: (i) rocks with quartz<40% where porosity increases with quartz, and (ii) rocks with quartz>40% where porosity decreases with increasing quartz. Overall, the first group of rocks contains high clay percentages indicating that most of the samples from this group also belong to cluster 1 on the porosity-clay crossplot.

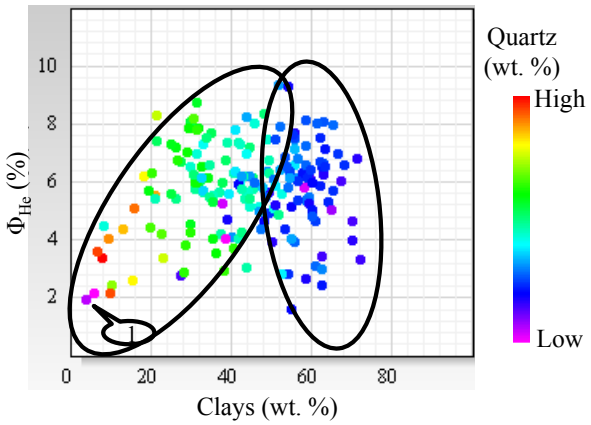

Figure 10: Crossplot of core porosity (Φ_{He}) and total clays. Data is colored with quartz content (wt. %). Data bounded by two ellipses indicate two clusters of rocks. The cluster with higher clay concentration is characterized by low quartz concentration and the other cluster with lower clay concentration is characterized by higher quartz concentration. Points marked by "1" indicates carbonate-rich samples, characterized by both low clays and low quartz concentrations.

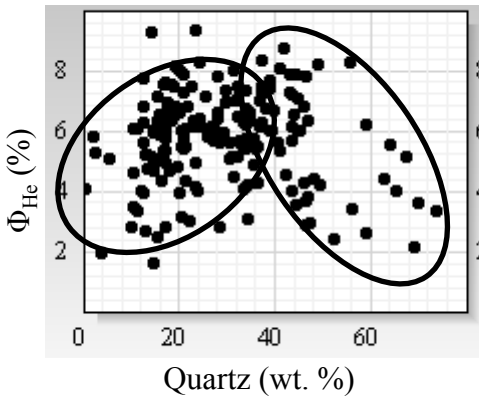

Figure 11: Crossplot of core porosity (Φ_{He}) and quartz. Crossplot exhibits two clusters of rocks as indicated by two ellipses. Φ_{He} increases with increasing quartz for quartz<40% and decreases with increasing quartz for quartz>40%.

As sated before, TOC directly affects the presence of hydrocarbon within the self-sustained resource-shales. TOC is also correlated with porosity that increases with increasing porosity (Figure 9). In general TOC increases with increasing clay content as observed by previous authors (Kale, 2009; Raina, 2010) in other resource shales. Crossplot of TOC and clays (Figure 12a) however reveals more subtle correlation between TOC and clay content for the studied shale. The crossplot indicates three clusters of rocks with unique correlations between these two parameters: (i) Rocks with low clay concentration (0%<clays<24%), is characterized by low TOC. TOC does not show any correlation with clays for this group of rocks. (ii) Rocks with intermediate clay concentration (8%<clays<48%), where TOC increases with increasing clay content. (iii) Clay rich rocks (clays>44%); this group of rocks has a wide range of TOC (0%-14%). However, TOC does not show much dependence on clay content. Crossplots of TOC and quartz shows apparently poor correlation between these parameters; correlation improves when the data is broken into three clusters (Figure 12b): (i) rocks with quartz<25%, where TOC shows loosely increasing trend with increasing quartz content. This group of rocks is also characterized by high clay content and hence, belongs to the group iii on the TOC-clay crossplot. (ii) For rocks with 24%<quartz<58%, TOC shows good dependence on quartz concentration and increases with increasing quartz concentration. This group of rocks is also characterized by intermediate clay content and hence, belongs to the group ii on the TOC-clay crossplot. (iii) Rocks with high quartz content (quartz>58%), TOC decreases with increasing quartz concentration. Overall TOC is low in this group of rocks. This group of rocks is representative of the characteristic cherty facies of the

Woodford Shale (chapter 4 of this dissertation, Hoeve et al., 2011). This group of rocks contains low clay and belongs to group ‘i' on TOC-clay crossplot.

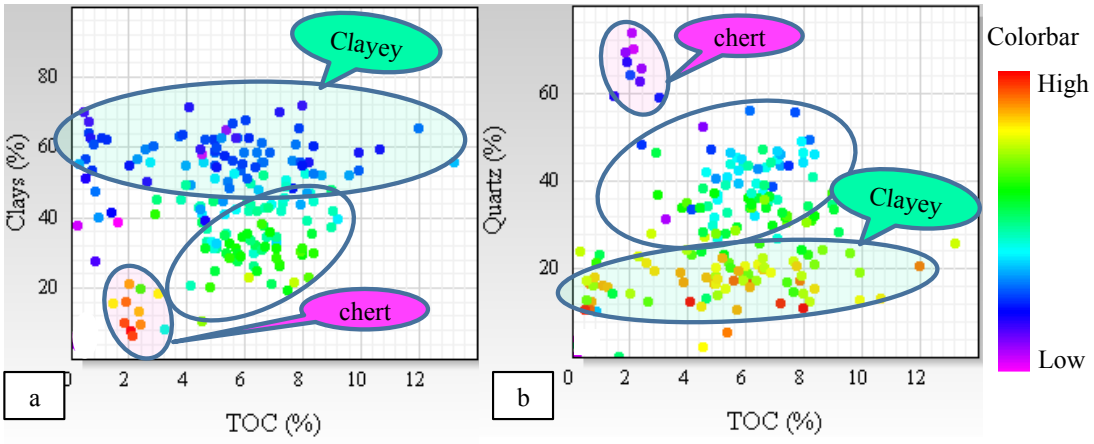

Figure 12: Crossplot of TOC and (a) clays, (b) quartz. Data is colored with quartz and clay content in figure a, and b respectively. Crossplots indicate more than one cluster of data as bounded by the ellipses.

TOC does not have any correlation with total carbonate, which is obvious, as the geologic history indicates silica-shelled organisms dominated the Woodford Sea (chapter 4 of this dissertation; Lambert, 1993; Sullivan, 2006). These silica-shelled organisms along with marine algae (Tasmenities for example) are the source of TOC in the Woodford Shale. Carbonate shelled organisms had limited existence in the study area (Comer, 2008; chapter 4 of this dissertation; Sullivan, 2006). Primary source of carbonate was detrital (Comer, 2008) along with some diagenetic dolomite, and aragonite which formed as bi-product of bacterial activities in the upper few centimeter of sediment column (chapter 4 of this dissertation).

Geologic history of the study area indicates two sources of silica: biogenic and detrital (chapter 4 of this dissertation, Cladwell, 2011). For the group of rocks with intermediate clay and quartz content (8%<clays<48% and 24%<quartz<58%), increasing trends of TOC with increasing quartz content indicate biogenic silica dominates in this group of rocks. As increasing quartz content also increases the brittleness of the rocks (Sondergeld et al., 2010); this group of rocks is also characterized by increasing brittleness with increasing potential for the presence of hydrocarbon. Such brittle nature of this rocks makes it easier to initiate hydraulic fracturing in this rocks and thus improves the hydrocarbon deliverability of this rocks.

Deliverability of the resource shale is largely controlled by the success of hydraulic fracturing which is primarily governed by the mechanical properties of shales. Dynamic elastic moduli calculated from acoustic velocities provide an indirect estimate of mechanical properties. In this study, ultrasonic velocities are measured on horizontal core plugs collected from two wells (well 1 and 3).

Crossplots of ultrasonic velocities, elastic moduli with other petrophysical indicate that both porosity and TOC varies inversely with both Vp and Vs, Young's modulus (E) is inversely proportional with TOC for E<60 GPa and TOC>4% (Figure 13).

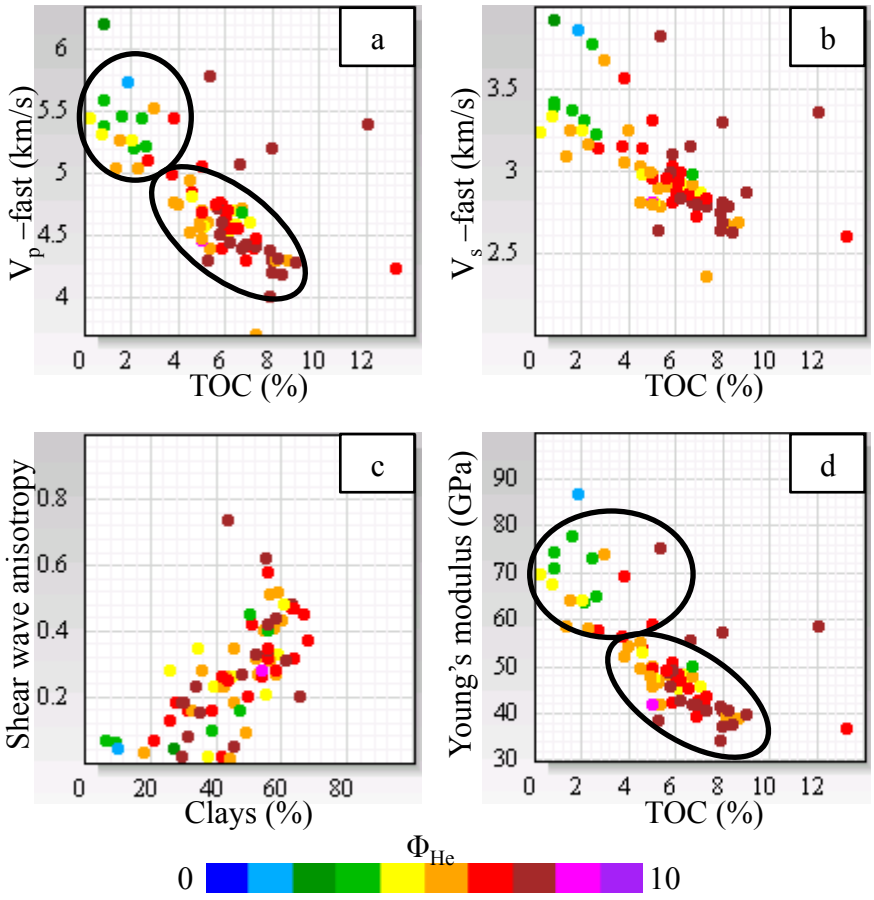

Figure 13: Crossplots of V_p-fast and V_s-fast with TOC, shear wave anisotropy and clay, and Young's modulus and TOC. Black circles indicate possible different rock types holding unique correlation between different petrophysical parameters. Data are colored with Φ_{He}, as shown on the color bar.

Combination of Young's modulus and Poisson's ratio is often used to define brittleness of rocks such that rocks with high Young's modulus and low Poisson's ratio are brittle, and hence, are easily fraccable compared to rocks with low Young's modulus and high Poisson's ratio and considered as ductile (Rickman et al., 2008). For the Woodford Shale, Poisson's ratio varies between 0.05 and 0.16, V_p-fast/V_s-fast ranges

between 1.4 and 1.65 while Young's modulus varies between 36 GPa and 80 GPa. Due to such narrow range of both Poisson's ratio and V_p/V_s the brittleness of the Woodford Shale is dictated by the Young's modulus.

Detailed core description of well 3 reveals that only layer bound natural fractures are present in two intervals where some siliceous laminae/cherty layers are present with alternate mudstone (Figure 14). Although it was not possible to collect plugs and ultrasonic measurements from the thin brittle layers, mineralogy data confirms high quartz content of those siliceous layers.

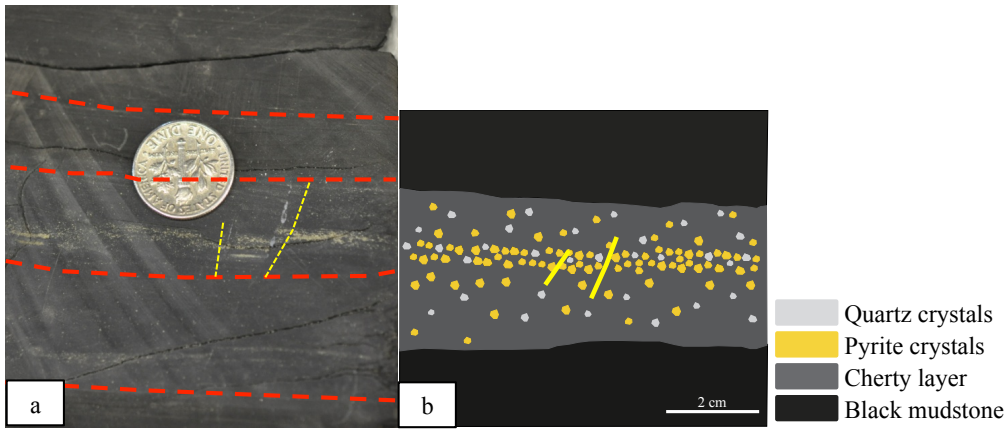

Figure 14: (a) Core sample from well 3 showing small-scale faulting bounded within the brittle layer. Red dashed lines indicate the boundaries between more brittle (central interval), less brittle and ultimately to the black mudstone, yellow lines indicate vertical fractures bounded within the brittle layer. Dime is kept for scale. (b) Schematic representation of picture a.

Mechanism for organic-pore development

SEM imaging analysis helped us to make visual inspection of organic pores and investigate the presence of any other pore types. SEM imaging of samples with thermal

maturity varying from oil window (R_o 0.7%) to post-mature wet gas condensate window (Ro 1.72%) allowed us to visually inspect the distribution of pores with increasing thermal maturity. Figure 15, Figure 16a and Figure 16b shows examples of organic pores at different thermal maturities indicating very little porosity in sample with low thermal maturity (Figure 15a, Figure 16a) and lots of organic pores in sample with high thermal maturity (Figure 15b, Figure 16b). This matches with the laboratory data, which also indicates overall increase in porosity with increasing thermal maturity (Figure 9). However, SEM images of some samples with low thermal maturity (R_o 0.7%) reveal lots of pores (Figure 16c, d) indicating complex mechanism behind the formation of such pores.

Detail analyses through SEM imaging indicate that although more organic pores are developed with increasing thermal maturity; such increase in porosity is not a simple function of thermal maturity. A possible mechanism for the formation of organic pores is discussed as follows. Jarvie (1991) documented three forms of organic carbon such as: (i) extractable organic carbon (EOM), (ii) convertible carbon, and (iii) residual carbon. We propose that distributions of these different forms of carbon within the starting organic matter actually control the amount of organic pore formation through following mechanism. With increasing thermal maturity hydrocarbon is generated from EOM while some convertible carbon gets converted to EOM and fill up the void space created by the expulsion of hydrocarbon (Figure 17). This process continues until the convertible organic carbon concentration drops so much that it cannot fill up all the void spaces created by the expulsion of hydrocarbon from EOM; organic pores are developed at this stage. Zargari et al. (2011) noticed softening of organic matter at the initial stage of

thermal maturity and progressive drop in elastic modulus and hardening of organic matter leading to increase in elastic modulus with progressive increase in thermal maturity at later stage of thermal maturity.

The above mechanism also explains that organic pores will generate at much earlier stage with small quantity of convertible organic carbon compared to organic matter with higher proportion of extractible organic carbon. Figure 17b shows distributions of different forms of organic carbon in different kerogen type.

Detailed core description reveals that porous organic matters with larger pores at low thermal maturity occur in samples from the cherty mudstone facies. Geologic history indicates that deposition of such facies were associated with high energy flow; hence, different types of organic matter representing a mixture of both in-situ as well as transported organic matter are expected within this lithofacies. This also implies differential distribution of different forms of organic carbon and hence, heterogeneous distribution of pores within this lithofacies.

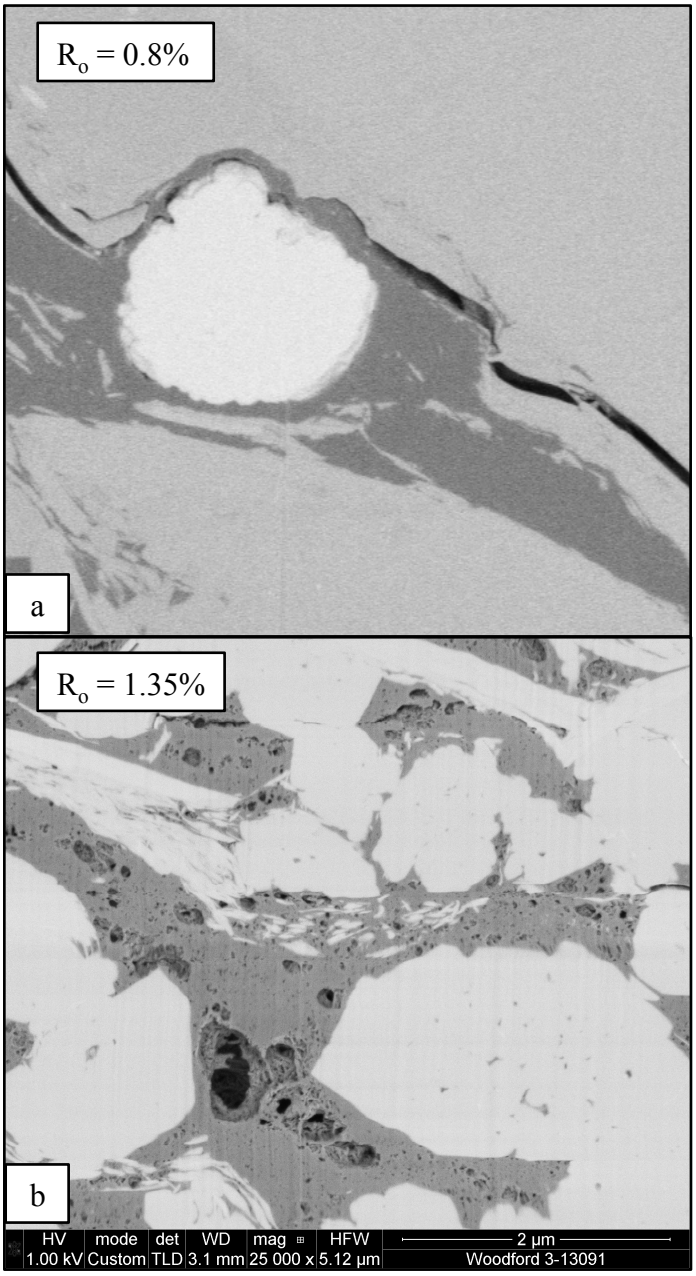

Figure 15: Backscatter electron images of focused ion beam milled samples. Grey areas are indicating organic matter; dark areas within the organic matter indicate organic pores. (a) No organic pore in sample with estimated R_o = 0.8%. (b) Lots of organic pores can be observed in sample with estimated R_o = 1.35%.

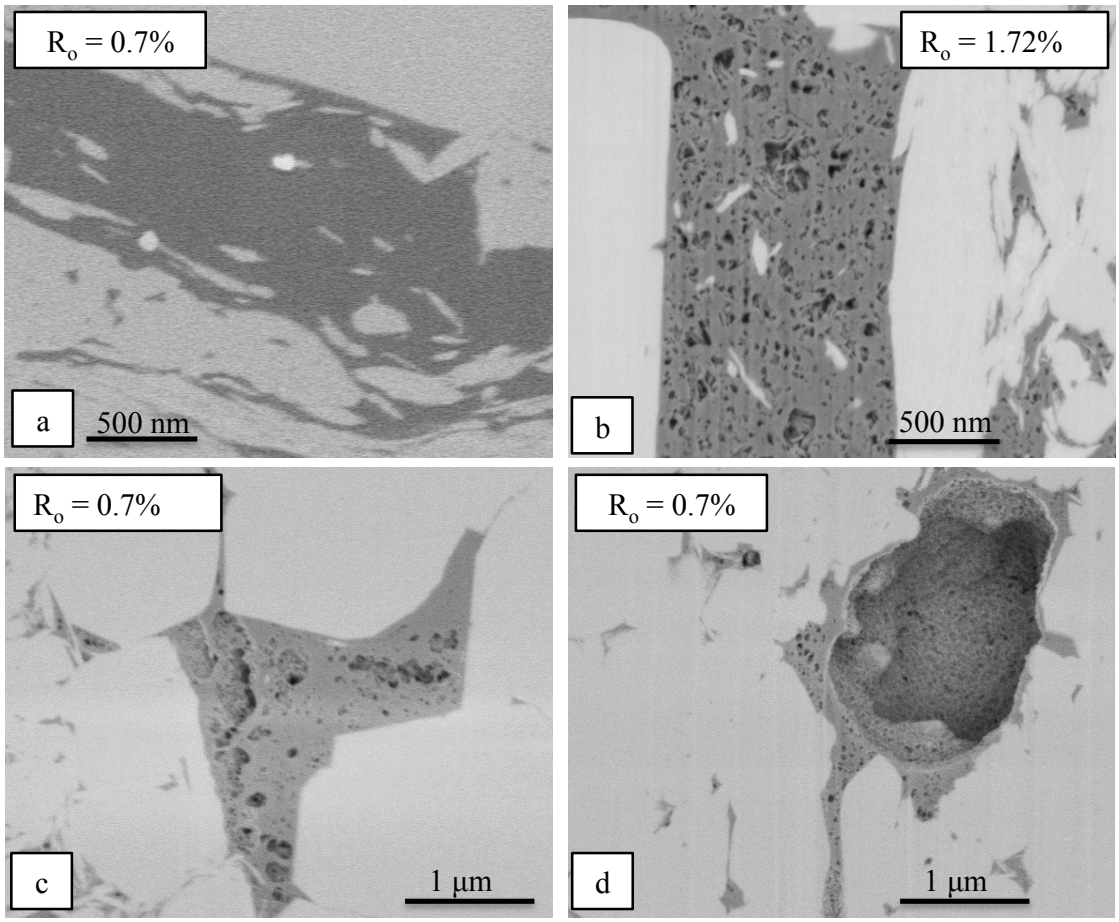

Figure 16: Backscatter electron images of samples showing distribution of organic pores at different thermal maturity. Grey areas are indicating organic matter, dark areas within the organic matter indicate organic pores. (a) and (b) Samples with R_o =2.72% and 0.8% showing a range of pore sizes within the same piece of sample. (c) and (d) Backscatter electron image of a sample with thermal maturity in the oil window (R_o =0.7%) showing lots of pores. Figure d shows large micrometer-size pore present at low thermal maturity (R_o = 0.7%).

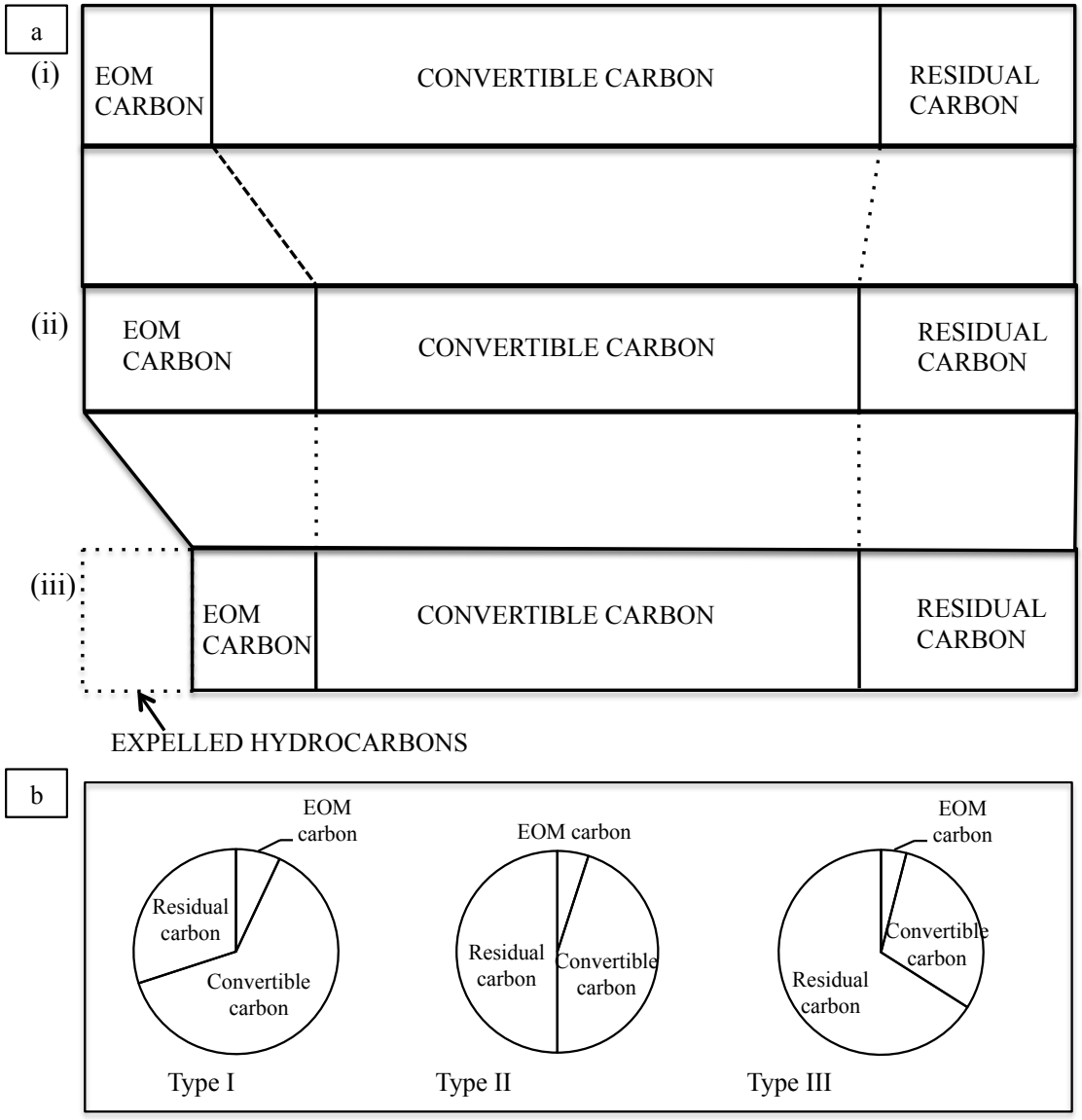

Figure 17: (a) Effect of thermal maturation on a given volume of organic carbon: (i) with increasing thermal maturity, the initial EOM and convertible carbon amounts are changed as a result of generation, (ii) EOM carbon increases at the expense of the convertible carbon, (c) with expulsion, the original TOC value is decreased by the amount of carbon contained in the expelled EOM carbon fraction. The residual carbon increases slightly with maturation. (b) Typical distributions of different forms of carbon in different kerogen types. Modified from Jarvie, 1991.

Heterogeneity of the starting organic material also causes heterogeneous distribution of porosity within equivalent samples collected from same depth. Backscatter electron image from well 1 emphasizes different amount of pores within the same piece of organic matter (Figure 18). While the heterogeneity in organic matter may result from different types of organic matter present in the host rock, heterogeneity can also be observed in different body parts of multicellular organisms. Totten (2011) has imaged different types of organic material forming the outer rim of a spore compared to the material inside it.

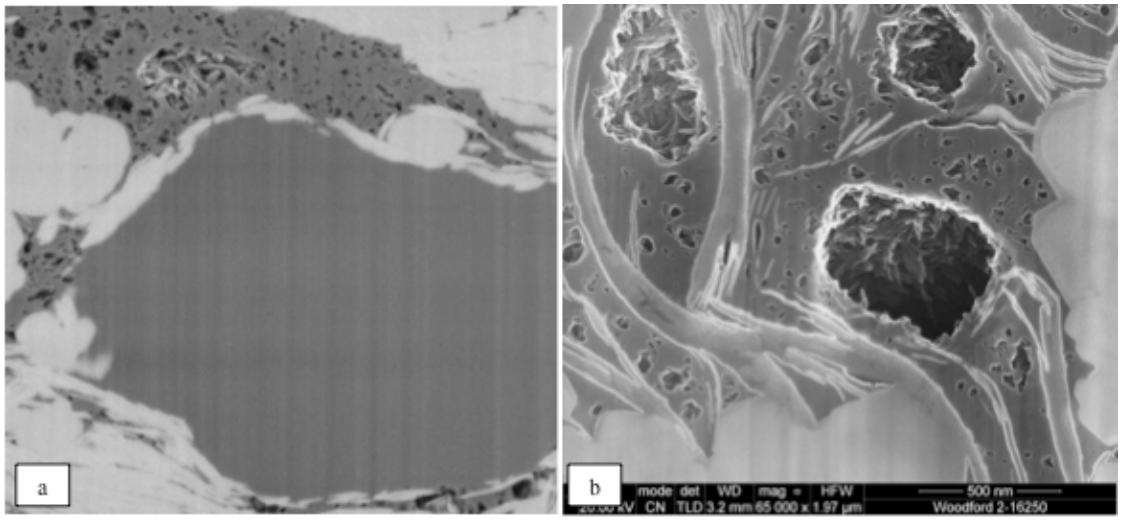

Figure 18: Back-scattered images of samples from studied wells with T_{max} = 443°C and 549°C, respectively in figure a, and b. Note organic matter (dark grey) with lots of pores (black) and without any pore space in the same sample, displayed in figure a. Figure b shows heterogeneous distribution of pore spaces within the same piece of organic matter. Horizontal axis is same for both the images.

Mercury injection capillary pressure (MICP)

Complex nature of the resource-shales limits the quantitative use of the capillary pressure data. However, different shapes of the capillary pressure curves indicate different types of rocks. Four groups of rocks have been identified based on the different shapes of the capillary pressure curves. Typical characteristics of these curves are described below (Figure 19):

Type 'A': Incremental Hg intrusion plot increases monotonously and does not reach plateau even at 60,000-psi pressure (Figure 19a). This indicates that the largest pore throats are either smaller than 3 nm diameter or pores were initially larger than 3 nm and got compressed in response to increasing confining pressure during the experiment.

Type 'B': In this type incremental Hg intrusion plot reaches a plateau (Figure 19b) indicating that largest pore volume in this rock-type is larger than 3 nm. This also implies that this rock type have the highest permeability. This rock type is also associated with highest range of Φ_{He}. Φ_{He}. = 9.3% for the example shown in Figure 19b.

Type 'C': Incremental Hg intrusion has similar shape as type 'A' (Figure 19a, c). However, they show false intrusion, which can be confirmed from the cumulative Hg intrusion curve (figure on right of Figure 19c). The saturating and desaturation cumulative intrusion curves almost follow each other without much separation between them (lack of hysteresis). Lack of hysteresis between saturating and de-saturating curves indicates false intrusion. Significant hysteresis hysteresis is observed in cumulative Hg intrusion curve type 'A'. This rock type also shows very little Hg intrusion (<0.0005 ml/g of sample); such small volume also indicates that Hg did not actually intrude the sample and the Hg-intrusion is not real.

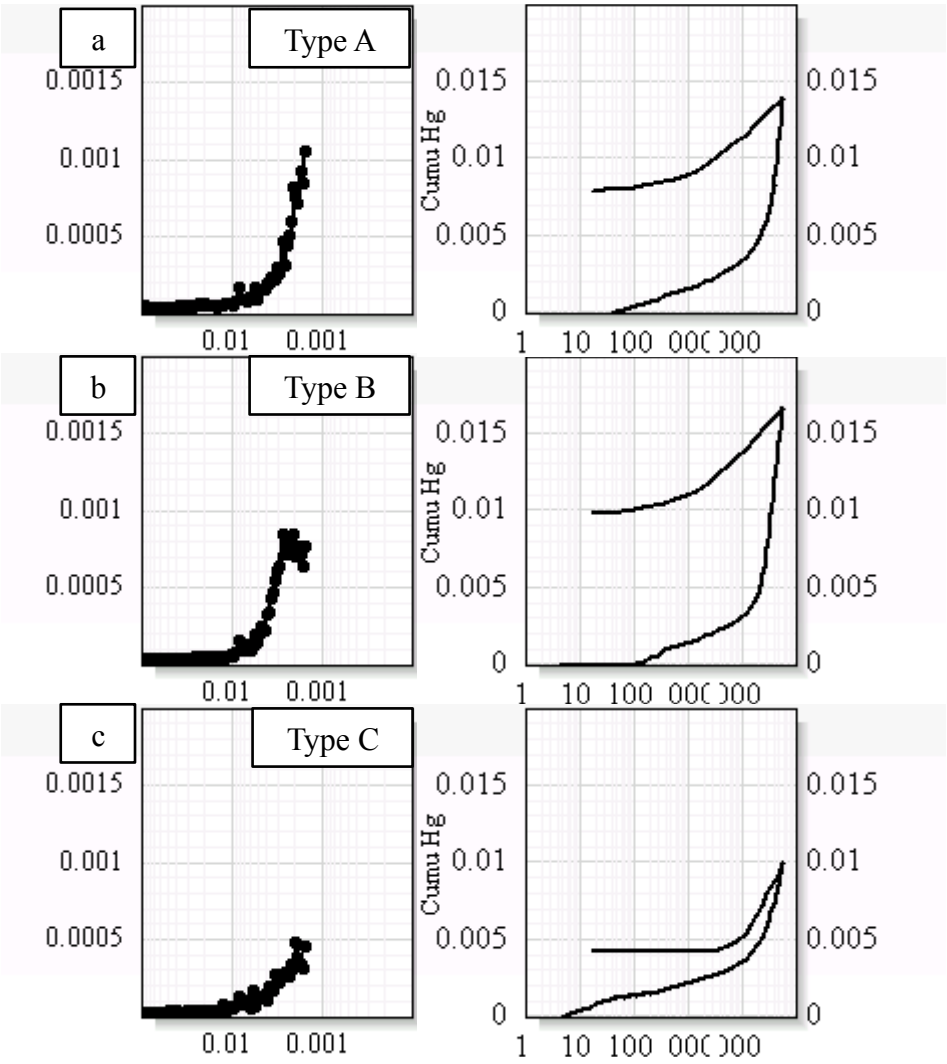

Figure 19: Examples of MICP curve type A through C in figures 'a' through 'c' respectively.

Type 'A', 'B' and 'C' have also been observed in the Barnett Shale from the Fort Worth Basin (Kale et al., 2010b). For all the samples, it has been observed that intruded Hg volume is smaller compared to volume of Φ_{He}. This implies that either pores are not connected (mercury can intrude only into the connected pore spaces) or pore throats are smaller than 3 nm.

Petro typing

It is obvious from the previous discussion that there are at least two clusters of rocks possibly indicating different petro-types. Petrotypes are defined as units of rocks possessing unique sets of petrophysical properties and were deposited under similar conditions and experienced similar diagenetic processes (Gunter et al., 1997). Previous authors (Amaefule et al., 1993; Gunter et al., 1997; Pittman, 1992; and Rushing et al., 2008) have documented quantitative methods to identify petro-types in conventional reservoirs. However, standard petro-typing workflows are inapplicable for the unconventional Woodford Shale system. Two major issues which makes the conventional petro-typing principles unusable for the self-sustained resource-shale petroleum systems are: (1) large dependence on the dynamic range of porosity and permeability commonly observed in conventional reservoirs and narrow range of porosity and permeability value of the resource shales, and (2) no evaluation of the mechanical properties of rocks which play important role for hydrocarbon production from resource shales. We have used clustering analyses of principal petrophysical properties to quantitatively recognize different petro-types within the Woodford Shale in the Study area. Kale (2009) applied a similar clustering analysis technique to identify different petro-types within the Barnett Shale.

Petrophysical analysis discussed in the previous sections show that only few petrophysical parameters show significant dynamic range to be useful for identifying different group of rocks, such as: Φ_{He}, TOC, quartz, illite, smectite-mixed clays, total clays (Figure 4a, b). Mineralogy data from wells 1 through 6, located in different part of the basin, show that illite is the most dominant clay mineral and hence, total clay instead

of illite have been used for clustering analyses. Previous studies (Kale, 2009; Raina, 2010; Sondhi, 2011) on other resource-shales also indicate that wide range of porosity, total organic carbon content, and mineralogy are useful in defining different rock types within the resource-shales.

Clustering analysis of different parameters using Gaussian K-means classification method (Bardley and Mangasarian, 2000) ultimately helped us to quantitatively define these rock types. The Gaussian K-means classification method analyzes "N" data points located in "I" dimensional space and then classifies them into "K" clusters, so that the variance between any two members from two different groups are more than the variance between any two members of the same group (N, I and K are any integers). Three groups of rocks (K=3) have been identified through this technique and using four petrophysical parameters (I=4): Φ_{He}, TOC, quartz, and clays.

Ultrasonic velocities as well as dynamic elastic moduli also indicate different clusters as shown in Figure 13. However, ultrasonic data could not be included into the clustering analyses as only few ultrasonic measurements could be performed and also sampling of core plugs required for these measurements are biased towards more competent rocks.

Table 3 summarizes petrophysical properties of different petro-types identified through clustering analysis. Figure 20 shows petrophysical characteristics of different petro types identified through clustering analysis. Petro type 3 shows intermediate clay (20%<clay<53%) and quartz content (26%<quartz<55%) with high porosity and high TOC values (average TOC 7.5%). In this petrotype TOC increases proportionally with quartz (Figure 20d), which enhances the brittleness of the host rock. Such petrophysical

properties indicate that this petro-type forms good reservoir rock. Petro-type 2 has a wider range of porosity (2.4%-9%) and TOC (0%-13%). However, this petro-type is characterized by high clay concentration (>42%; 90% confidence interval) (Figure 20c). Measured petrophysical properties indicate that Petro-type 1 is characterized by both low porosity and TOC values. The organic matter in this petro-type contains large micrometer size pores identified through SEM imaging. The low porosity values are due to overall low TOC content of this facies. High quartz content (Figure 20a) of this litho-type makes it the most brittle petro-type.

Petro-type	**TOC (%)**		**Φ_{He} (%)**		**Quartz (%)**		**Clays (%)**	
	Range	**Average**	**Range**	**Average**	**Range**	**Average**	**Range**	**Average**
1	**1-4**	**2.5**	**2-5.5**	**3.9**	**59-73**	**66.5**	**7-20**	**13**
2	**0-13**	**6.5**	**2.4-9**	**6.0**	**13-56**	**37**	**27-71**	**55**
3	**3-12**	**7.5**	**4-9**	**6.5**	**26-55**	**40.5**	**20-53**	**36**

Table 3: Petrophysical properties of different petrotypes.

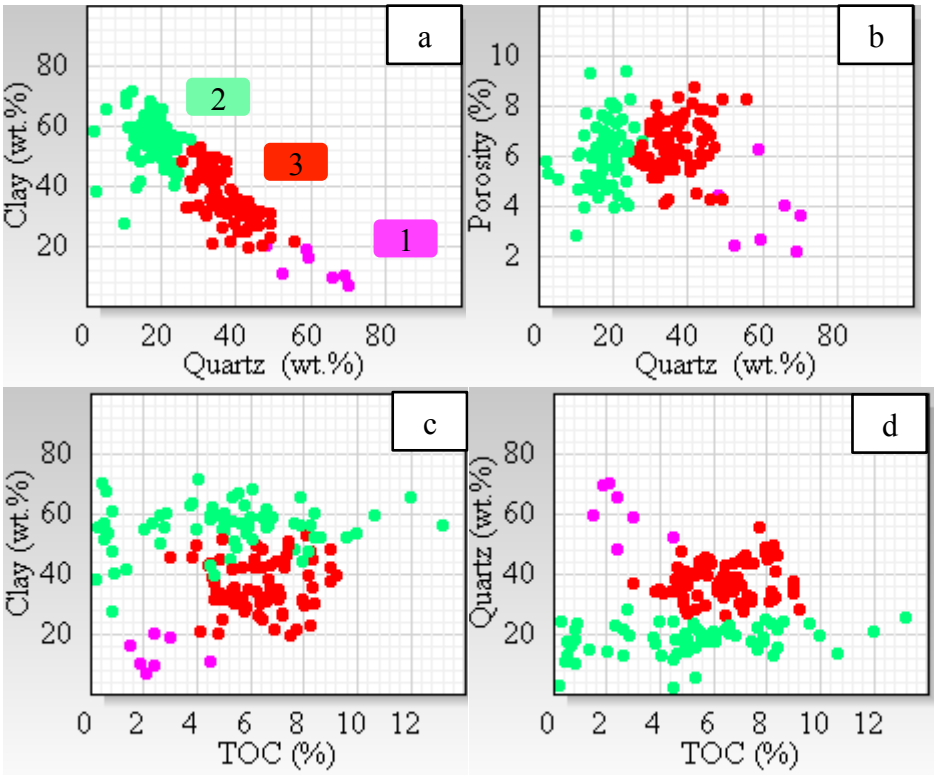

Figure 20: Crossplots of porosity, TOC, quartz and clays showing 3 petro-types identified through clustering analyses. Petro-type 1 through 3 are colored with pink, green and red as marked on figure 'a'. Figure 'a' indicates that each petro-type is characterized by unique range of clay and quartz concentrations.

Reservoir qualities indicated by petrophysical properties also correspond to the production data. For example, well 3 is reported as dry well, which contains the highest thickness of the clay rich petro-type 2 and the thicknesses of different petro-types within the Woodford interval in this well are as follows: 4%, 78% and 18% respectively for petrotype 1 through 3. On the other hand the well 1 is a hydrocarbon producing and is characterized by the highest thickness of petro-type 3. Thicknesses of different

petrotypes within the Woodford interval in this well are as follows: 18%, 16% and 66% respectively for petrotype 1 through 3.

Good correlations between these different groups of rocks with the geologic history indicate that these rock types are indeed indicating different petrotypes that are important for reservoir evaluation purposes. For example, petro-type 1 represents the cherty mudstone lithofacies, characterized by high quartz content and low TOC while petro-type 2 and 3 represent the black mudstone facies. Visual inspections of sub-surface cores reveal that the cherty mudstone facies are typically centimeter thick; this thin nature of this lithofacies makes it difficult to measure petrophysical properties of this litho-type even at the laboratory-scale. Integration of geologic analyses will help in this regard as it provides systematic approach to understand the presence of different litho-types.

Although petrophysically petro-type 3 is the best reservoir followed by petro-type 2, TOC-rich intervals from either petro-type are characterized by low Young's modulus, high Poisson's ratio as well as high V_p-V_s ratio and hence, are ductile in nature (Figure 21). Such ductile nature of the hydrocarbon/TOC enriched intervals demand intervening brittle intervals in order to initiate hydraulic fracturing and produce hydrocarbon from the otherwise impermeable resource-shales. Hence, vertical juxtaposition of petro-types with contrasting mechanical properties (brittle versus ductile) will improve reservoir quality of the resource shales. Among the studied wells, the best producing well 2 is characterized by most wide distributions of petrophysical parameters indicating presence of different petro-types in the stratigraphic column. On the other hand, despite of good reservoir storage capacity (good amount of TOC and Φ_{He},) well 3 is a dry well. Lack of contrasting petro-types in the vertical section and high clay content limited the hydraulic fracturing in

this well. This is an ideal example of a well with good storage capacity and zero hydrocarbon production due to inability to initiate hydraulic fracturing. Petro-typing is not performed on well 6 (located in between well 2 and 3) due to limited sample availability.

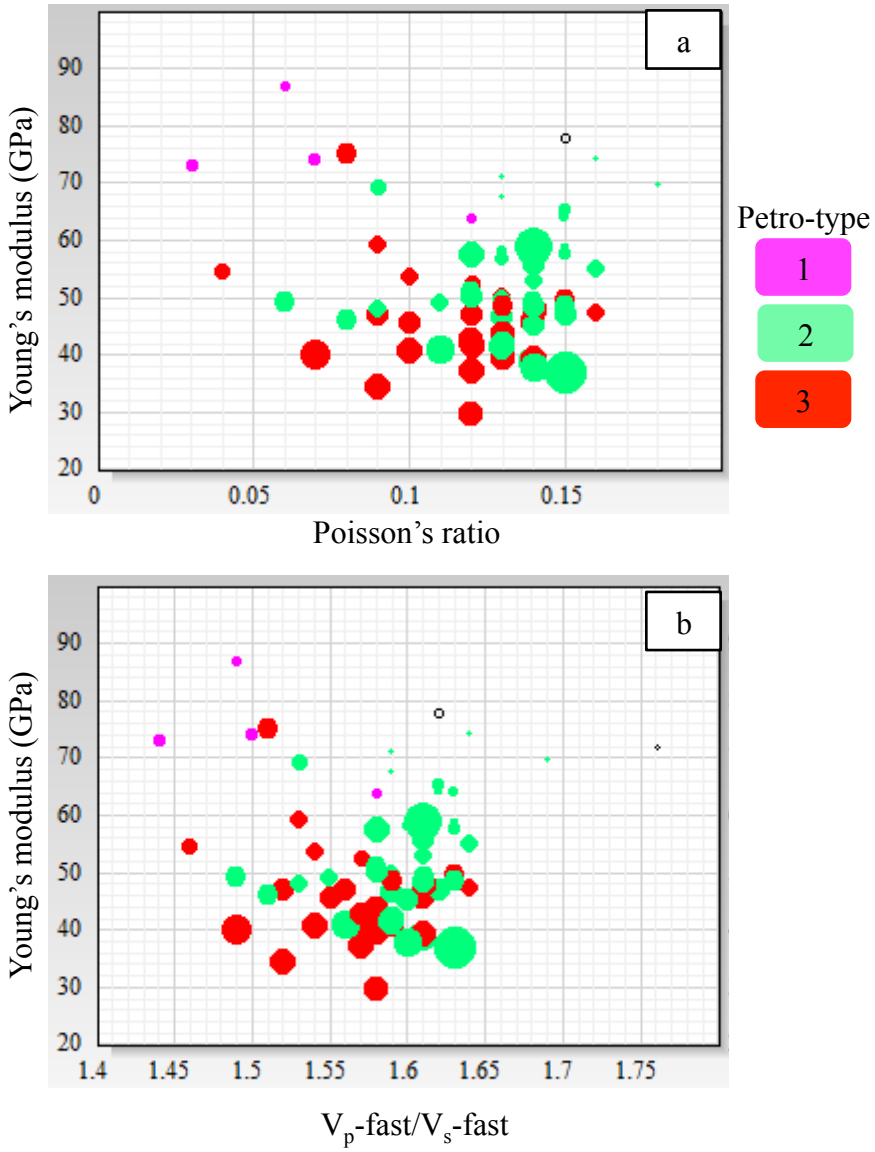

Figure 21: Crossplots of (a) Young's modulus versus Poisson's ratio (v), (b) Young's modulus versus ratio of V_p-fast/V_s-fast. Point size depicts TOC content.

Calibration of petro-types with MICP data

MICP characteristics of each petro-type are summarized in Table 4 indicating that petro-type 1 is represented by MICP type C, petro-type 2 is represented by MICP type A

while petro-type 3 contains almost equal quantity of MICP type A and MICP type B. MICP type C indicates the poorest connectivity between pores. Although SEM imaging has revealed micrometer size pores within petro-type 1, poor connectivity between those pores (as indicated by MICP type C) reduces the reservoir quality of this petro-type. MICP type A (Figure 19a) indicates pore throats smaller than 3 nanometer which resulted from nanometer-size pores present in the studied rocks and as observed through SEM-imaging. MICP type B (Figure 19b) is indicative of little larger pore throat diameter and is most commonly present within petro-type 3 compared to petro-type 1 and petro-type 2. Hence, presence of rocks with MICP type B improves the reservoir quality. Such integration of petro-types with the MICP curve types improves our understanding about individual petro-types.

Petro-type	MICP 'A'	MICP 'B'	MICP 'C'
1	0%	0%	100%
2	72.5%	17.5%	10%
3	41%	51%	8%

Table 4: Distributions of different types of MICP curve within each petro-type. MICP measurements were performed on 110 samples.

Well-log Analyses

Petro-typing based on core data although are successful, one needs to correlate this petro-types to well logs as generation of such a large dataset through core plug measurement, is expensive and time consuming and is not possible every time. These problems are overcome by correlating the rock types with the log measurements from the same interval and then use these correlations along with the measured well-logs for

predicting petrophysical properties in the uncored interval. However, limited well logs from only one well (well 1) were available for this study and petro typing from well logs could not be performed. Well-logs were used in combination with core data for calculating fluid density and TOC and to identify well-log signatures of the petro-types identified from core data.

Well-log data was first shifted to core depth prior to integrating well logs with core data. Depth-shifting is critical for this highly heterogeneous rocks and it is obvious that correlation between core and well-log as well as any analyses involving both core and well-log data will improve with high precision depth shifting. In this study, depth shifting was performed through high-resolution gamma-ray correlation.

Total organic carbon (TOC)

Good correlations between TOC and ρ_b and V_p (Figure 21) indicate that these two parameters can be used to estimate TOC from well logs. TOC is calculated from both compressional velocity-deep resistivity and bulk density-deep resistivity pairs using Passey method (Passey et al., 1990). Ultimately TOC is estimated at well-log scale by taking arithmetic average from these two sources and calibrating it with the core measured TOC. This well-log derived TOC can be used in combination with Well-log measured quartz and clay content in order to identify similar rock types at well-log scale as identified based on core data.

Well-log signatures of petro-types

Petro-type 3 when plotted against deep resistivity (AT90) shows the highest resistivity values compared to petro-type 1 and type 2 (Figure 22). Intervals of petro-type

3 with high resistivity, low clay concentration, and high porosity (>6.5%) further ascertain the reservoir intervals. High resistivity values coupled with low clay concentration, high porosity, and high TOC in these intervals indicate that the high resistivities result from the hydrocarbon enrichment. Most of these intervals are located within the Middle Woodford interval, indicating that this is the most productive interval at least in this well (Figure 23). Good reservoir interval alternating with intervals of high Young's modulus and low Poisson's ratio fine tune a particular interval within the Middle Woodford as the most prolific interval for placing the horizontal well (Figure 23). Finally it can be stated that, this analyses highlight that it is possible to detect reservoir intervals within the Woodford Shale when well logs are used in combination with laboratory measured core data.

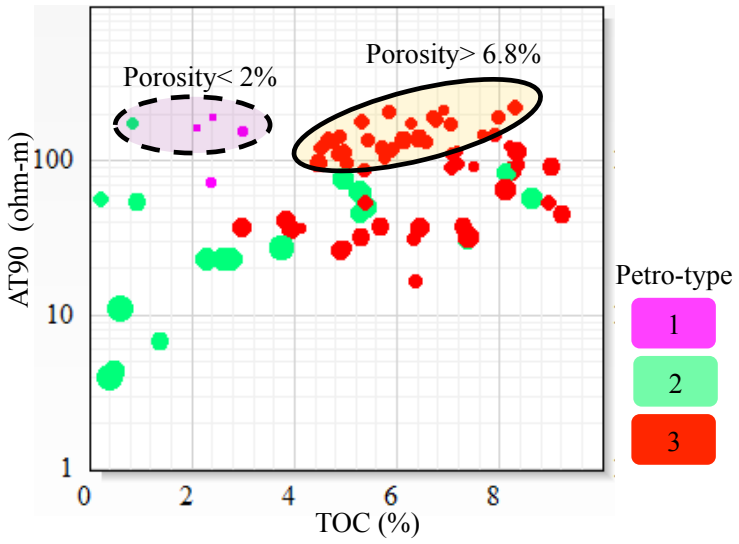

Figure 22: Crossplot of laboratory measured organic carbon (TOC) with deep resistivity from well-log (AT90). Size of the data points is equivalent to clay concentration. Data points marked by yellow ellipse indicate good reservoir rocks characterized by high porosity (>6.5%), data with purple ellipse is characterized by very low porosity (~2%).

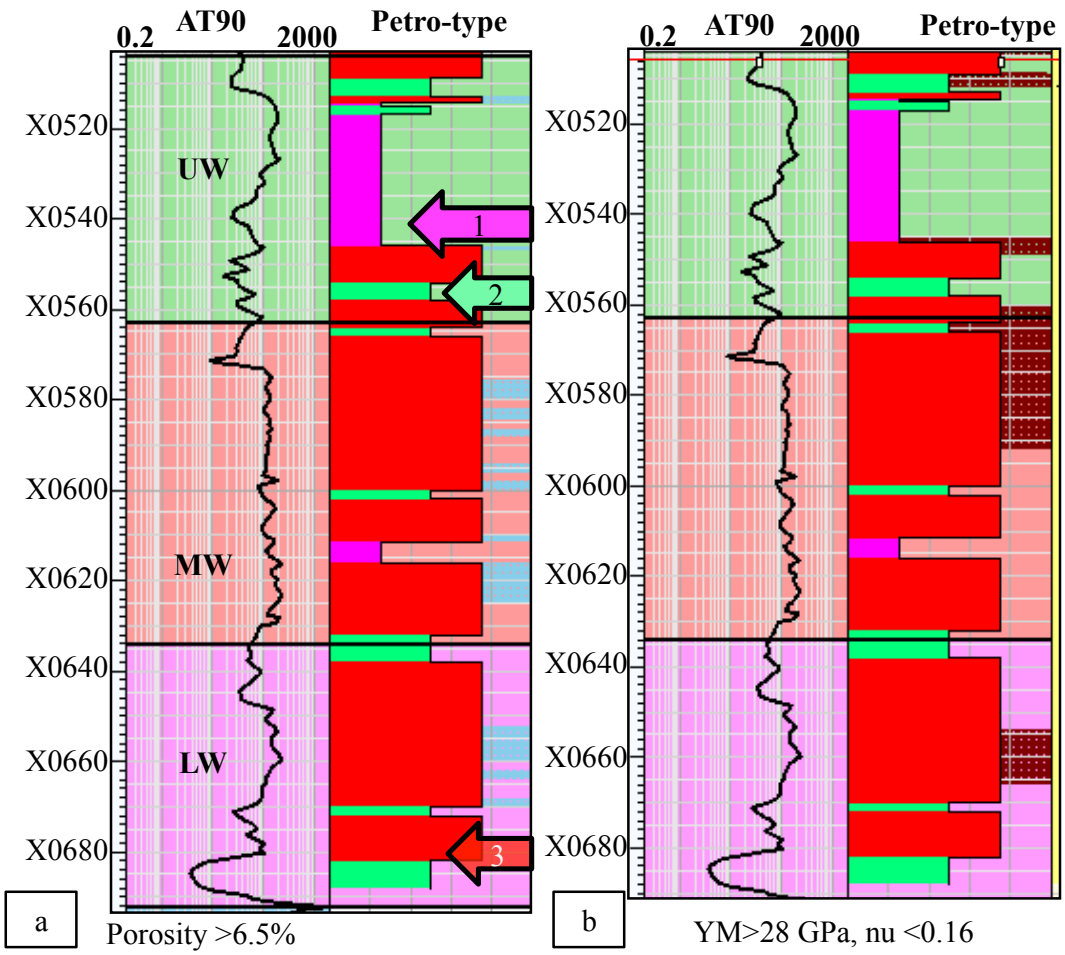

Figure 23: Distribution of the petro type 3 in well 1. Deep resistivity is plotted in track 1, petro-type is plotted in track 2. LW, MW, and UW refer to lower, middle and upper member of the Woodford Shale respectively. (a) Petro-type 3 with Φ_{He}>6.5% are highlighted with cyan in track 2. (b) Petro-type 3 with dynamic Young's modulus >28 GPa and v<0.16 are highlighted with maroon in track 2. Note, the alternating cyan and maroon intervals located within the middle Woodford member.

Conclusions

Petrophysical properties measured on carefully collected samples indicated that porosity, TOC, quartz and clay concentrations are critical parameters for identifying different rock types within the Woodford Shale play. Three petro-types have been identified through clustering analyses of these four parameters. Petro-type with intermediate clay and quartz concentrations is identified as the best reservoir rocks. Proportional increase in TOC with quartz concentration within this petro-type ensures the most brittle nature of the TOC enriched intervals.

Dynamic elastic moduli calculated from ultrasonic measurements indicate typical ductile nature of the TOC rich intervals. Hence, reservoir intervals (interval with good petro-type) with intervening brittle layers (cherty mudstone facies) are identified as sweet spots and are ideal intervals for initiating hydraulic fracturing. This is in contrast to conventional reservoirs where intervals with highest net to gross are considered as the best intervals for hydrocarbon exploration and production. Geologic analyses indicate that the cherty mudstone facies are resulted from storm-related deposits which typically follow the depressions on the basin floor making these areas good target for placing wells compared to basin floor highs which are characterized by high clay content deposited with the sediments from suspension fall out and least affected by detrital sediments from any storm/current flows (good source for detrital sediments).

Both thermal maturity and distributions of different forms of carbon control the formation of organic pores. More organic pores are developed with increasing thermal maturity. Heterogeneity in the organic matter causes different distributions of organic

carbon, which result into heterogeneous distributions of organic pores at any stages of thermal maturity.

Calibration of well logs to core data allows the proper estimation of TOC, total porosity, and fluid density from well logs. These parameters along with mineralogy data can be used for identification of different petro-types from field data.

The integrated workflow described in this study can also be applied to identify critical petrophysical parameters followed by determination of the sweet-spots within any other resource shales.

Acknowledgement

We would like to thank Cimarex Energy for providing the funding and some cores used in this study. We acknowledge the help and guidance provided by the people at the University of Oklahoma's Integrated Core Characterization (IC^3) Laboratory.

References

Amaefule, J. O., M. Altunbay, D. Tiab, D. G. Kersey, and D. K. Keelan, 1993, Enhanced Reservoir Description: Using Core and Log Data to Identify Hydraulic (Flow) Units and Predict Permeability in Uncored Intervals/Wells, SPE Annual Technical Conference and Exhibition, Houston, Texas, 1993 Copyright 1993, Society of Petroleum Engineers, Inc.

Ballard, B. D., 2007, Quantitative Mineralogy of Reservoir Rocks Using Fourier Transform Infrared Spectroscopy.

Birch, F., 1960, The velocity of compressional waves in rocks to 10 kilobars, part 1: Journal of Geophysical Research, v. 65, p. 1083-1102.

Bradley, P. S., and O. L. Mangasarian, 2000, k-Plane Clustering: Journal of Global Optimization, v. 16, p. 23-32.

Caldwell, C. D., 2011, Lithostratigraphy of the Woodford Shale, Anadarko Basin, West-Central Oklahoma: Mid-Continent Section meeting.

Comer, J. B., 2008, Distribution and Source-Rock Characteristics of Woodford Shale and Age-Equivalent Strata: AAPG Annual Convention and Exhibition.

Curtis, M. E., R. J. Ambrose, C. H. Sondergeld, and C. S. Rai, 2011, Investigation of the Relationship Between Organic Porosity and Thermal Maturity in The Marcellus Shale, North American Unconventional Gas Conference and Exhibition, The Woodlands, Texas, USA, Society of Petroleum Engineers.

EnergyInformationAdministration, 2011, Review of Emerging Resources: US Shale Gas and Shale Oil Plays, ftp://ftp.eia.doe.gov/natgas/usshaleplays.pdf.

Espitalilie, J., 1986, Use of Tmax as a maturation index for different types of organic matter. Comparison with vitrinite reflectance, *in* J. Burrus, ed., Thermal modeling in sedimentary basins: Paris, Editions Technip, p. 475-496.

Gunter, G. W., J. J. Pinch, J. M. Finneran, and W. T. Bryant, 1997, Overview of an Integrated Process Model to Develop Petrophysical Based Reservoir Descriptions, SPE Annual Technical Conference and Exhibition, San Antonio, Texas, Society of Petroleum Engineers, Inc.

Hoeve, M. V., S. C. Meyer, J. Preusser, and A. Makowitz, 2011, Basin-Wide Delineation of Gas Shale □Sweet Spots□ using Density and Neutron Logs; Implications for Qualitative and Quantitative Assessment of Gas Shale Resources: AAPG Geoscience Technology Workshop: US Shale Plays.

Jacobi, D. J., M. Gladkikh, B. LeCompte, G. Hursan, F. Mendez, J. Longo, S. Ong, M. Bratovich, G. L. Patton, and P. Shoemaker, 2008, Integrated Petrophysical Evaluation of Shale Gas Reservoirs, CIPC/SPE Gas Technology Symposium 2008 Joint Conference, Calgary, Alberta, Canada, Society of Petroleum Engineers.

Jarvie, D. M., 1991, Total Organic Carbon (TOC) Analysis, *in* R. K. Merrill, ed., Treatise of Petroleum Geology: Handbook of Petroleum Geology, Source and Migration Processes and Evaluation Techniques, American Association of Petroleum Geologists, p. 113-118.

Jarvie, D. M., R. J. Hill, T. E. Ruble, and R. M. Pollastro, 2007, Unconventional shale-gas systems: The Mississippian Barnett Shale of north-central Texas as one model for thermogenic shale-gas assessment: AAPG bulletin, v. 91, p. 475.

Johnson, K. S., 1988, Geologic evolution of the Anadarko basin, *in* K. S. Johnson, ed., Anadarko basin Symposium: Circular 90, Oklahoma Geological Survey, p. 3-12.

Kale, S., 2009, Petrophysical Characterization of Barnett Shale Play, University of Oklahoma.

Kale, S., C. S. Rai, and C. H. Sondergeld, 2010, Petrophysical Characterization of Barnett Shale, SPE Unconventional Gas Conference, Pittsburgh, Pennsylvania, USA, Society of Petroleum Engineers.

Kale, S., C. S. Rai, and C. H. Sondergeld, 2010b, Rock Typing in Gas Shales, SPE Annual Technical Conference and Exhibition, Florence, Italy, Society of Petroleum Engineers.

Kamath, J., 1992, Evaluation of accuracy of estimating air permeability from mercury-injection data: SPE formation evaluation, v. 7, p. 304-310.

Karastathis, A., 2007, Petrophysical measurements on tight gas shale, University of Oklahoma, Norman.

Lambert, M. W., 1993, Internal stratigraphy and organic facies of the Devonian-Mississippian Chattanooga (Woodford) Shale in Oklahoma and Kansas: Source rocks in a sequence stratigraphic framework: AAPG Studies in Geology, v. 37, p. 163-176.

Loucks, R. G., R. M. Reed, S. C. Ruppel, and D. M. Jarvie, 2009, Morphology, genesis, and distribution of nanometer-scale pores in siliceous mudstones of the Mississippian Barnett Shale: Journal of Sedimentary Research, v. 79, p. 848.

Matteson, A., and M. M. Herron, 1993, Quantitative mineral analysis by Fourier transform infrared spectroscopy, p. 1-15.

Newsham, K. E., and J. A. Rushing, 2001, An Integrated Work-Flow Model to Characterize Unconventional Gas Resources: Part I - Geological Assessment and Petrophysical Evaluation, SPE Annual Technical Conference and Exhibition, New Orleans, Louisiana, Copyright 2001, Society of Petroleum Engineers Inc.

Passey, Q., S. Creaney, J. Kulla, F. Moretti, and J. Stroud, 1990, A practical model for organic richness from porosity and resistivity logs: AAPG bulletin, v. 74, p. 1777-1794.

Passey, Q. R., K. Bohacs, W. L. Esch, R. Klimentidis, and S. Sinha, 2010, From Oil-Prone Source Rock to Gas-Producing Shale Reservoir-Geologic and Petrophysical Characterization of Unconventional Shale-Gas Reservoirs, International Oil and

Gas Conference and Exhibition in China, Beijing, China, Society of Petroleum Engineers.

Pittman, E. D., 1992, Relationship of porosity and permeability to various parameters derived from mercury injection capillary pressure curves for sandstone: AAPG bulletin, v. 76, p. 191-198.

Raina, I., 2010, Petrophysical Characterization of Thirteen Finger Limestone, University of Oklahoma.

Rickman, R., M. J. Mullen, J. E. Petre, W. V. Grieser, and D. Kundert, 2008, A Practical Use of Shale Petrophysics for Stimulation Design Optimization: All Shale Plays Are Not Clones of the Barnett Shale, SPE Annual Technical Conference and Exhibition, Denver, Colorado, USA, Society of Petroleum Engineers.

Rushing, J. A., K. E. Newsham, and T. A. Blasingame, 2008, Rock Typing-Keys to Understanding Productivity in Tight Gas Sands, SPE Unconventional Reservoirs Conference, Keystone, Colorado, USA, Society of Petroleum Engineers.

Sigal, R. F., 2009, A methodology for blank and conformance corrections for high pressure mercury porosimetry: Measurement Science and Technology, v. 20, p. 045108.

Sondergeld, C., and C. Rai, 1993, A new concept in quantitative core characterization: The Leading Edge, v. 12, p. 774.

Sondergeld, C. H., K. E. Newsham, J. T. Comisky, M. C. Rice, and C. S. Rai, 2010, Petrophysical Considerations in Evaluating and Producing Shale Gas Resources, SPE Unconventional Gas Conference, Pittsburgh, Pennsylvania, USA, Society of Petroleum Engineers.

Sondhi, N., 2011, Petrophysical Characterization of Eagle Ford Shale, University of Oklahoma.

Sullivan, K. L., 2006, Organic facies variation of the Woodford Shale, in western Oklahoma, University of Oklahoma.

Swanson, B., 1981, A simple correlation between permeabilities and mercury capillary pressures: Journal of Petroleum Technology, v. 33, p. 2498-2504.

Thomeer, J., 1983, Air permeability as a function of three pore-network parameters: Journal of Petroleum Technology, v. 35, p. 809-814.

Thomeer, J., 1960, Introduction of a Pore Geometrical Factor Defined by the Capillary Pressure Curve: Journal of Petroleum Technology, v. 12, p. 73-77.

Totten, M. W., 2011, Electron Probe Micro-analysis of the Woodford Shale, South-Central Oklahoma, The University of Oklahoma, Norman.

Zargari, S., M. Prasad, K. C. Mba, and E. Mattson, 2011, Organic Maturity, Hydrous Pyrolysis, and Elastic Property in Shales, Canadian Unconventional Resources Conference, Alberta, Canada, Society of Petroleum Engineers.

Chapter 2

Microstructural study of shales for evaluating reservoir properties at different thermal maturities

Abstract

A set of intrinsic properties including micrometer range grain size, nanometer range pore size, along with nanodarcy permeability of resource-shales demand sub-microscopic investigations of such rocks in order to understand the factors controlling critical reservoir parameters like gas in place and deliverability. Scanning electron microscopic (SEM) imaging is proving to be a critical tool for this purpose. Textural arrangement, distribution of pore spaces, pore sizes, pore shapes and distribution of organic matter, as well as distributions of different minerals have been investigated on the Woodford shale samples through high magnification imaging of focused ion beam milled (FIB) samples. Samples have been chosen from different thermal maturity windows (vitrinite reflectance: 0.7% to 1.6%) in order to track any physical changes of the organic matter, distributions of pore spaces in response to increasing thermal maturity.

SEM imaging reveals organic pores as the primary pore types within the Woodford Shale. While nanopores are common, few micrometer size pores have been observed. Nanometer-scale pores are also estimated from mercury injection capillary pressure experiment.

Both SEM imaging and laboratory measurements indicate that porosity increases with increasing thermal maturity. However, detail SEM analyses of samples from different thermal maturities indicate that formation of organic pores is controlled by the distributions of extractable-, convertible- and residual- organic carbon at any particular place within the organic matter. At any stage of thermal maturity, heterogeneous distribution of these three forms of organic carbons originating from either internal structure of organisms or mixing of insitu and transported organic matter, causes heterogeneous distribution of organic pores.

Introduction

Organic-rich shales have long been considered as source rock until the advent of shale-gas exploration. Owing to the higher oil price compared to gas, nowadays resource-shales are being explored for liquid hydrocarbon as well. Typical characteristics of the resource-shales include fine grain size (few nanometer<grain size<65 μm) (Loucks et al., 2009), high concentration of organic matter, with thermal maturity ranging from mature to post-mature. SEM imaging allows the visual inspection of the fine-scale (nano-meter range) constituents of the resource-shale. Although SEM imaging captures only an extremely small portion of the highly heterogeneous resource shales, for the current study pore sizes observed through SEM imaging matched with the macroscopic averaging measures of pore bodies through nuclear magnetic resonance (NMR) relaxation and of pore throats through high pressure mercury injection. Such dimensional consistency between macroscopic measurements and fine-scale observations though SEM imaging

indicate that indeed the objects controlling critical reservoir attributes are small and have been captured through SEM imaging.

Changes in thermal maturity affects both physical and chemical properties of the organic matter which in turn affects the overall rock properties as the low-density organic matter occupy significant rock volume. Sometime heterogeneity of the starting organic material makes it difficult to solely recognize the effect of thermal maturity. SEM imaging provides a tool to correlate such micro-scale changes with the macro-scale laboratory measurements.

Sample preparation

We have examined Woodford Shale samples from five wells located within 1500 square miles in Oklahoma. Samples were examined with petrographic microscope and SEM imaging. Ultra-thin, 30-micron thick thin sections were prepared impregnated with blue dye. Rock textures, along with some microcracks were identified; however, no pores were visible through this technique.

Small pieces of samples closely resembling the rocks at the equivalent depths were collected for the SEM imaging. Special techniques were applied to image the nanometer size pores present within the highly heterogeneous resource shale. A surface perpendicular to the bedding plane was first simply grounded and polished, which generated a roughly polished surface as the softer materials were selectively removed in the process. The next step was to ion mill the surface; however, the common Ar^+ milling systems generated “curtains” which are ridges on the milled surface (Curtis et al., 2010). At this stage, focused ion beam (FIB) integrated within a SEM was used to handle the

problem and get good high-magnification images. The FIB uses a Ga+ ion source, which was accelerated at high voltage with variable ion beam current to remove material and generate extremely flat surface without polishing mark. Images of the milled surface were taken using backscattered electrons (BSE) to differentiate different constituents.

A set of petrophysical properties have been collected from samples from the same depth for correlating microstructural properties with the bulk rock petrophysical parameters, such as: porosity, bulk density, grain density, mineralogy, ultrasonic velocities (compressional and shear wave velocities), mercury injection capillary pressure (MICP) along with total organic carbon content (TOC), rock-eval pyrolysis, and vitrinite reflectance.

SEM imaging

SEM imaging helps to analyze textural arrangements between different constituents, location of pore spaces, along with size and shape of pores critical for reservoir assessment of the resource shales. Detail understanding about the location, internal structure, shape, size of pores imaged through SEM helps to generate appropriate fluid flow model. We have broken our discussion into: (i) Textural pattern, (ii) pores, and (iii) thermal maturity, in order to build a thorough understanding about these components along with the effect of thermal maturity on these parameters within the Woodford Shale.

Textural information

Rock forming elements have been classified into four groups, which are useful for textural analyses of the resource-shales, such as: organic matter, pores, clay minerals and non-clay inorganic material. Organic matter, primarily present in amorphous form, shows

conformable boundaries between organic matter and inorganic particles. Such boundaries indicate that the starting organic material was soft and got squeezed into the inter-granular space with continued burial (Figure 24). In this way, almost all pore spaces got occupied by organic matter in this organic rich Woodford Shale. Imbrication of the floating clay particles within organic matter further support this hypothesis of flowing organic matter. Absence of hard shell at the time of deposition has resulted into such amorphous organic matter. Marine planktonic algae, radiolarian are identified as sources of organic matter in this shale (Chapter 4). Most of the radiolarian tests got dissolved at the sediment-water interface owing to the unstable silica (Schieber, 1996). However, some of the organic matters are identifiable through petrographic analyses as well as low magnification SEM images, owing to the early diagenetic silicification. Both diagenetic as well as detrital minerals are observed at the SEM images.

Clays are present as clay laminae, which get deformed next to the larger, and heavier grains. Such bedding parallel clay imbrication can be seen in Figure 25a, b, c, e. Originally, these clay particles might have deposited as clay floccule with random orientation of clay minerals (Schieber et al., 2007). The Woodford Shale lacks any bedding parallel laminae and appears as massive mudstone for intervals with clay concentrations below certain threshold. Clay particles are randomly oriented in intervals with lower clay concentrations as well as intervals with diagenetic clays. Such randomly oriented clays can decrease the host shale's elastic anisotropy when present in a significant number.

The non-clayey inorganic material covers a wide range of grain size from coarse silt (>30 μm) to fine clay (<4 μm). Presence of such clay size non-clayey minerals along

with silt-sized materials provides an overall grain-supported appearance of all the rock types at low-magnification backscatter images (Figure 26).

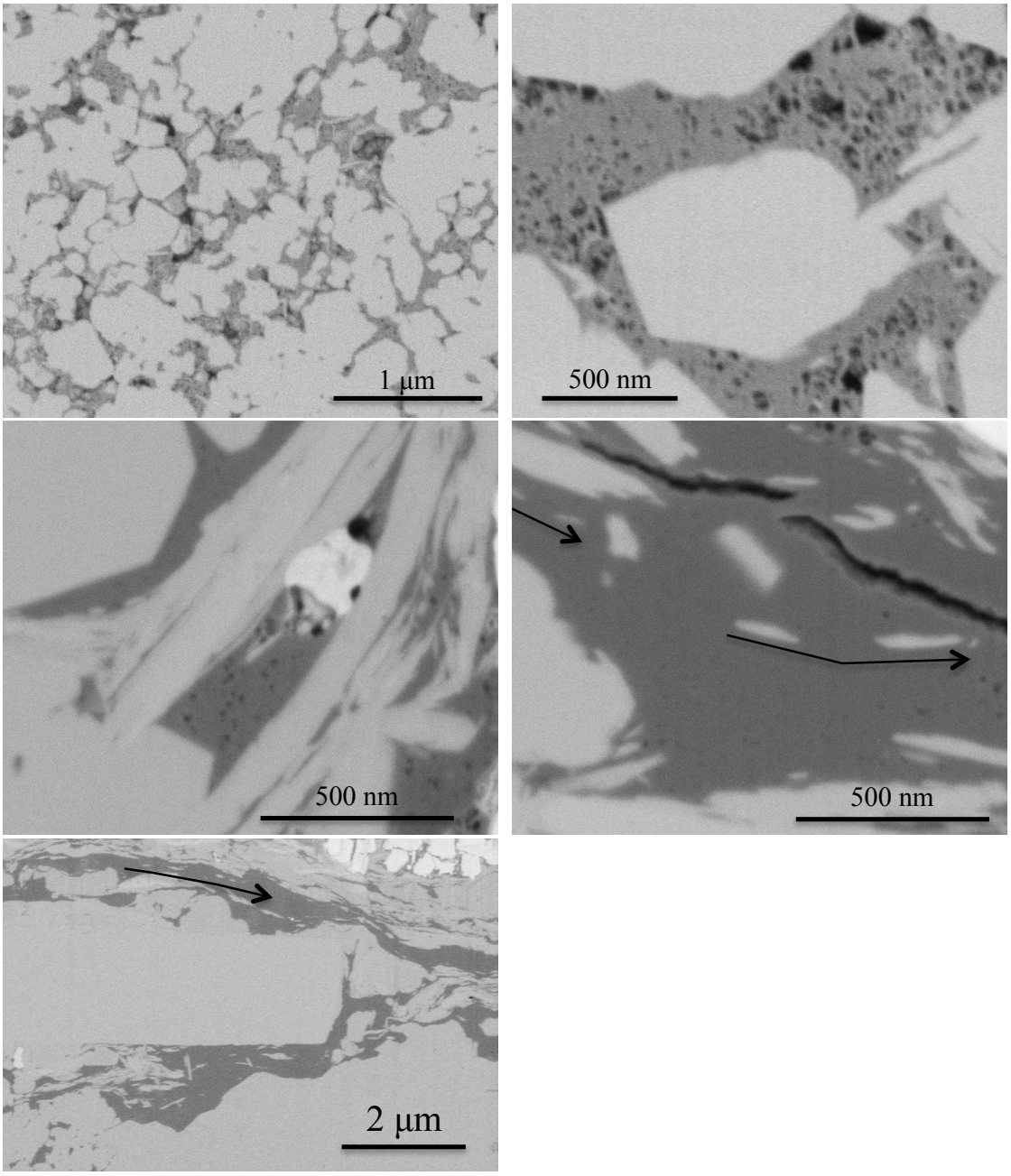

Figure 24: Backscatter electron images of focused ion-milled surfaces. Dark gray materials are organic matter, black areas are pores and rests are other inorganic minerals. Note, organic matter nicely conforming the grain boundaries of inorganic material and occupying the inter-granular spaces visible at different magnification. Black arrows indicate imbrication of floating clay particles within the organic matter indicating stream-like flow of the organic matter.

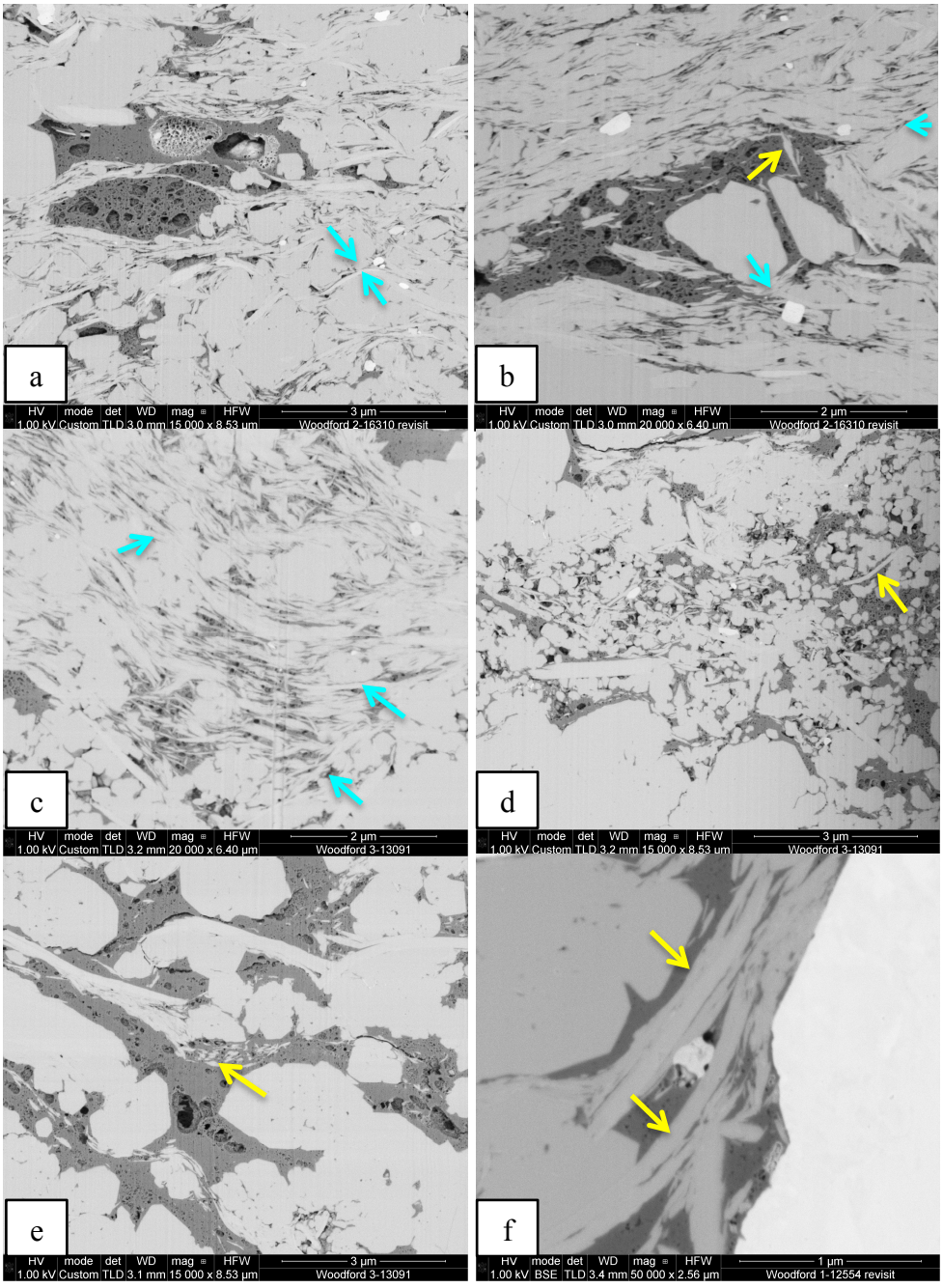

Figure 25: Backscatter electron images showing clays with detrital (cyan arrows) and diagenetic origin (yellow arrows). Figure c, and d are showing imbricated detrital clays and randomly oriented diagenetic clays in different areas of the same sample. Dark gray areas are organic matter.

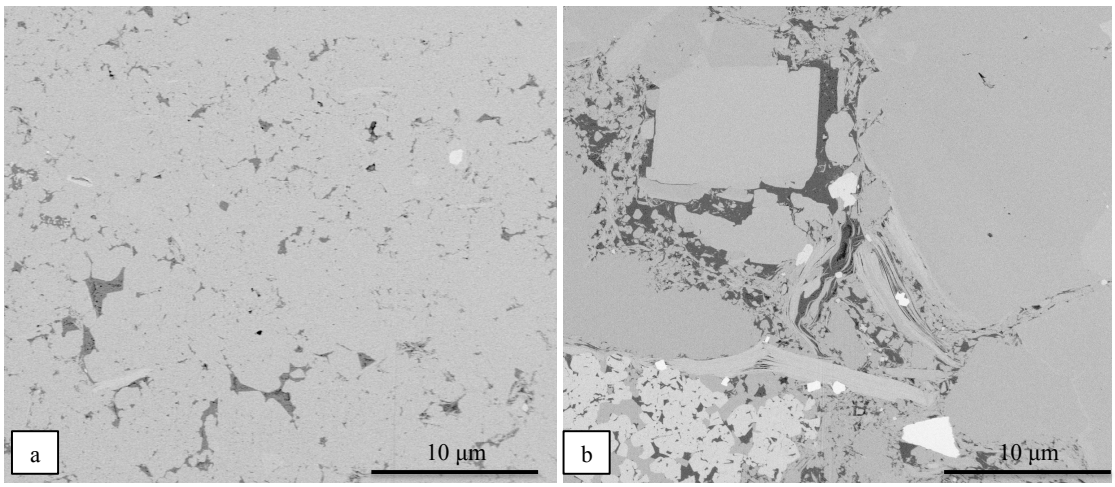

Figure 26: Backscatter electron images of samples with low- (28%) and high-(62%) clay content respectively in Figure a and b. Note, the overall grain-supported appearance of both samples at low magnification. Sample in Figure 'a' came from X597ft, and sample in Figure 'b' came from XX250ft. Horizontal scale is same in both the images.

Pore spaces

Porosity of the Woodford Shale in the study area ranges from 0% to 10%. SEM imaging reveals that organic pores (Figure 27a through g) are the most common pore-types with very few inorganic pores (Figure 27h, i). Such observations confirm that organic matter occupied most of the inter-granular spaces and thus destroyed any inter-granular the pore spaces before significant burial. Modal analysis of organic pores visible on the SEM images reveal good correlation between the organic pores and the laboratory measured porosity (Figure 28). Curtis et al. (2010b), Loucks et al. (2009) have observed organic pores as the most common pore types in other resource shales as well.

Few inorganic pores were observed at irregular grain boundaries (Figure 27i), spaces between individual clay particles, as well as in the form of microcracks.

Nanometer scale pores, observed at SEM scale matches with the interpretations made from capillary pressure experiments. However, caution should be taken prior attempting generalized interpretations from SEM-scale observations as SEM imaging captures only an extremely small portion of the highly heterogeneous resource shales.

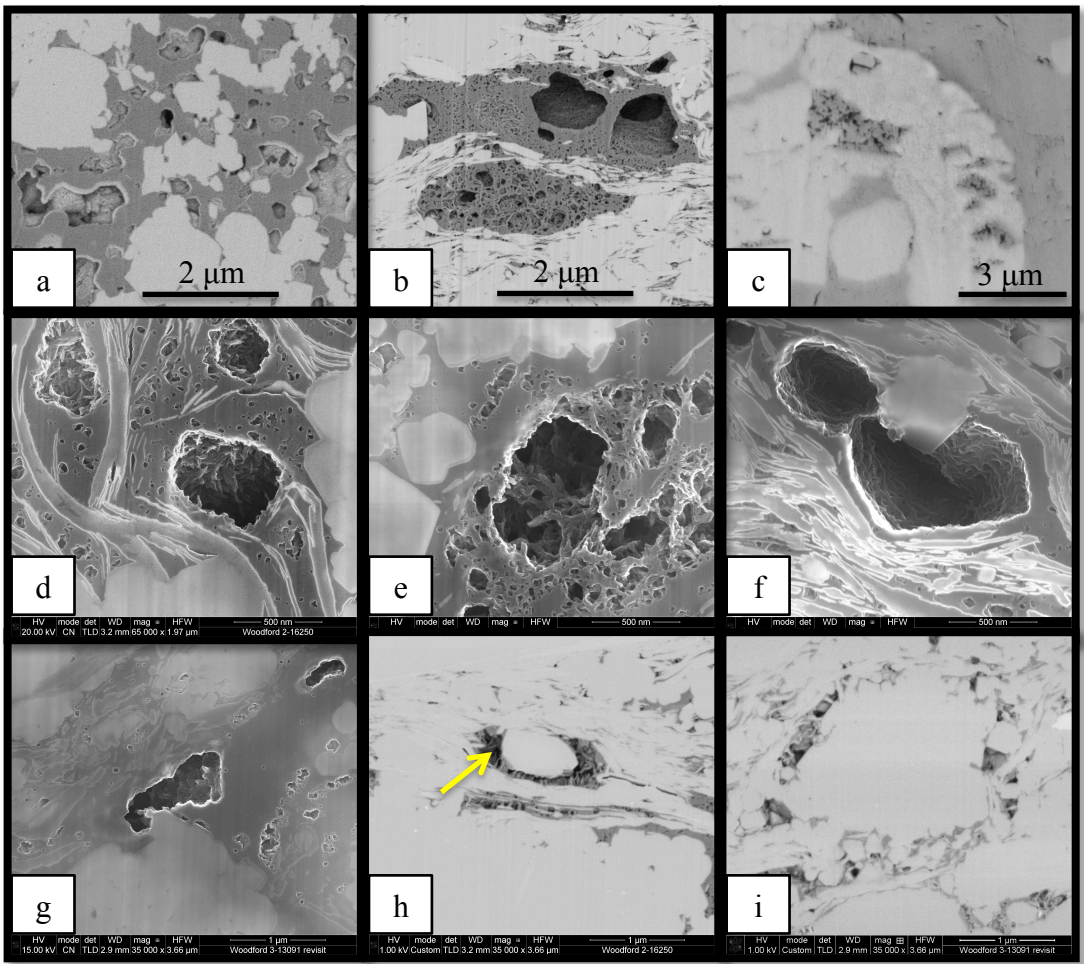

Figure 27: Backscatter electron images showing distribution of pores in the Woodford Shale. Figure 'a', 'b' show backscatter images of organic-pores in samples from two wells. Figure 'c' shows organic matter present within a fossil; porosity developed inside that organic matter. Figure d, e, and f shows detailed structures of the organic pores. Figure 'g' shows pores formed within the bitumen. In Figure 'h', pore spaces have developed at the boundary of a quartz grain and organic matter (dark grey). Figure 'i' shows inorganic pore developed at the irregular grain boundary. Organic matter in the underlying layer is visible through the empty pore space.

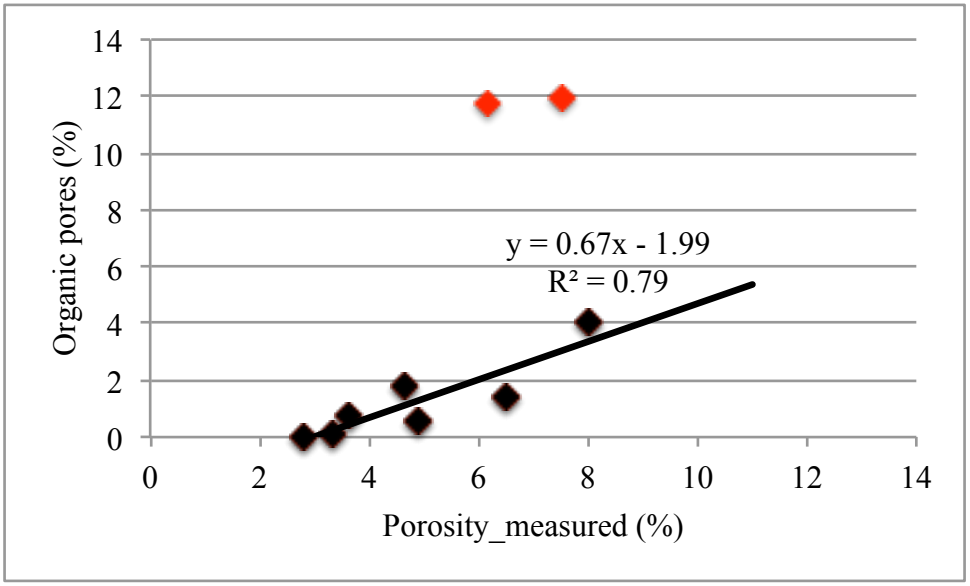

Figure 28: Crossplot of organic pores calculated from the modal analysis of the SEM images and laboratory-measured porosity. High correlation between the two indicates organic pores as the most common pore type in the studied rock. Two outlying points (shown in red) are from samples, which were highly photogenic, thus biasing our attention towards the organic pores.

Large variations of the organic pore-size, -shape as well as their heterogeneous distributions observed at SEM-scale further complicate reservoir evaluation process. Most commonly, pores although are within nanometer-scale, vary from few nanometer to few 100s of nanometer (Figure 27b, d, g, and Figure 29). Shape of the organic pores also varies from semi-circular (Figure 27, Figure 29) to high aspect ratio micro-crack shape (Figure 30). High magnification images also reveal that the studied shale is characterized by complex internal pore structures (bird's nest like structure) (Figure 27d, e, Figure 29) instead of tubular pores. Such complex internal pore structure is expected to improve connectivity between different sizes of pores as observed in Figure 27b, Figure 29.

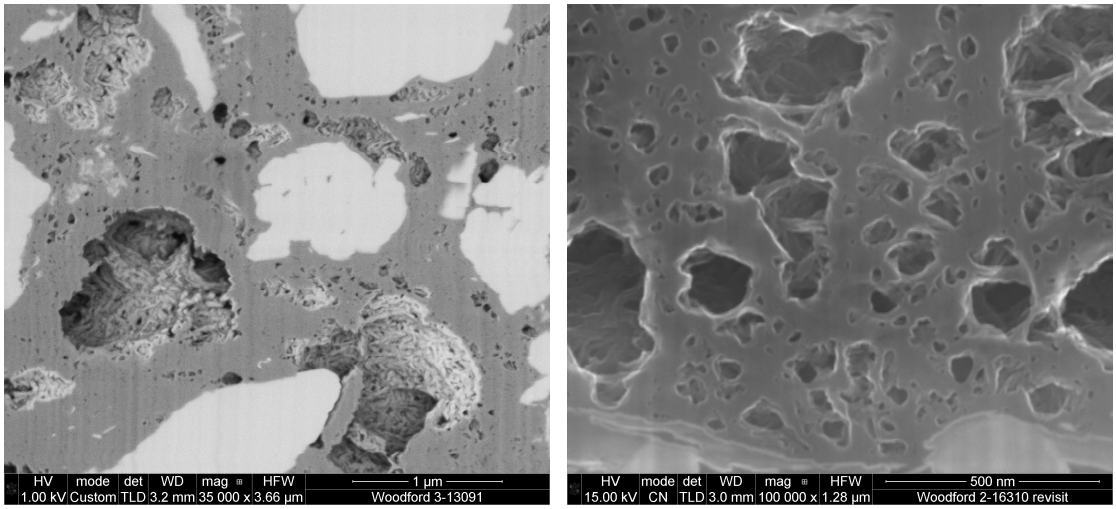

Figure 29: Backscatter electron images showing different sizes of pores even within same piece of organic matter.

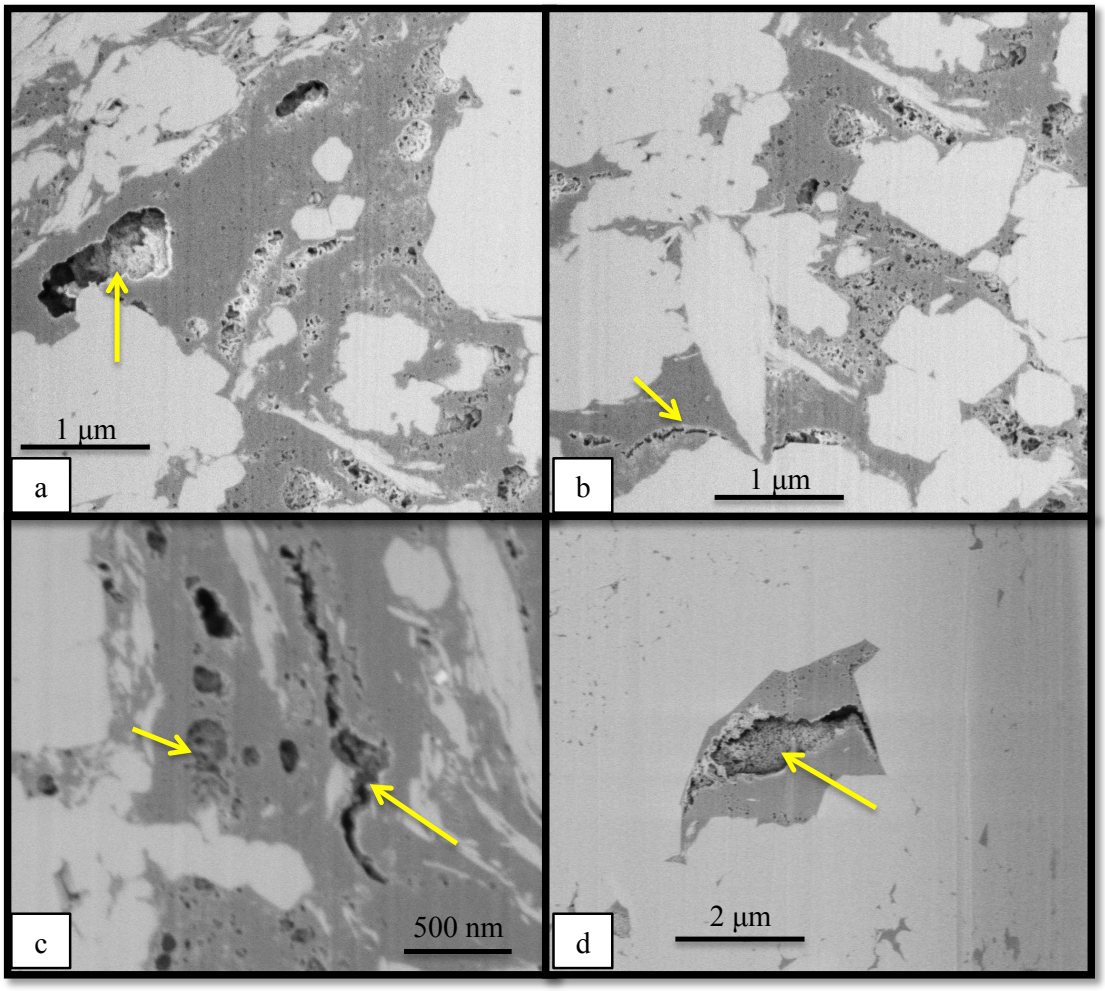

Figure 30: Backscatter electron images showing different shapes of the organic pores. Note, the shape varies from almost circular to crack-shape with high aspect ratio. In Figure 'c' mineral growth connecting either side of the open space ensuring the intrinsic origin of these pores.

Thermal maturity

We have studied the Woodford Shale for thermal maturity varying from oil window (R_o 0.7%) to wet gas condensate window (Ro 1.72%) in order to track the impact

of increasing thermal maturity on overall rock architecture. Figure 31 shows examples of organic pores at different thermal maturity.

Limited numbers of pores have been identified within organic matter with R_o 0.7%. Micro-crack like pores (Figure 31b) at the boundary between organic matter and inorganic minerals have been observed at this low maturity samples. Micro-crack like pores also have been reported at low thermal maturity during hydrous pyrolysis experiments on the Woodford Shale (O'Brien et al., 2002). On the other hand, abundant organic pores are observed in samples with higher maturity values (Figure 31c, d). Laboratory measured porosity on 200 samples show overall higher porosity at higher thermal maturity compared to samples with lower maturity and equivalent TOC (Figure 32).

Despite of the overall increase in organic pores with increasing thermal maturity, Figure 31e and f document lots of organic pores in samples with low thermal maturity (R_o 0.7%); both figures are taken from the same sample. Figure 31f shows micrometer size organic pores within a cherty mudstone sample. Visual inspections of the core reveal that such pore spaces are characteristic of the cherty mudstone facies. This cherty mudstone facies are typically few centimeters thick and are not easily distinguishable in rock samples, as they appear as shiny black rocks in a black background (black mudstone facies) (Figure 31g). The non-linear boundary between the cherty mudstone facies and the background black mudstone facies indicates that deposition of the cherty facies was associated with high energy flow; hence, different types of organic matter representing a mixture of both in-situ as well as transported organic matter are expected within this lithofacies. Presence of large micrometer size organic pores within the cherty facies at

low thermal maturity indicates that the development of organic pores is not solely controlled by the thermal maturity.

SEM imaging also reveals heterogeneous distribution of the organic pores even at a given thermal maturity. For example, Figure 31c documents preferential development of pore spaces in some areas of the same piece of organic matter. Such preferential porosity development most likely reflects compositional differences within the organic matter. For example, Totten (2011) has imaged different type of organic material forming the outer rim of a spore compared to the material inside it.

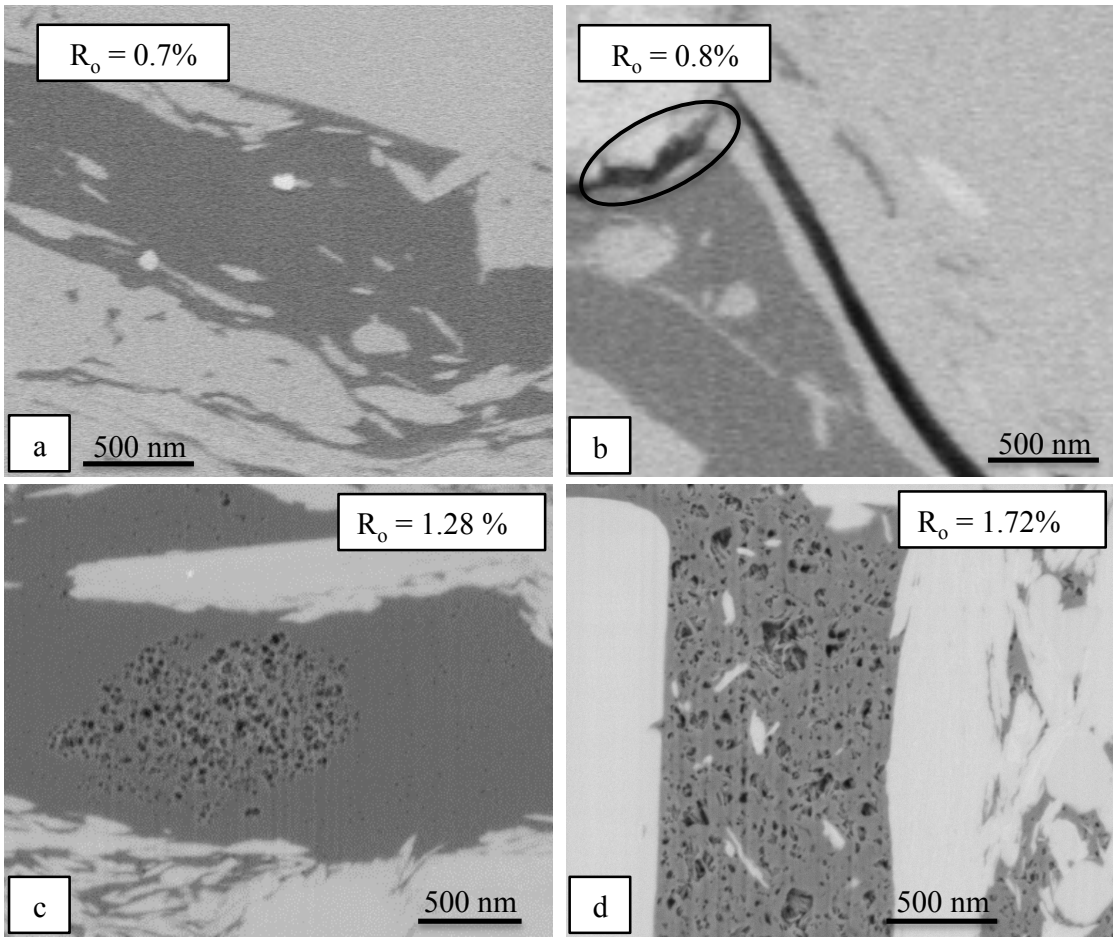

Figure 31: Backscatter electron images of samples from different thermal maturity. (a, b) samples are in the oil-window, showing almost no organic pores except for a microcrack like pore marked by the black ellipse in Figure b, (c, d) higher maturity (wet gas-condensate window) sample with lots of organic pores. (c) Preferential pore space development in the same piece of organic matter. (e) and (f) Picture taken from the same sample with thermal maturity in the oil window. Figure f shows micron size pores. (g) Left figure is a picture of a hand specimen showing the cherty layer bounded by the two red lines. A dime has been kept for scale. The right figure is a schematic diagram showing the centimeter thick chert layer.

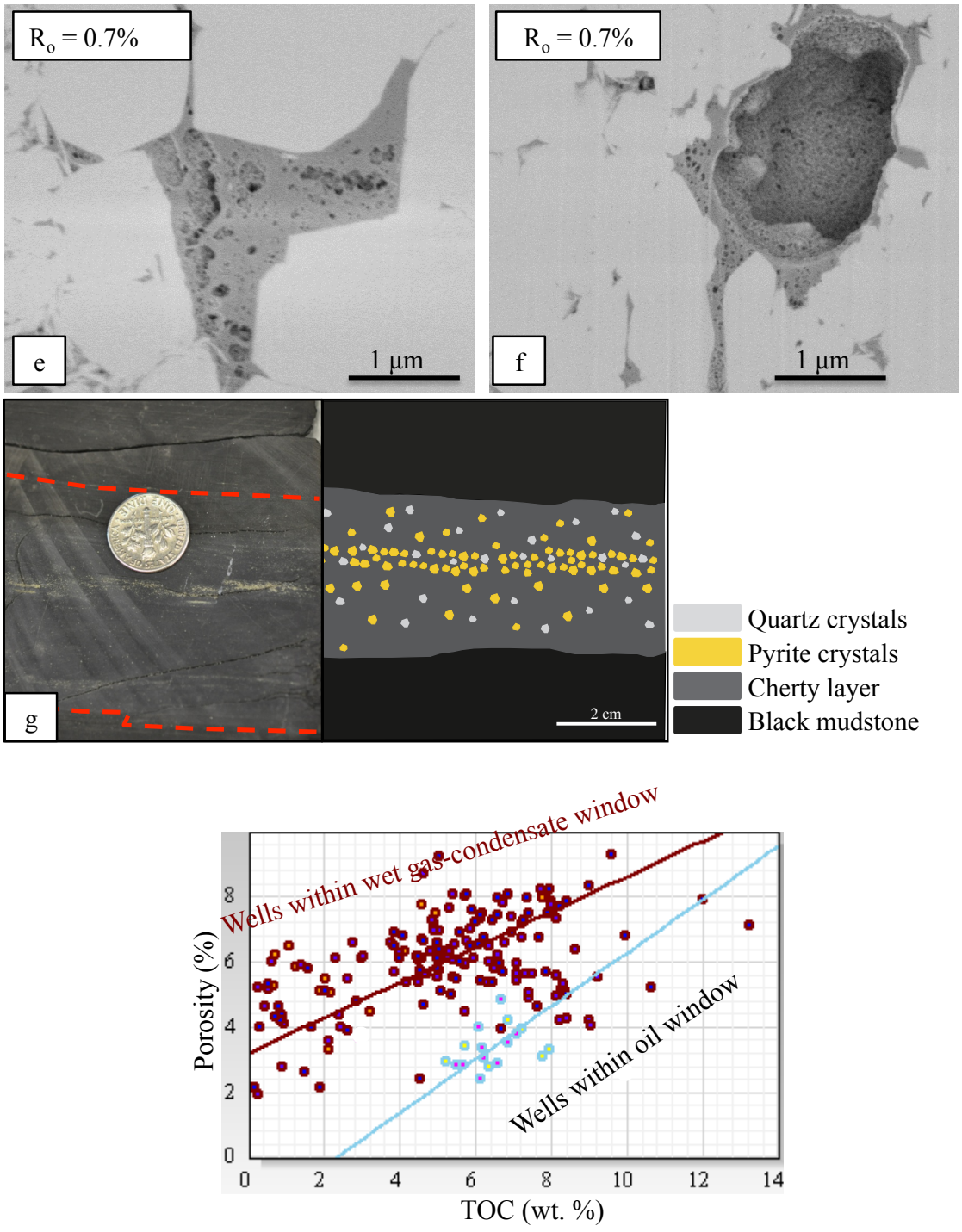

Figure 32: Crossplot of laboratory measured porosity and total organic carbon (TOC) showing overall low porosity for less mature wells compared to highly mature wells.

Here we propose a possible mechanism for the formation of organic pores that can explain the heterogeneity of the distribution of organic pores. Jarvie (1991) documented three forms of organic carbon such as: (i) extractable organic carbon (EOM), (ii) convertible carbon, and (iii) residual carbon. Ratios between these three forms of organic carbon control the organic pore formation within organic matter. With increasing thermal maturity hydrocarbon is generated from EOM while some convertible carbon gets converted to EOM and fill up the void space created by the expulsion of hydrocarbon (Figure 33). Hence, organic pores are developed only when the convertible organic carbon concentration has dropped so much that it cannot fill up all the void spaces created by the expulsion of hydrocarbon from EOM. Hydrous pyrolysis experiment by Zargari et al. (2011) documented that the starting solid organic matter expands voluminously and almost cover the whole surface at the early stage of thermal maturity (Figure 34). This accounts for the expandable nature of the convertible organic carbon at the early stage of thermal maturity. At later stage of thermal maturity, organic matter hardens, although surface area increases through formation of organic pores (Figure 34). The proposed mechanism also explains that organic pores will generate at much earlier stage within organic matter containing high EOM and high EOM/convertible organic carbon compared to organic matter with similar EOM but lower values of EOM/convertible organic carbon.

Different sizes of pores in Figure 27d, Figure 27e, Figure 29 must have resulted from multi-stage hydrocarbon expulsion from the sample. Hydrocarbon is first generated from the most labile part of the organic matter and hence, pores are first created in those areas of high labile carbon; with progressive increase in thermal maturity hydrocarbon

starts to get out from less labile part and initiate small size pores in new areas while the pores those were generated before grows bigger.

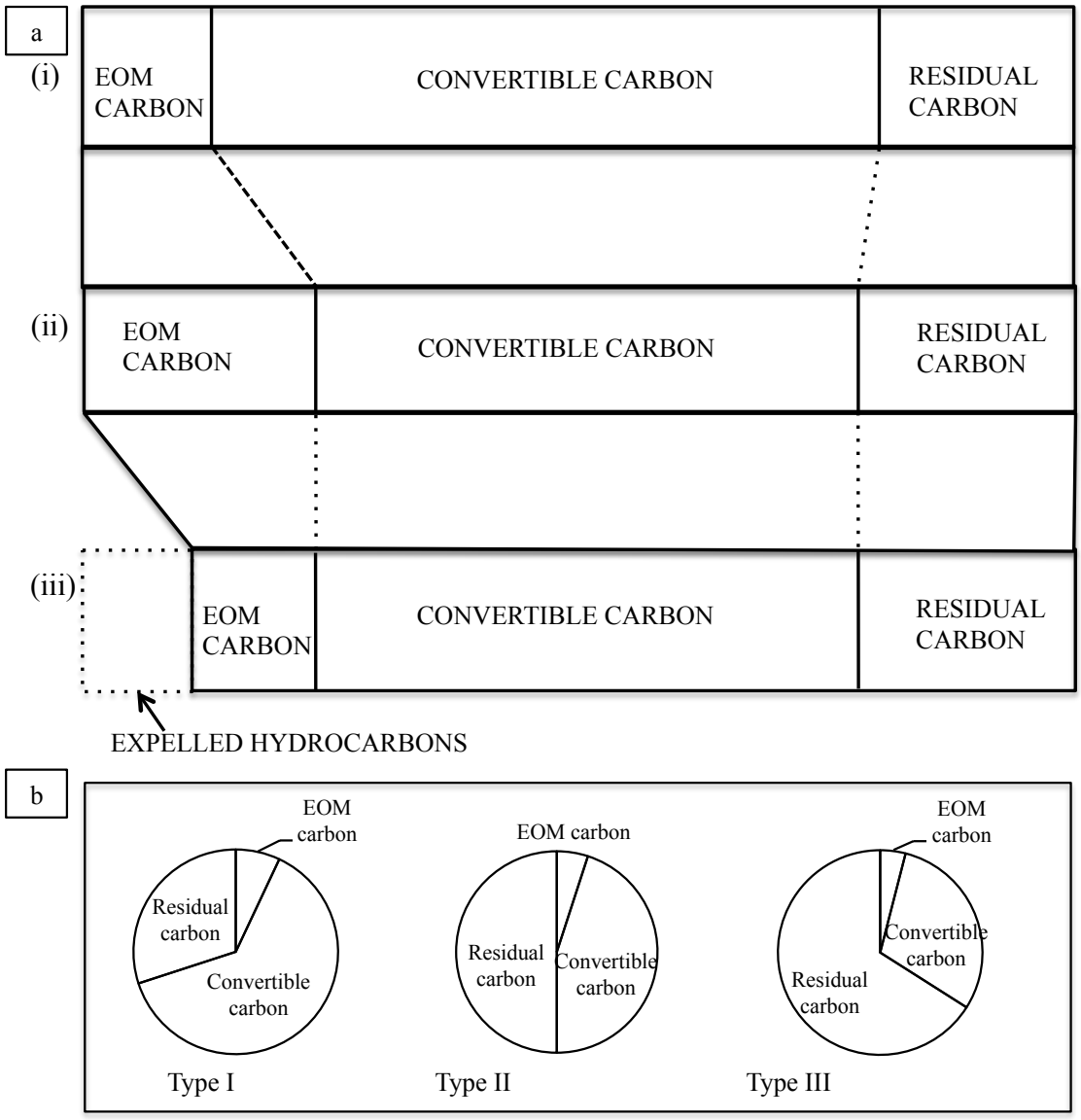

Figure 33: (a) Effect of thermal maturation on a given volume of organic carbon: (i) with increasing thermal maturity, the initial EOM and convertible carbon amounts are changed as a result of generation, (ii) EOM carbon increases at the expense of the convertible carbon, (c) with expulsion, the original TOC value is decreased by the amount of carbon contained in the expelled EOM carbon fraction. The residual carbon increases slightly with maturation. (b) Typical distributions of different forms of carbon in different kerogen types. Modified from Jarvie, 1991.

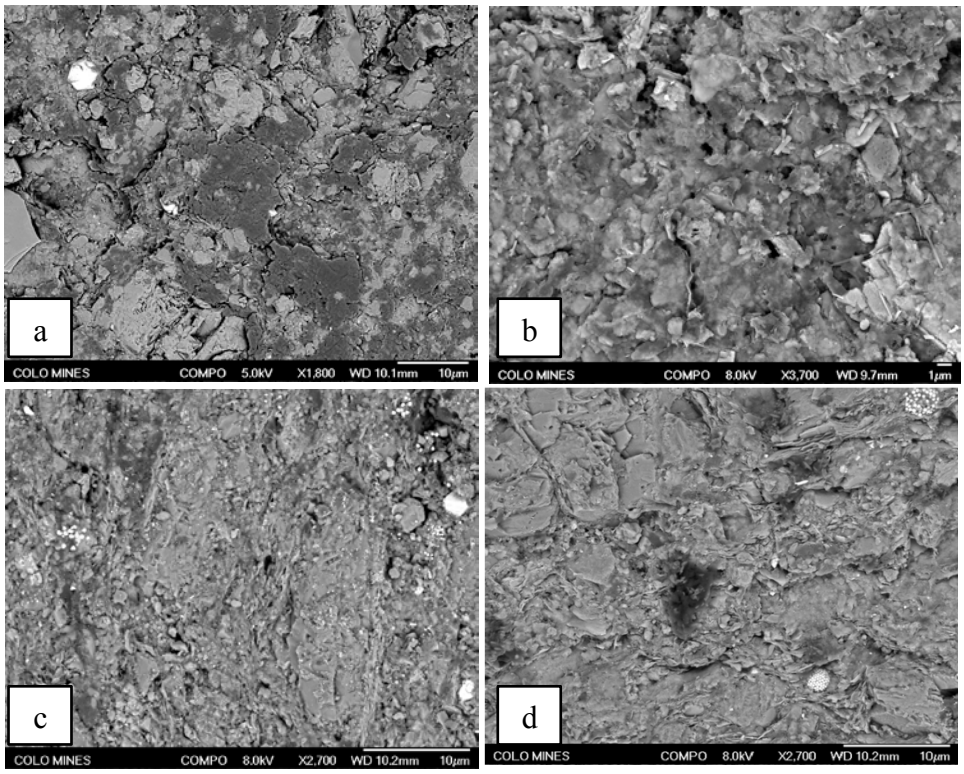

Figure 34: SEM images showing effect of hydrous pyrolysis on samples from the Bakken Shale with varying thermal maturity. (a) and (b) before pyrolysis and after pyrolysis of a sample with Tmax = 431.2°C, showing dramatic change in distribution of organic matter. Figure 'b' shows that the generated hydrocarbon in cooked sample covers most grains; whereas in the natural state sample (Figure 'a'), darker colored kerogen can be distinguished from lighter colored grains. (c) and (d) before pyrolysis and after pyrolysis of a sample with Tmax = 457.1°C showing minor changes after pyrolysis (Figure d) compared to the natural sample (Figure c). Modified from Zargari et al., 2011.

Conclusions

Micro-scale inspections have revealed a set of characteristic features of the Woodford Shale that are important for understanding the reservoir characteristics of this resource shale. It was possible to integrate SEM observations made from a number of samples with petrographic analysis and laboratory measured petrophysical properties in order to quantitatively analyze the SEM observations. Although SEM imaging captures only an extremely small portion of the highly heterogeneous resource shales, it provides detail understanding about the internal pore structure, connectivity etc..

Organic pores are identified as the most common pore type within the Woodford Shale. Pores of inorganic origin occur at irregular grain boundaries, interstitial spaces between individual clay platelets, as well as microcracks.

Combination of SEM imaging and petrophysical analyses indicates that the amount of organic pores increase with increasing thermal maturity. Heterogeneity in the starting organic material causes heterogeneous distribution of EOM, convertible and residual organic carbon, which in turn causes heterogeneous porosity distribution even within the same piece of organic matter.

SEM imaging revealed that the Woodford Shale is characterized by two sources of clays: detrital and diagenetic. Detrital clays are imbricated and forms parallel laminae if not distorted by the surrounding larger and heavier grains. Diagenetic clays are randomly oriented and decrease the shale anisotropy.

References

Curtis, M. E., C. H. Sondergeld, R. J. Ambrose, and C. S. Rai, 2010, Microstructural Observations in Gas Shales: AAPG Hedberg Conference.

Curtis, M. E., R. J. Ambrose, and C. H. Sondergeld, 2010b, Structural Characterization of Gas Shales on the Micro- and Nano-Scales, Canadian Unconventional Resources and International Petroleum Conference, Calgary, Alberta, Canada, Society of Petroleum Engineers.

Jarvie, D. M., 1991, Total Organic Carbon (TOC) Analysis, *in* R. K. Merrill, ed., Treatise of Petroleum Geology: Handbook of Petroleum Geology, Source and Migration Processes and Evaluation Techniques, American Association of Petroleum Geologists, p. 113-118.

Loucks, R. G., R. M. Reed, S. C. Ruppel, and D. M. Jarvie, 2009, Morphology, genesis, and distribution of nanometer-scale pores in siliceous mudstones of the Mississippian Barnett Shale: Journal of Sedimentary Research, v. 79, p. 848.

O'Brien, N. R., M. D. Cremer, and D. G. Canales, 2002, The Role of Argillaceous Rock Fabric in Primary Migration of Oil: Transactions-Gulf Coast Association Of Geological Societies, v. 52, p. 1103-1112.

Schieber, J., 1996, Early diagenetic silica deposition in algal cysts and spores; a source of sand in black shales: Journal of Sedimentary Research, v. 66, p. 175-183.

Schieber, J., J. Southard, and K. Thaisen, 2007, Accretion of Mudstone Beds from Migrating Floccule Ripples: Science, v. 318, p. 1760-1763.

Sondergeld, C. H., R. J. Ambrose, C. S. Rai, and J. Moncrieff, 2010, Micro-Structural Studies of Gas Shales, SPE Unconventional Gas Conference, Pittsburgh,

Pennsylvania, USA, Society of Petroleum Engineers.

Totten, M. W., 2011, Electron Probe Micro-analysis of the Woodford Shale, South-Central Oklahoma, The University of Oklahoma, Norman.

Zargari, S., M. Prasad, K. C. Mba, and E. Mattson, 2011, Organic Maturity, Hydrous Pyrolysis, and Elastic Property in Shales, Canadian Unconventional Resources Conference, Alberta, Canada, Society of Petroleum Engineers.

Chapter 3

Seismic attribute driven integrated characterization of the Woodford Shale in west-central Oklahoma

Abstract

This study focuses on regional characterization of the prolific Woodford Shale play in west-central Oklahoma. I combine seismic attributes, pre-stack inversion, well logs and core information with principles of seismic geomorphology to define the overall basin architecture and major stratigraphic changes. Overall, the Woodford Shale is TOC-rich silty shale. Seismic attributes highlight rugged topography of the basin floor of the Woodford Sea, which controlled the lateral and vertical distribution of different lithofacies containing variable amount of TOC and also brittleness. Depressions on the basin floor are characterized by TOC-lean cherty lithofacies at frequent depth intervals providing TOC-lean brittle and TOC-rich ductile rock couplet compared to basin floor highs characterized by overall ductile lithofacies.

High curvature values in basin floor depressions indicate higher number of natural fractures further improving hydrocarbon deliverability of the studied rock in such areas. Seismic data indicates that both the Woodford Shale and the underlying Hunton Limestone are affected by multi-stage tectonic deformations and thus resulting into hetreogenous distribution of natural fractures. Higher number of natural fractures are associated with complex structures such as highly curvilinear fault planes, rotated fault

blocks, areas with high curvature values as highlighted by recently developed volumetric seismic attributes.

Petrophysical properties extracted from the seismic data and calibrated with the core measurements and well logs help to quantitatively define different petro-types, which in turn identify potential sweet spots within the study area.

Introduction

The Late Devonian Woodford Shale was deposited in an epeiric sea covering a wide area in the southern midcontinent. Regionally the Woodford Shale play is divided into three parts: Woodford, Cana-Woodford of the Midwest and Barnett Woodford of the Southwest, with estimated technically recoverable resource of 22.21 TCF, 5.72 TCF and 32.15 TCF respectively (EIA, 2011). Current study focuses on the Woodford Shale of the Midwest (Figure 35) where the shale is reported to produce dry gas, condensate, and oil and has an average thickness of 200 ft. In the study area the Woodford Shale exhibits complex and heterogeneous geophysical characteristics owing to the lithologic heterogeneity. Our goal is to identify areas with favorable lithology and geomorphologic characteristics for producing hydrocarbon from the studied shale.

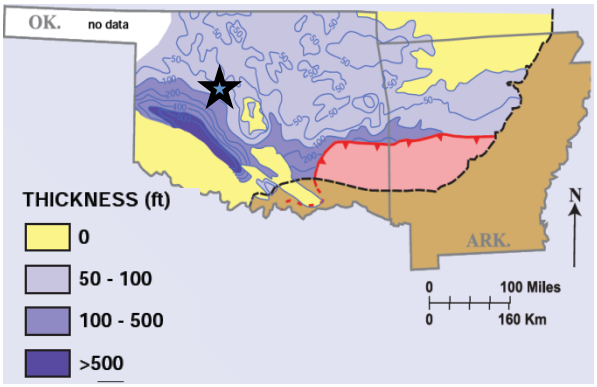

Figure 35: Thickness map showing the distribution of the Woodford Shale in Oklahoma. The asterisk shows the study area. Map modified from Comer (2008).

In this paper, I present a workflow for the regional characterization of the resource shales. I start with integrated seismic geomorphologic analyses and geologic history in order to highlight sequential stratigraphic changes controlling the distribution of different lithofacies and organic matter (TOC) richness. Next I present geomorphologic analyses in order to highlight areas of natural fracture concentrations critical for hydrocarbon deliverability of the tight resource shale. Ultimately, I present a comparison between petrophysical properties extracted through simultaneous prestack seismic inversion, well logs and core measurements.

Geomorphologic setup

We have used seismic attributes to highlight the overall basin architecture. Pre-depositional basin geomorphology carved the basin floor of the Woodford Sea and thus controlled the distributions of different lithologies affecting the resource potential of the studied shale. Multi-stage tectonic deformation carved the post-depositional

geomorphology. In this section we will focus on the pre-depositional basin geomorphology and it's effect on the lithologic distributions.

Time structure maps (Figure 36) of the Woodford Shale and the underlying Hunton Limestone show an overall flat topography with structural dips less than 2°. Time Structure maps reveal that the palaeo shoreline was located toward the northeast while the basin depocenter was located toward the southwest. Time thickness map (Figure 37) of the Woodford Shale indicate no correlation between the thickness of the Woodford shale and paleo contour maps shown by the time structure maps in Figure 36. We have flattened the seismic volume along the top of the Woodford in order to remove the effect of post-depositional architectural overprint and extract the original basin geomorphology at the time of Woodford deposition for further analysis. Vertical slices through the 3D seismic amplitude volumes (Figure 38) show a number of faults extending through these stratigraphic intervals indicating that major tectonic activities have affected the Woodford Shale in the study area. Figure 39 shows a set of volumetric attributes highlighting the basin floor topography of the Woodford Sea. Low coherent seismic energy (Figure 39b), low $\mu\rho$ values (Figure 39e) indicate the Woodford Shale deposited in areas inundated at earlier stage of Woodford Sea transgression and high values indicate remnant Hunton Limestone. Horizon slice through the co-rendered high curvature values and coherent seismic energy (Figure 39d) indicate high curvature values in juxtaposition with areas with high seismic energy. Such correlations indicate high curvature values are associated with collapse of the Hunton Limestone. Geologic history indicates that a prolonged period of non-deposition and associated erosional activities created a very irregular topography at the top of the Hunton Limestone, which became the basin floor topography

of the Woodford Sea. The Woodford Shale was deposited as the sea progressively transgressed onto the unconformity surface and depressions on the sea-floor were inundated earlier compared to topographically high areas. We were able to map the seabed topography (Figure 40) of the Woodford Sea or the top surface of the Hunton Limestone. Seabed topography (Figure 40) in combination with the time-thickness map of the Woodford Shale (Figure 37) indicates the relatively thick accumulation of the Woodford Shale in depression areas of the basin and thinner Woodford interval in topographically high areas.

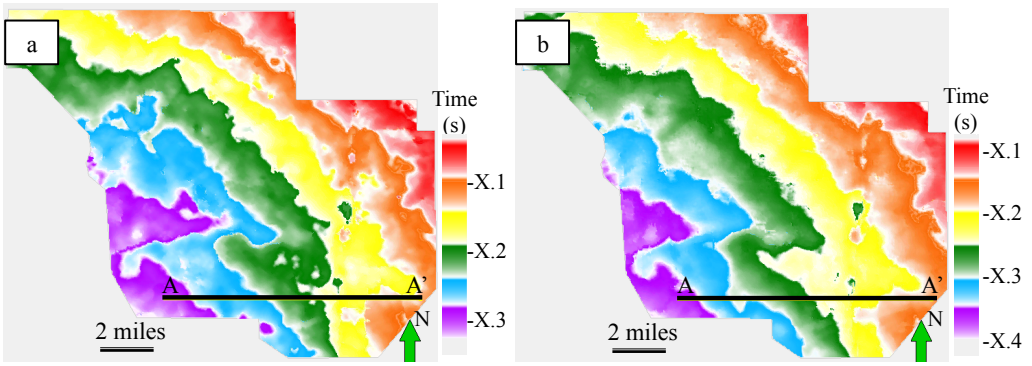

Figure 36: Time structure map of the (a) base of the Woodford Shale/top of the Hunton limestone, and (b) top of the Woodford Shale. Vertical slices along line AA' are shown in the following figures.

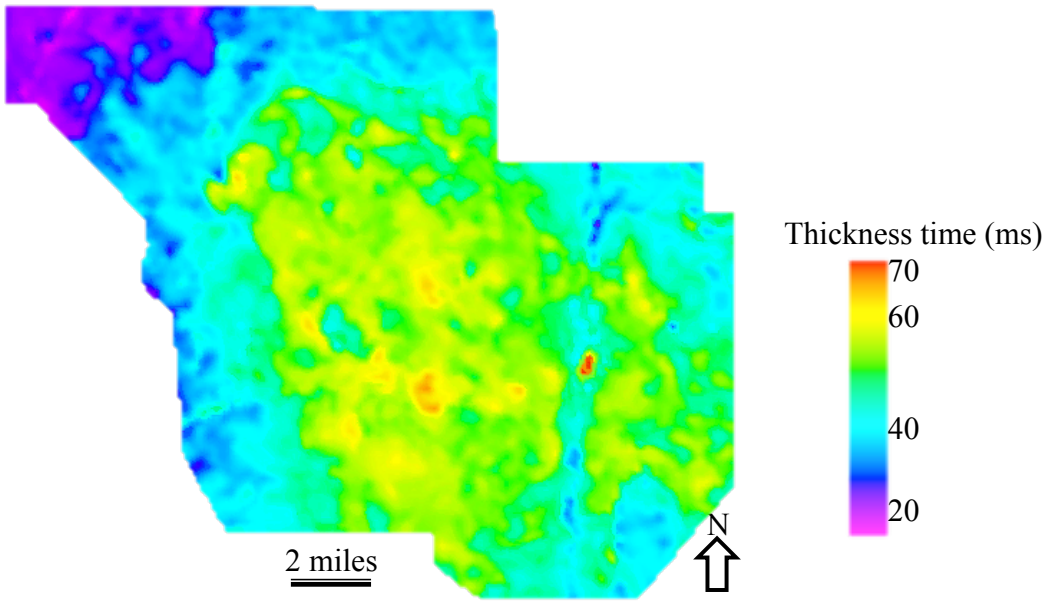

Figure 37: Time thickness map of the Woodford Shale showing apparently anomalous distribution of the Woodford Shale and no correlation with the time structure maps.

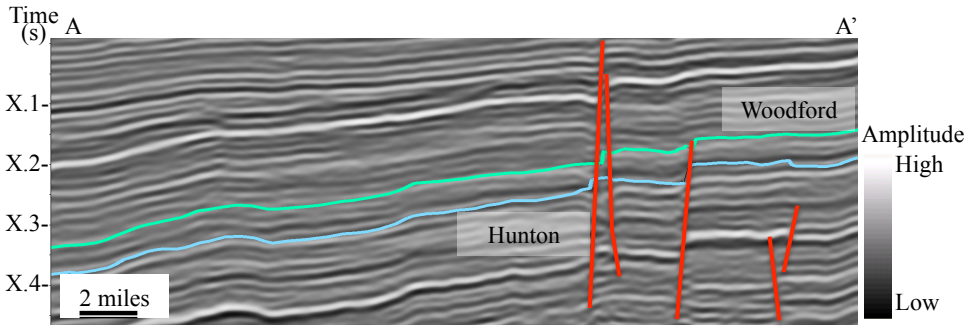

Figure 38: Vertical slice along AA' through the seismic amplitude volume showing the Woodford Shale and the underlying Hunton limestone. Some of the faults cutting through these two horizons are marked with red lines.

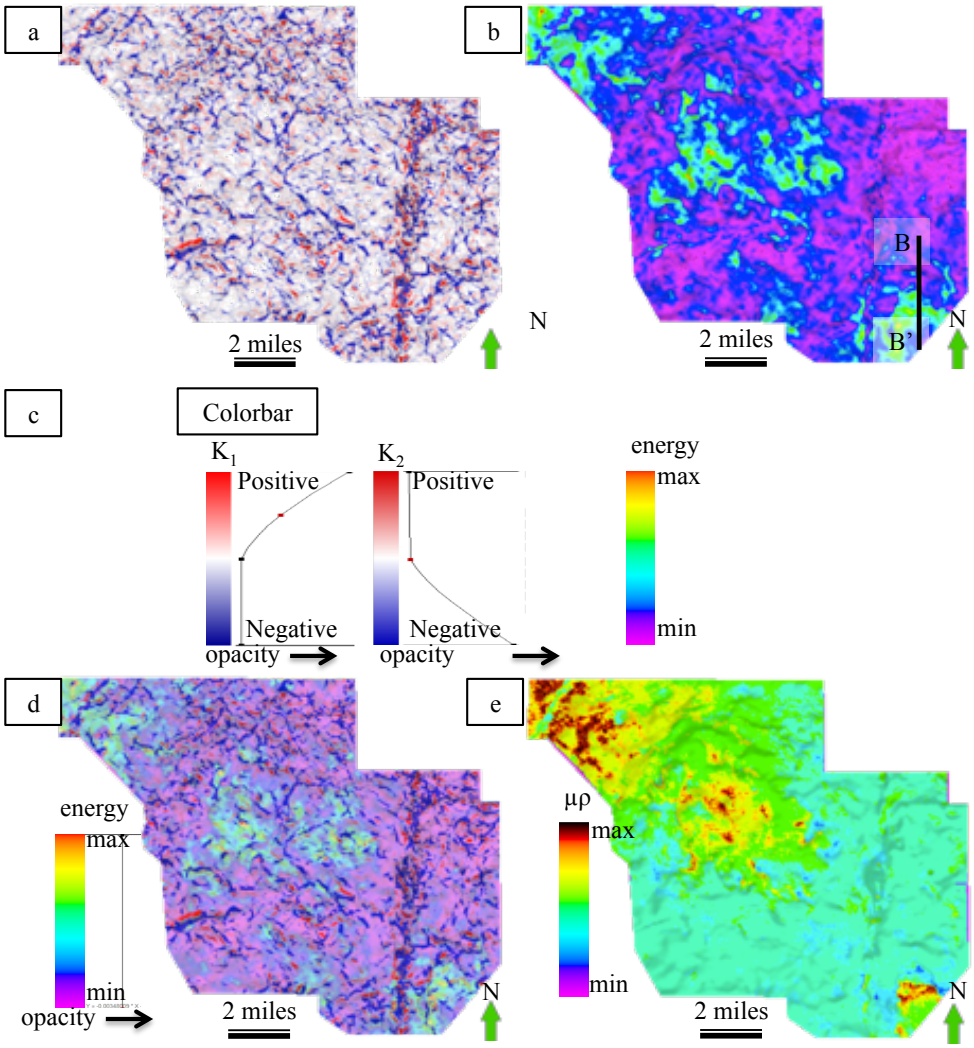

Figure 39: Horizon slices through the attributes calculated from a seismic volume flattened along the top of the Woodford Shale and along the top of the Hunton Limestone reflecting the geomorphologic features of the basin floor of the Woodford Sea. (a) Horizon slice through the co-rendered most positive (K_1) and most negative (K_2) principal curvature attribute volumes. (b) Horizon slice through the coherent seismic energy attribute volume. Vertical slices along BB' is shown in Figure 6. (c) Colorbars used in Figures a, b. (d) Horizon slice through the co-rendered most positive (K_1) and most negative (K_2) principal curvatures, and coherent seismic energy attribute volumes. The coherent seismic energy attribute volume is rendered transparent (~50%) in this Figure. (e) Horizon slice through the μρ attribute volume. Note the areas with high μρ values match with higher values for the coherent seismic energy shown in Figure b.

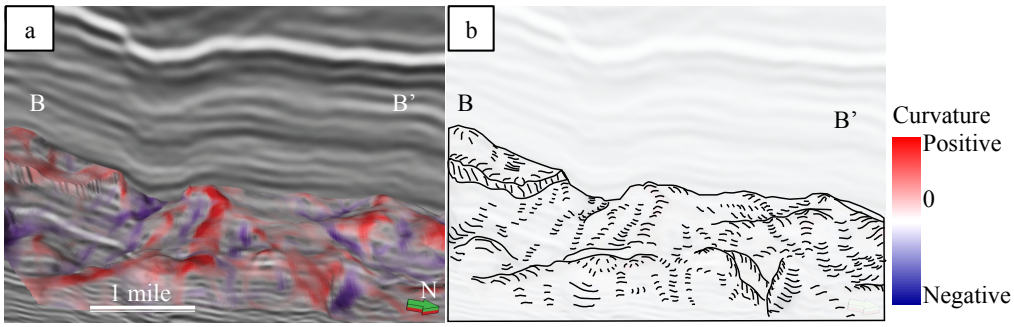

Figure 40: (a) 3D display of a horizon slice through most positive and most negative principal curvatures with a vertical slice through seismic amplitude. (b) Schematic diagram drawn from the curvature expression of the horizon in Figure a showing the rugged sea-bed topography of the Woodford Sea as defined by the unconformity surface on top of the Hunton Limestone.

Stratigraphic framework

When calibrated with wells, seismic attributes enable the mapping of subtle but important stratigraphic components, which in turn facilitate the construction of the depositional history. To this end, we examined 20 Woodford stratal slices through co-rendered coherent seismic energy and in-line energy gradient, and μρ attribute volumes in order to track stratigraphic changes in the study area, five of which are shown in Figure 41, Figure 42. Low energy areas (magenta and blue colored areas) in Figure 41a represent the initial shale (low seismic energy) deposition on top of the Hunton Limestone (high seismic energy). High seismic energy areas on this figure correspond to structural highs (Figure 41b) on the sea floor, which are more amenable to receive only suspension fallouts. In contrast, structural lows on the sea floor were inundated earlier, are affected by storm and turbidity currents, as well as debris flows resulting in silty deposits rather than clay-rich suspension fallouts. Note shale deposition didn't start in the high seismic-

energy area in the top left corner of Figure 41a and Figure 41b (areas marked with black circle) until the time of Middle Woodford deposition started (Figure 41c). The outlined areas (Figure 41b, Figure 41d, and Figure 41e) are high seismic-energy areas within the Woodford Shale, probably indicating silica enrichment. Notice, the white outlined area (high energy) in the northeastern part of Figure 41d, and Figure 41e corresponds to shale deposits reflecting low seismic energy in Figure 41a, Figure 41b, and Figure 41c. This high seismic-energy area is representing increase in chert in the Upper Woodford, as reported in the literature (Chapter 4 of this dissertation). Stratal slices extracted from the $\mu\rho$ attribute volume further confirm the similar depositional pattern (Figure 42). Low $\mu\rho$ values indicate clay-rich shale and high $\mu\rho$ values indicate lithologies like limestone, silica-rich rocks.

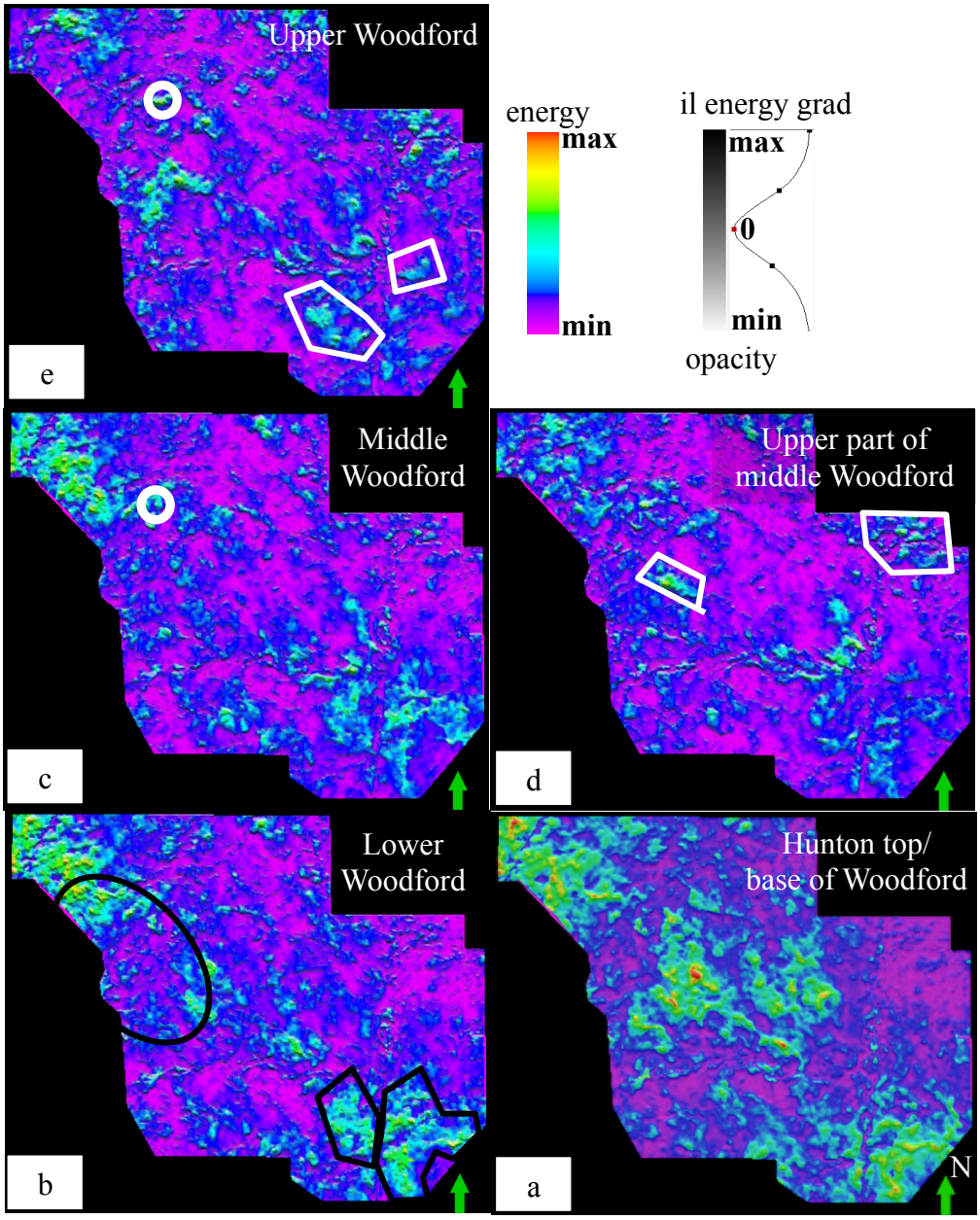

Figure 41: Stratal slices generated by co-rendering coherent energy with in-line energy gradient. Figures from bottom to top represent top of the Hunton unconformity, in the middle of the Woodford Formation and near the top of the Woodford Formation respectively (a, b, c). Notice the subtle high seismic-energy nature (represented by cyan color) in the top-most stratal slice. (c) may be indicative of richness in biogenic silica concentration as reported in the literature (Chapter 4 of this dissertation).

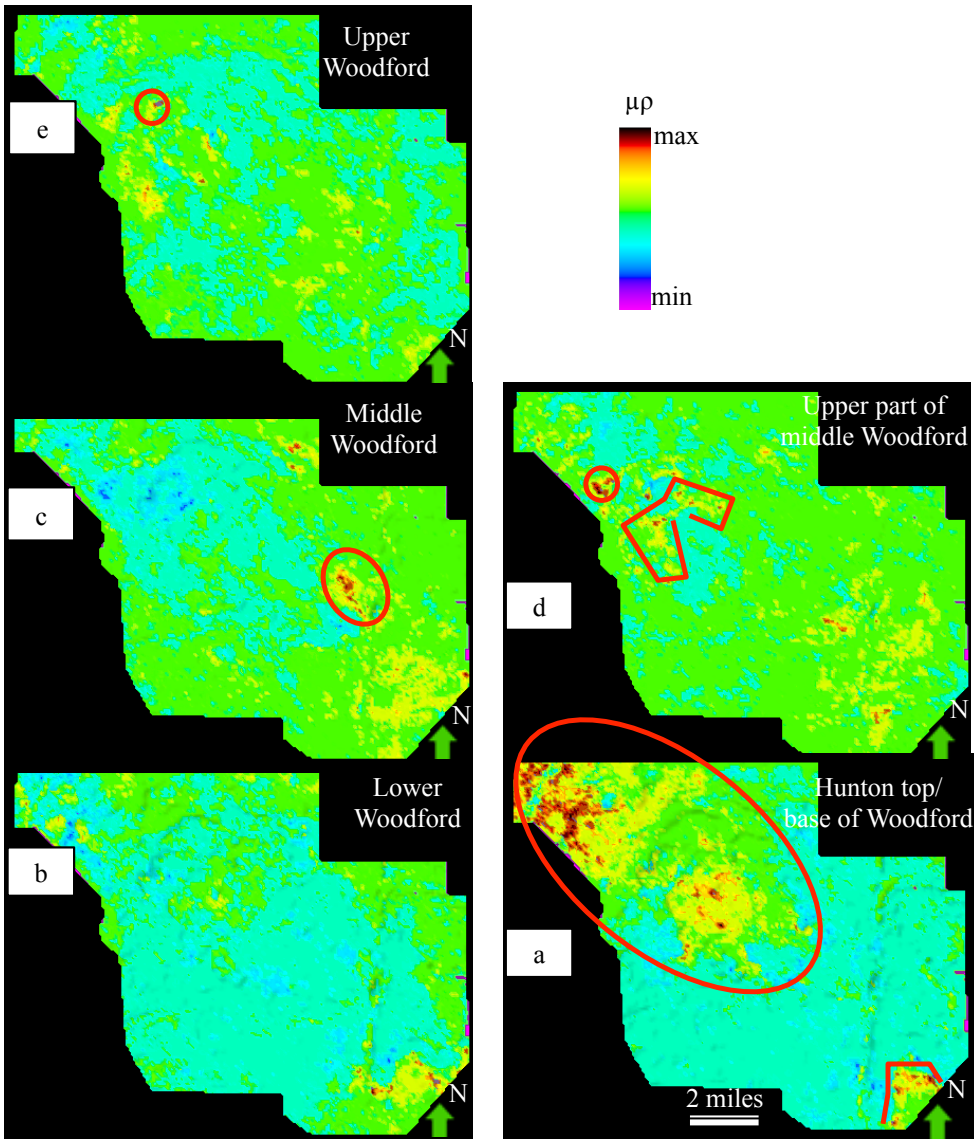

Figure 42: Stratal slices generated from the μρ attribute volume. Figures from bottom to top represent top of the Hunton unconformity, in the middle of the Woodford Formation and near the top of the Woodford Formation respectively (a, b, c). (c) Biogenic silica enrichment (marked by red ellipse) as reported in the literature (Chapter 4 of this dissertation).

Natural fracture distributions

Natural fracture plays critical role for the evaluation of the tight, low-permeable resource-shales in a number of ways, such that open fractures improve the host rock's permeability while mineral filled fractures provide week areas in rock to inititate artificial fractures. Figure 3 indicates that the Woodford Shale and the underlying Hunton Limestone are affected by multi-stage post-Woodford tectonic deformations enhancing the generation of natural fractures. Figure 43 shows that the Woodford Shale is naturally fractured in the study area. Structural deformation and the tectonic history indicate that major and multi-stage tectonic activities affected the Woodford Shale in the study area. We have used a number of conventional and recently developed volumetric attributes to highlight possible areas of natural fracture concentration. Volumetric seismic attributes are routinely used to map drilling hazards in shale plays (Sullivan et al., 2006; Schulke, 2011). Conventional attributes detect major structural deformation; recently developed attributes illuminate subtle changes in structural elements and thus capture the complex nature of these structural elements and are also good for detecting subtle geomorphologic features. We have used seismic attributes to highlight a number of faults, collapse features and fracture zones within the Woodford Shale and the underlying Hunton Limestone critical for the hydrocarbon exploration within the Woodford Shale.

Figure 44 shows an example of a horizon slice through Sobel filter similarity, an edge-detecting attribute highlighting the faults and the irregular unconformity surface at the base of the Woodford Shale (which is also the top of the underlying Hunton Limestone). Collapse features in the Hunton Limestone highlighted by the Sobel filter similarity (Figure 44) form low areas (Figure 40) on the Woodford Sea characterized by

high curvature values (Figure 39) and likely to contain lots of natural fractures. Such areas also contain thicker (Figure 37) Woodford Shale succession.

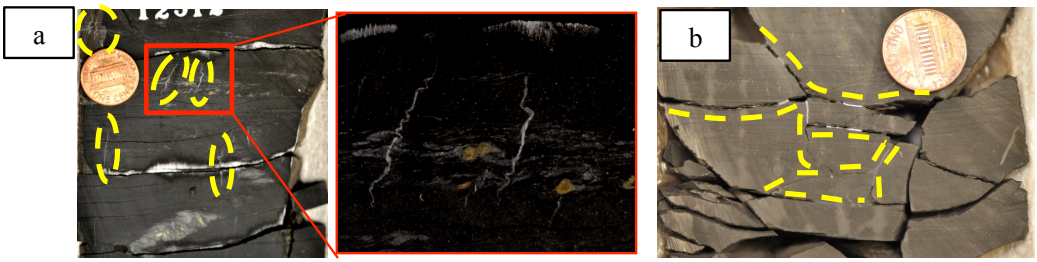

Figure 43: Photograph of subsurface core collected from one of the subsurface wells in the study area. (a) Natural fractures, and (b) either drilling induced fractures or natural fractures got enhanced by drilling activities.

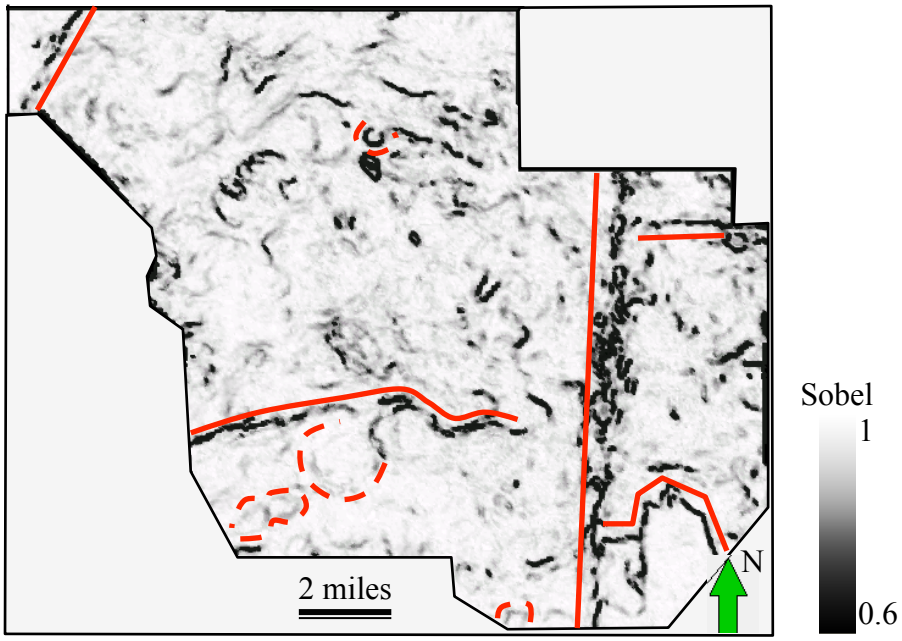

Figure 44: Horizon slice through the Sobel filter similarity attribute volume along the underlying Hunton Limestone over which the Woodford Shale was deposited. Solid red lines indicate faults while the dashed red lines indicate some of the collapse feature.

One of such recently developed attribute, strike of the most-negative principal curvature, $\psi_{k2,}$ modulated by the magnitude of the most negative principal curvature, k_2, (Al-Dossary and Marfurt, 2006) show the progressive change in fault azimuth from NE-SW to NW-SE across the survey within the Woodford Shale interval (Figure 45). Not only the fault orientation we have also tracked the relative movements of the fault blocks with respect to each other through another recently developed attribute reflector rotation with respect to reflector normal (Figure 46). This attribute determines the rotation about the normal to the reflector dip and thus is a measure of the reflector rotation across a discontinuity. Marfurt and Rich (2010) discuss the mathematical background for the calculation of this attribute.

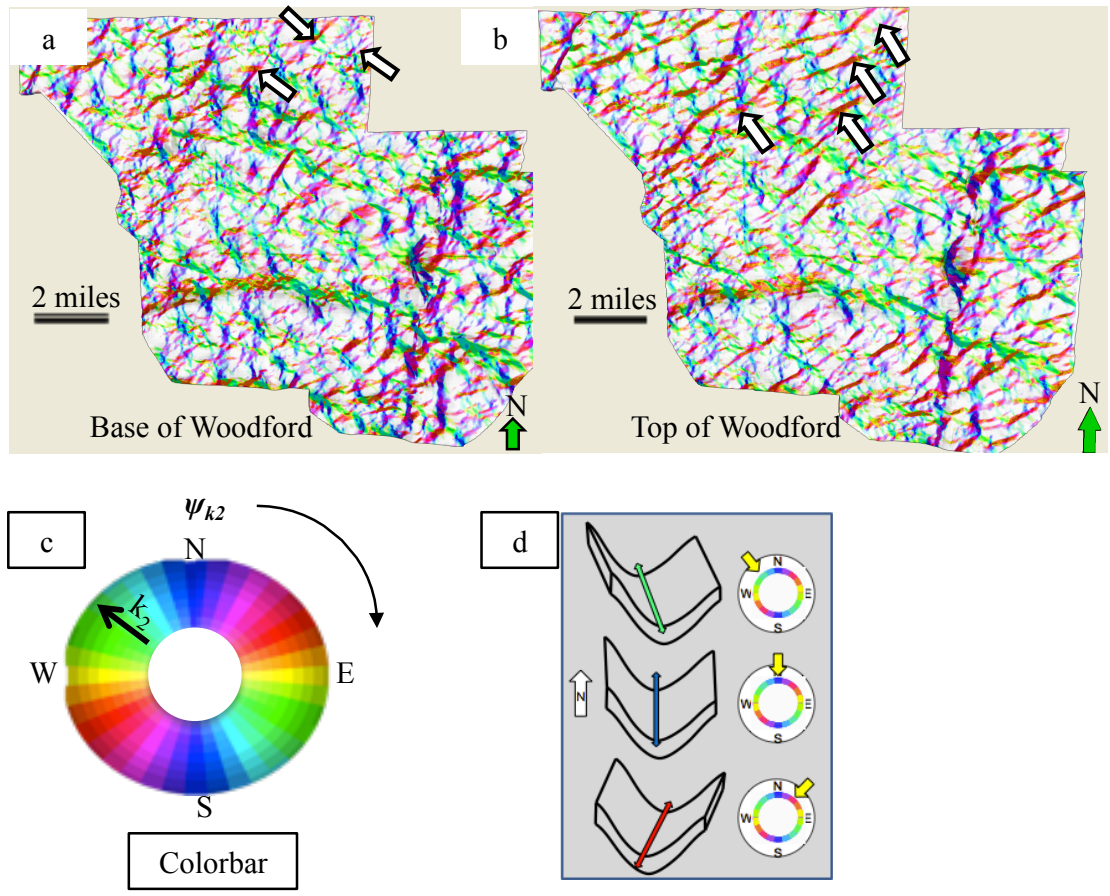

Figure 45: Horizon slice through the strike of the most-negative principal curvature, ψ_{k2}, (plotted against hue) modulated by the magnitude of the most negative principal curvature, k_2. (a) 10 ms above the Hunton top and (b) near the Woodford top using (c) a 2D colorbar and making the low curvature values transparent. (d) Cartoon illustrating a valley trending NW-SE colored cyan (top), a valley trending NS colored blue (middle), and a valley trending NE-SW colored magenta (bottom). Note the change in the orientation (indicated by white arrows) of the lineaments in the Woodford compared to the Hunton, indicated by white arrows.

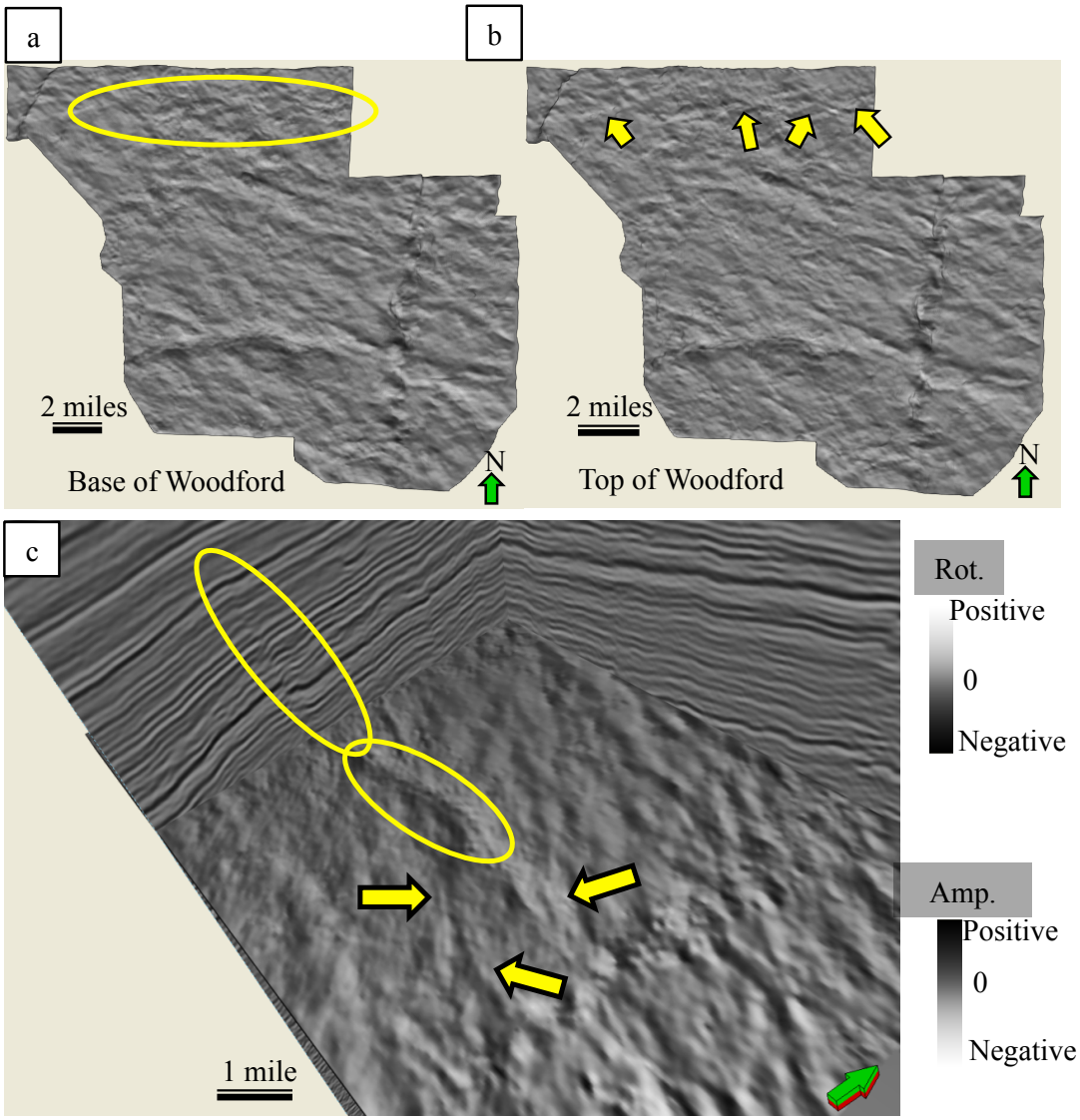

Figure 46: Reflector rotation about the average reflector normal. The horst and graben blocks show considerable contrast and can be interpreted as separate units. (a) Horizon slice at t = 10 ms above the top of the Hunton Limestone, and (b) horizon slice near the top of the Woodford Shale. Ellipse and arrows on Figures a and b indicate progressive changes in the fault block rotation from the base to the top of the Woodford Shale. (c) Chair display of a time slice through reflector rotation about the average reflector normal and vertical profiles through seismic amplitude. Yellow ellipses show the same fault seen on the vertical slice through the seismic amplitude volume and on the time slice. Yellow arrows indicate a number of fault branches connected to a parent fault block.

The curvature attribute highlights areas with high flexures, which are potential areas for strain concentration and development of natural fractures. Previous authors have also documented correlation between natural fractures and curvature obtained from various sources. Murray (1968) correlated natural fractures and improved production from the Bakken formation of North Dakota with curvature obtained from well tops and 2D seismic correlated. Roberts (2001) first applied the curvatures to surfaces interpreted from 3D seismic data. There are two sets of curvature attributes such as: the most positive and most negative principal curvatures and the more commonly used most positive and negative curvatures, k_{pos} and k_{neg}. There is a significant difference between theses two sets of attributes (Marfurt, 2010). The principal curvatures exhibit anomalies along the tightest synclinal and anticlinal components of a fold, independent of the fold orientation while the k_{pos} and k_{neg} exhibit anomalies along the crest and trough of a fold with respect to the vertical time or depth axis. We have used the most positive and most negative principal curvatures to highlight potential areas for higher number of natural fractures. Guo et al. (2010) correlated natural fractures and the curvature attribute in the Woodford Shale. Multi attribute analyses through co-rendering of geometrically independent and interpretationally complementary attributes fine-tune the potential areas with natural fractures. Co-rendered Sobel filter similarity and most positive and most negative principal curvatures highlight the potential natural fractures (Figure 47). Sobel filter similarity is an edge-detecting attribute and highlights any discontinuity (Faults, fractures, joints etc.) within a reflector and the curvatures highlight areas with high flexures as stated before. Horizon slice through another recently developed attribute co-rendered most positive curvature on amplitude and most negative curvatures on

amplitude (Figure 48) shows similar geomorphologic characteristics as the previous one but appear as much high resolution. Such similarity indicates that this attribute can also be used to highlight fracture or damage zones within a horizon.

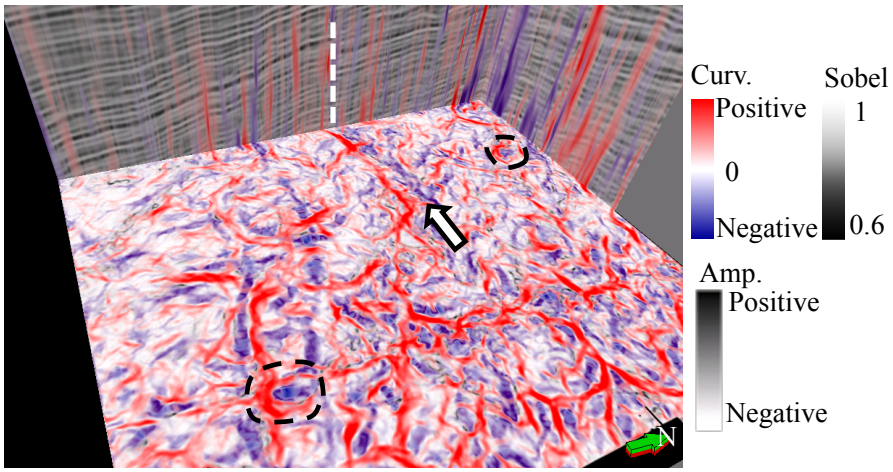

Figure 47: Chair display of a time slice showing co-rendered seismic amplitude, Sobel filter similarity, most-positive curvature, and most-negative curvature. Areas with low coherence match with the most-negative principal curvatures (areas marked by blue). Fault indicated by the white-dashed line on the vertical slice is aligned with a flexure bracketed by strong K_1 and K_2 values next to each other (marked by white arrow). Also note the red ridges of the most-positive principal curvature with the structure seen on the vertical slices through the seismic amplitude volume. Two of the collapsed features are highlighted by black dashed lines on the time slice.

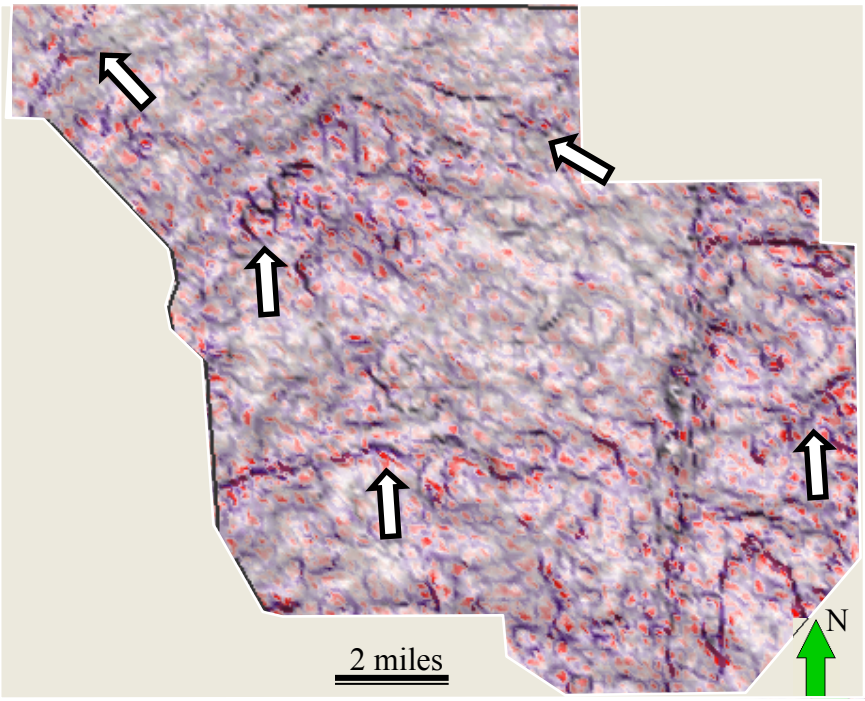

Figure 48: Co-rendered horizon slice along the top of Hunton through most-positive principal curvature, amplitude, most-negative principal curvatures. Areas with strong curvature have undergone considerable strain and thus are more likely to be fractured (white arrows).

Rigorous analyses of curvature of a reflector at different places allow us to quantitatively define the shape of reflector. Marfurt (2010) provides the mathematical expressions to calculate these shapes through shape index modulated by curvedness. The curvedness, C, quantifies the degree of deformation such that a planar surface has C=0.0, and large values of C define highly deformed surfaces. The shape index, s, is defined by the inter relationship between the most positive (K_1) and most negative (K_2) principal curvatures and progress from a bowl (s=-1.0, $k_1 \geq k_2$), through a valley (s=- 0.5), saddle (s=0.0), ridge (s=+0.5), to a dome (s=+1.0), with all the values in between (Figure 49).

Co-rendered image of shape index modulated by curvedness and seismic amplitude delineates the similarity between reflector shape and the calculated shapes of reflectors (Figure 50). Bowl-shape collapse features are possibly associated with the collapse of Hunton Limestone appear blue (blue arrow) and areas of thicker accumulation of the Woodford Shale. Guo et al. (2010) also used the shape index modulated by curvedness to illuminate surface irregularity of the Woodford Shale. Microseismic data indicates that the ridges and domes are favorable areas for initiating hydraulic fracturing (Figure 51).

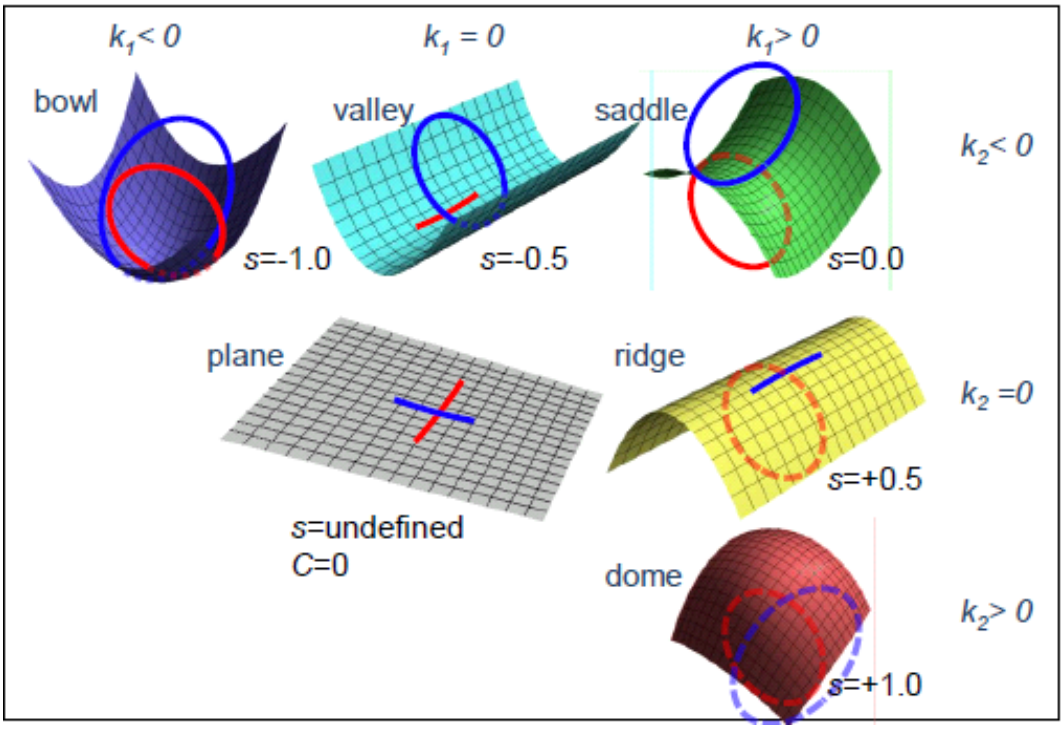

Figure 49: The definition of 3D quadratic shapes expressed as a function of the most-positive and most-negative principal curvatures, k_1 and k_2, through the shape index, $s=-(2/\pi)ATAN[(k_2+k_1)/(k_2-k_1)]$. By definition, $k_1 \geq k_2$. The curvedness, $C= [k_1^2+ k_2^2]1/2$. For values of $k_1=k_2=0$, the curvedness, $C=0$, the shape index, s, is undefined and we have a plane. If the shape index, $s=-1.0$, we have a bowl, if $s = -0.5$, we have a syncline, if $s = 0.0$, we have a saddle, if $s = +0.5$, we have an anticline, and if $s = +1.0$, we have a dome. (Figure modified from Marfurt, 2010).

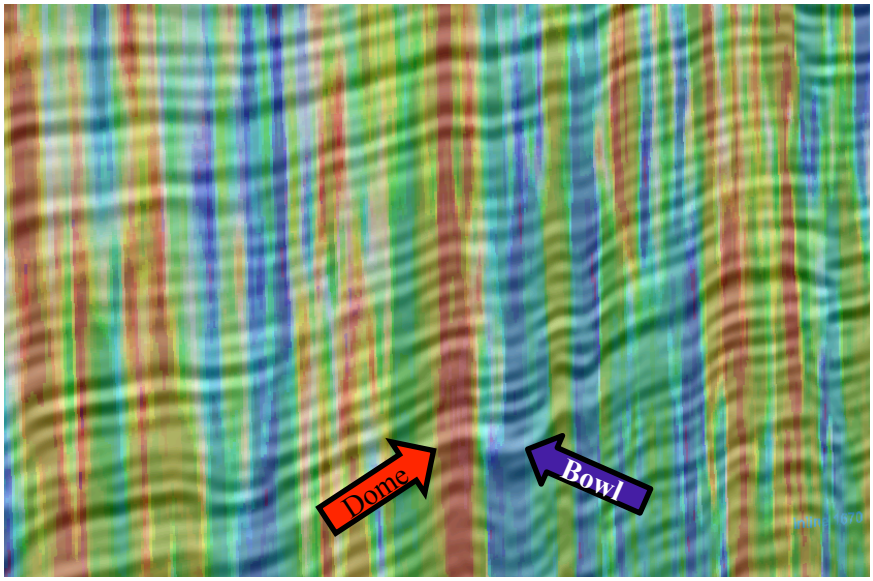

Figure 50: Shape index modulated by curvedness co-rendered with seismic amplitude. Red (dome) and blue (bowl) indicate irregularities associated with the unconformity surface. Note the correlation of the reflector shape attribute with the structure seen on the vertical slices through the seismic amplitude.

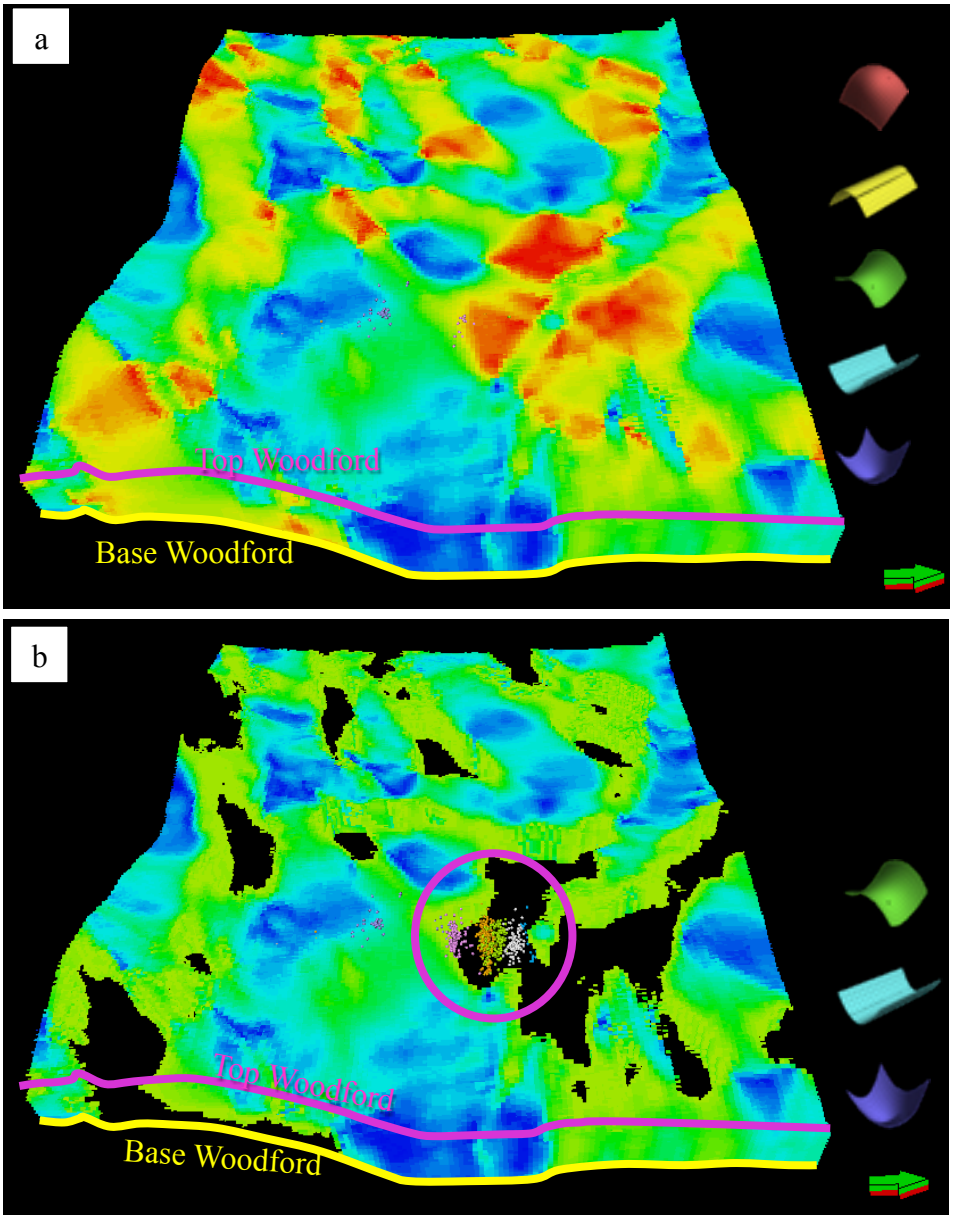

Figure 51: (a, b) Co-rendered horizon slice through the shape index modulated by curvedness and microseismic events. (b) Microseismic events are visible when the dome and ridges are rendered transparent indicating favorable areas for artificial fracturing in those areas and are also possible areas for higher number of natural fractures. Figure is modified from Guo et al., 2010; Microseismic courtesy of Pablo LLC; Seismic data courtesy of CGG-Veritas.

Petrophysical analysis

Petrophysical properties from core data allow us to define rock types, reservoir intervals and mechanical properties. Rock types in core are then correlated with well logs and finally to seismic impedance inversion resulting in 3D rock type volumes. Figure 52a shows three rock types identified from the core measurements, Figure 52b shows the same rock types, Figure 52c shows the data from seismic inversion. Core measurements shows that total organic carbon (TOC)-rich rocks are ductile and TOC-lean rocks are brittle (Figure 52a). Hence, intervals with alternating TOC-rich ductile rocks and TOC-lean brittle rocks are sweet spots within the Woodford interval containing good amount of hydrocarbon and having the brittle contrast needed to initiate hydraulic fracturing. Integrated 3D reservoir descriptions and 3D mechanical properties illuminate the reservoir-brittle rock couplet representing the sweet spots for the unconventional Woodford Shale.

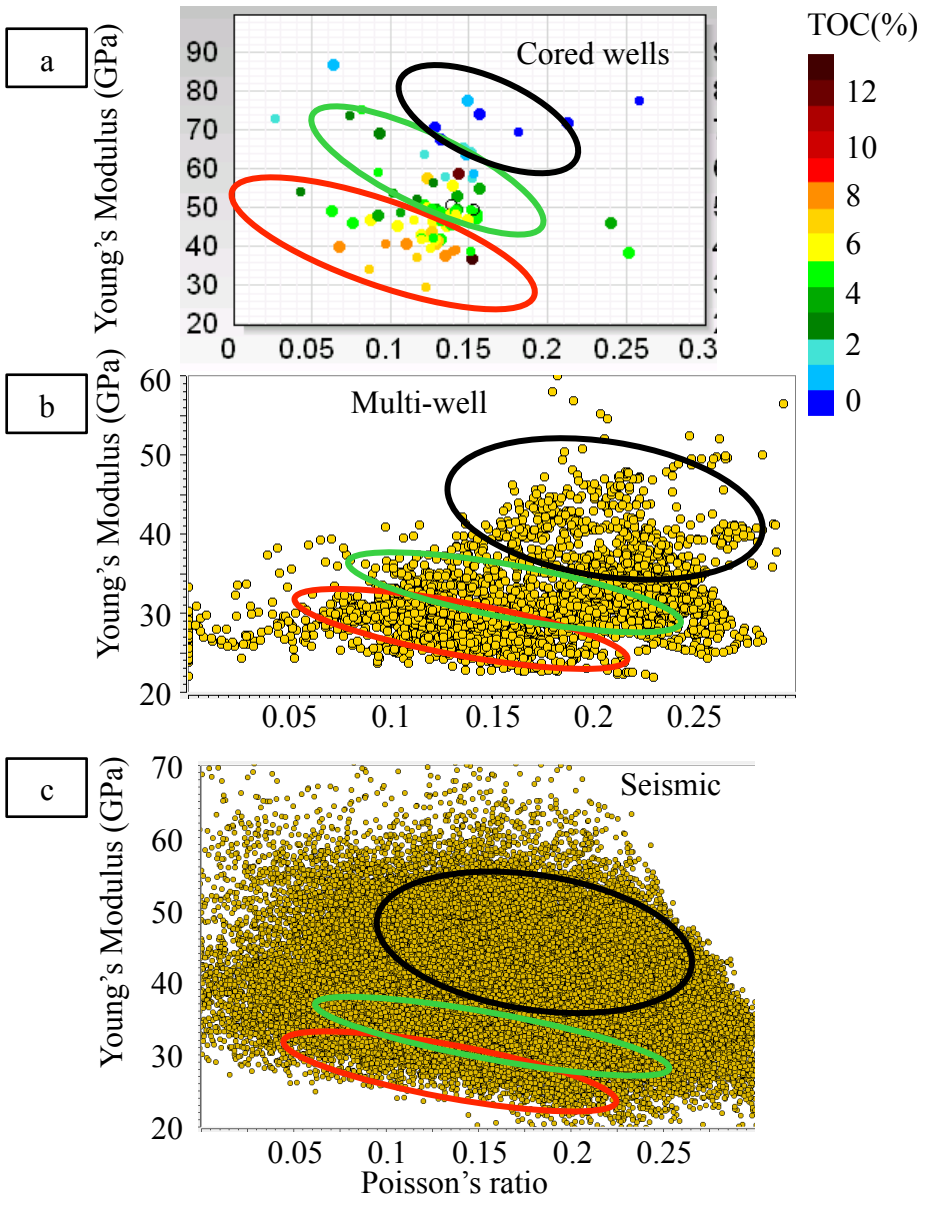

Figure 52: Crossplots of Young's modulus (E) and Poisson's ratio (v), (a) from core measurements, (b) from logs in 12 wells, (c) prestack seismic inversion. Crossplots indicate comparatively narrow range of v and wider range for the E. (a) Three rock types identified from core measurements. Data values are color coded by total organic carbon (TOC). Note the TOC-rich rocks (red ellipse) have lowest range of Young's modulus and hence, are ductile in nature compared to more brittle TOC-lean rocks (black ellipse). Rock types from core data are transferred to well data and seismic data crossplots.

Conclusions

Seismic data is the only source to track 3-dimensional distributions of hydrocarbon reservoirs even for the highly heterogeneous resource-shales.

Seismic attribute analyses help to illuminate both structural and stratigraphic elements, which are critical to understand the physiogeographic setting of the basin. Conventional seismic attributes illuminate major geomorphologic features while recently developed volumetric seismic attributes illuminate subtle changes in structural and stratigraphic changes critical for the hydrocarbon exploration within the shales.

Sequential seismic geomorphologic analyses with the help of various seismic attributes help us to determine periodic changes in depositional sequence stratigraphic pattern within the Woodford interval. Such analyses also help to identify potential areas for hydrocarbon exploration.

Detailed calibration of seismic geomorphology with the petrophysical properties along with acoustic impedance inversion guide us to redefine the estimates of depositional packages in yet to explore areas. Rock properties extracted from the calibrated seismic data also help to recognize different petro-types at regional scale.

In this study, we have proposed a workflow for the regional characterization of the Woodford Shale, which can also be applied for the resource evaluation of any other resource shales.

References

Al-Dossary, S., and K. J. Marfurt, 2006, Multispectral estimates of reflector curvature and rotation: Geophysics, 71, P41-P51.

Chopra, S. and K. J. Marfurt, 2010, Interpreting fractures through 3-d seismic discontinuity attributes and their visualization: AAPG international convention and exhibition.

Energy Information Administration, 2011, Review of Emerging Resources: U.S. Shale Gas and Shale Oil Plays, ftp://ftp.eia.doe.gov/natgas/usshaleplays.pdf.

Guo, H., S. Lewis, and K. J. Marfurt, 2008, Mapping multiple attributes to three- and four-component color models – a tutorial: Geophysics, 73, W7-W19.

Guo, Y., Zhang, K., and Marfurt, K.J., 2010, Seismic Attribute Illumination of Woodford Shale Faults and Fractures, Arkoma Basin, Ok. *SEG Technical Program Expanded Abstracts* 29, 1372-76.

Marfurt, K. J., 2010, The shape of seismic interpretation: AASPI consortium meeting, Norman, Oklahoma.

Marfurt, K. J. and J. Rich, 2010, Beyond curvature – volumetric estimates of reflector rotation and convergence, 80th Annual International Meeting, SEG, Expanded Abstracts, 1467-1472.

Murray, G.H. Jr., 1968, Quantitative Fracture Study-Sanish Pool, McKenzie County, North Dakota: AAPG Bulletin, 52, 57-65.

Roberts, A., 2001, Curvature attributes and their application to 3D interpreted horizons. First Break, 19, 85-99.

Chapter 4

Lithostratigraphic characterization and depositional setting of the Woodford Shale in west-central Oklahoma

Abstract

Limited understanding about the depositional processes adds uncertainty and therefore increases risk in the exploration activities in the emerging Woodford Shale play. To address this issue, this paper presents an integrated study of a set of laboratory measured and field data from both hydrocarbon producing and non-producing wells in the Anadarko Basin. The 200ft thick Woodford Shale cores can be subdivided into the lower, middle and upper members with average thicknesses 58ft, 77ft and 62 respectively. Cores were subjected to visual core description, petrographic analyses, laboratory measured petrophysical properties (bulk density, grain density, porosity, mineralogy, total organic carbon [TOC], rock eval pyrolysis, acoustic velocities [V_p-fast, V_s-fast and V_s-slow], core gamma ray), scanning electron microscopic analyses (SEM), and then correlated to wireline logs. Careful integration of data from multiple sources have revealed 14 depositional cycles within the Woodford interval with the three individual members made up of 6, 4, and 4 cycles from base to top. All the major flooding events correlate with published eustatic sea-level curve curves. Such events are typically characterized by hot gamma ray traceable in wells from widely separated geographic areas and thus are indicative of global events. These preliminary findings

provide components of a database that can be used to prioritize drilling prospects from surface seismic and production data.

Introduction

The late Devonian to early Mississippian Woodford Shale is an active shale-resource play. Although this shale formation has long been considered as the primary source rock for most of Oklahoma's hydrocarbon reserves, the depositional history and its correlation to reservoir petrophysical properties has not been established. A number of studies based on outcrop, laboratory and field data have shown the Woodford Shale to have a complex lithofacies distribution associated with variable amounts of TOC (Cardott and Lambert, 1982; Comer, 2008b; Comer, 1992; Fertl and Chilingarian, 1990; Hester and Schmoker, 1983; Hester et al., 1990; Kvale and Coffey, 2010; Lambert, 1993; Paxton et al., 2006; Sullivan, 2006). Comer (1992) lists the areas having greatest gas production potential and most prospective lithologies within the Woodford Formation to be the Anadarko Basin in Oklahoma (siltstone and silty-black shale), Arkoma Basin in Oklahoma and Arkansas (silty black shale), the Frontal zone of Ouachita fold belt in Oklahoma (chert), the Delaware Basin in Texas and New Mexico (siltstone and silty black shale), and the Val Verde and Midland Basins in Texas (siltstone and silty black shale). Major areas of thick Woodford accumulations include basins as well as uplifted areas in Oklahoma, Arkansas, Texas and New Mexico. Figure 53 shows the estimated resource potential of the Woodford Shale in Oklahoma (Comer, 2008b). Cardott and Lambert (1982) report that the depth of the Woodford Shale in the Anadarko Basin ranges from 5,060 ft on the northeastern shelf to 25,115 ft in the deepest part of the basin**;** thicknesses range from less than 25 ft in the northern shelf areas to more than 900 ft

along the frontal Wichita fault zone. Vitrinite reflectance increases systematically with depth.

Current study area focuses in west-central Oklahoma (Figure 54) where the Woodford Shale is about 200 ft. In this paper, I will use state of the art geologic history at the finest level, which can further be used to track the basin-wide correlations and changes. I start with petrographic observations, sedimentary and post-sedimentary structures, grain size distributions, and porosity. Next, I establish correlations between the petrophysical properties with the petrographic observations thereby defining principal petrophysical proxies for identifying syn- and post-depositional changes in the geologic processes. Then I correlate the cored wells to other wells in order to identify large-scale changes associated with the global sea-level curve.

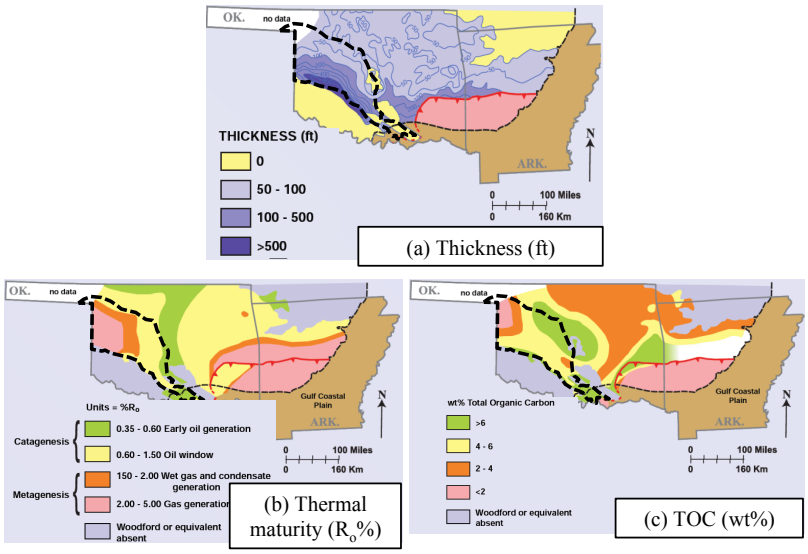

Figure 53: Map showing distribution of (a) thickness, (b) thermal maturity, (c) TOC (wt%) of the Woodford and equivalent strata. Inscribed black dashed line is showing the outline of the Anadarko Basin (approximate). Modified from Comer (2008).

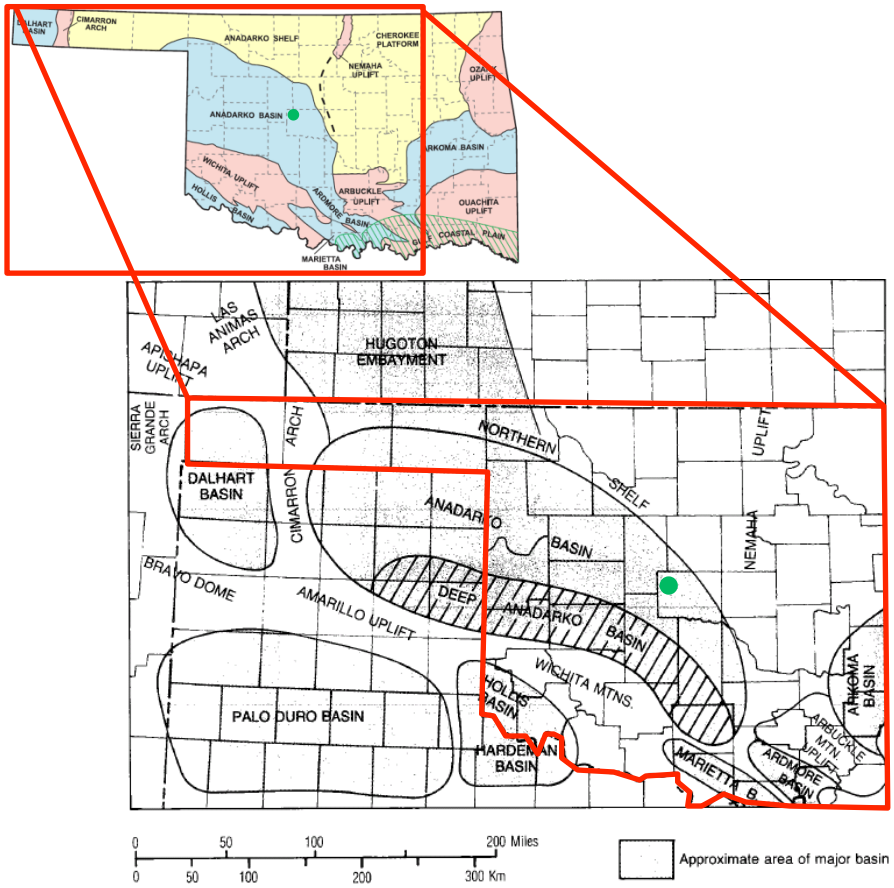

Figure 54: Major geologic provinces of Oklahoma. The enlarged map is showing Anadarko basin and surrounding geologic provinces; outlined area in red marks a part of Oklahoma present in the enlarged figure. Green dot is the approximate location of the studied cored-well. Figures are modified from Johnson (2008,1988).

Geologic framework

The late Devonian-early Mississippian Woodford Shale was deposited in an epeiric sea covering the huge Oklahoma basin extending over most parts of the southern Midcontinent (Figure 55) with the Anadarko basin being one of the protobasins of this ancestral Oklahoma basin. The Anadarko basin was formed as the Oklahoma basin was broken into a series of sharp uplifts and major basins during a post-Woodford,

Pennsylvanian orogenic episode. The present day geographic boundary of the Anadarko basin is defined by the Wichita and Amarillo uplifts on the south, the Nemha uplift on the east, the Cimarron arch on the west. The northern end extends across much of western Kansas, part of which is denoted as the Hugoton embayment (Figure 54). The Anadarko Basin is the deepest sedimentary and structural basin in the cratonic interior of the United States. The deep Anadarko basin and the Wichita-Amarillo uplift is known as the southern Oklahoma aulacogen which was also the deepest part of the Oklahoma basin (Johnson, 1988). Figure 56 shows the generalized stratigraphy of southern Oklahoma. The Woodford Shale was deposited as the sea progressed from south-southeast to northwest during a global sea-level rise. The base of the Woodford Formation has been correlated with the Taghanic onlap (Paxton et al., 2006), formed in response to the Kaskaskia transgression (Sloss, 1963). A widespread regional unconformity (period of non-deposition and erosion) defines the base of the Woodford Shale that in most places rests on the Silurian Hunton Limestone. Paleogeographic reconstruction indicates that during late Devonian time North America (Laurentia) moved north which placed the southern midcontinent near 15° to 20° south latitude (Figure 57). Such latitudes are associated with frequent ocean upwelling and a temperate climate, both of which aided the high biologic production and resulting TOC enrichment seen in the Woodford Shale.

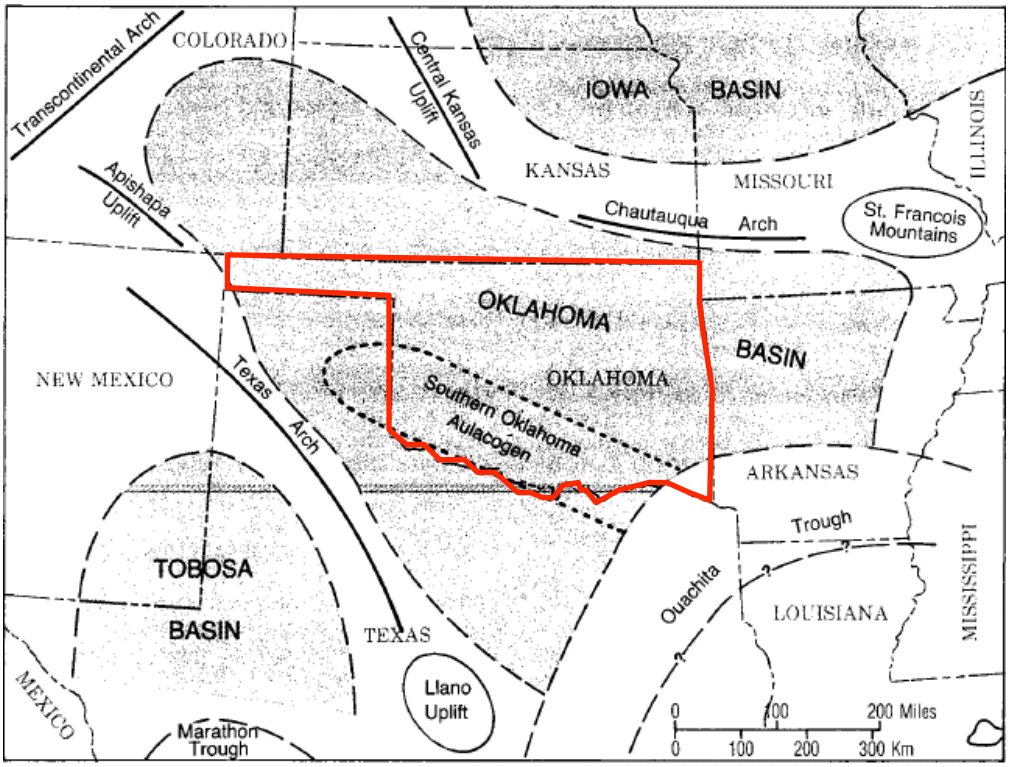

Figure 55: Approximate boundary of the Oklahoma basin and other major features in the early and middle Paleozoic time. Oklahoma-state is marked with red line. Figure is modified from Johnson (1988).

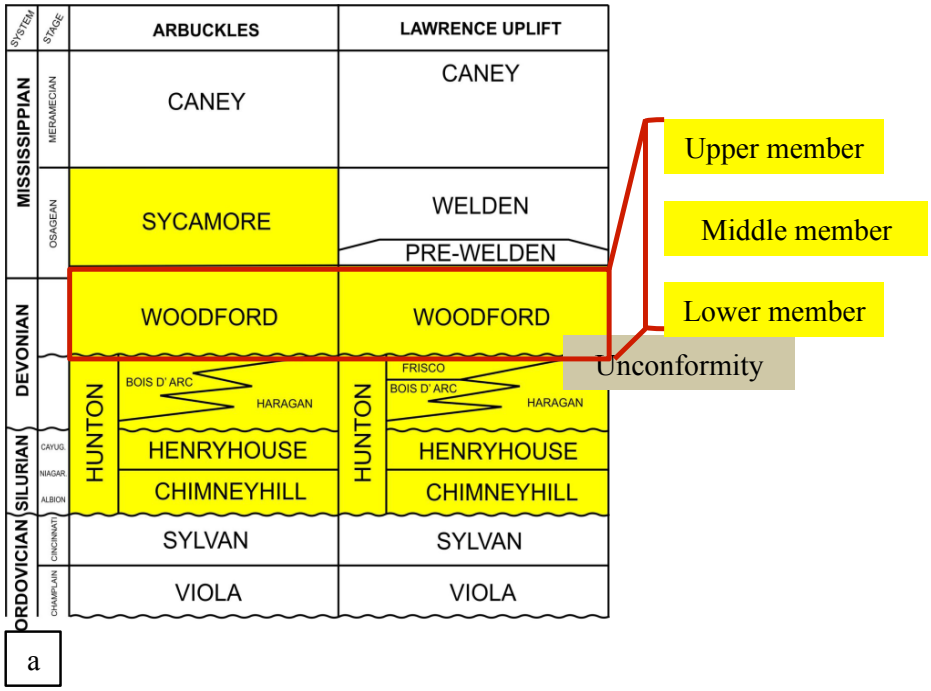

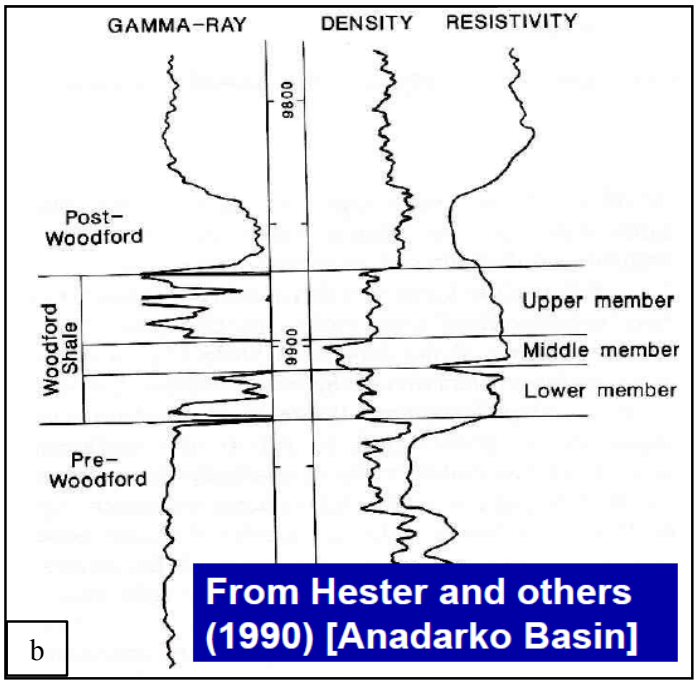

Figure 56: (a) Stratigraphy of the Woodford Shale, (b) type logs for the Woodford Shale. The informal members are defined on the basis of palynomorph, geochemistry and log signatures. Figures are modified from Cardott, 2008.

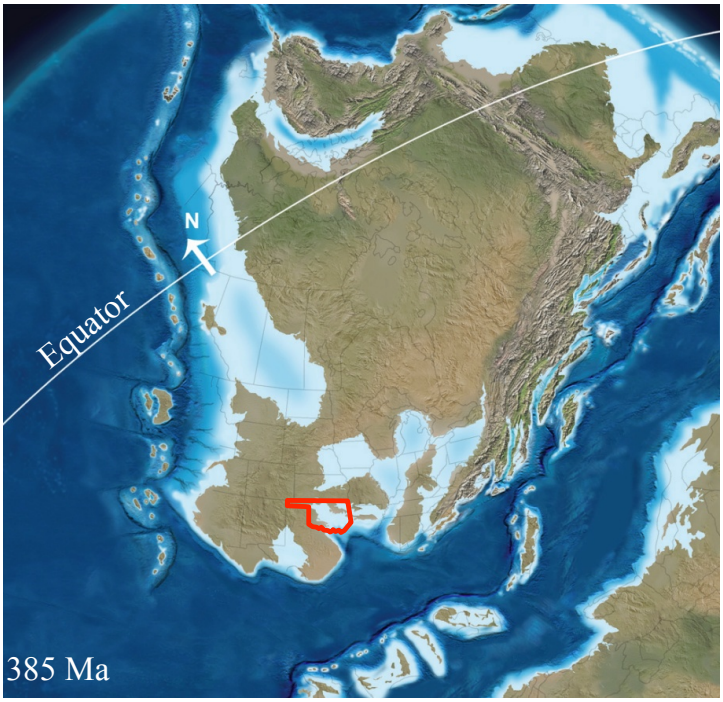

Figure 57: Paleogeography of North America at the beginning of late Devonian (Frasnian). Paleo-location of Oklahoma is marked with red line. Figure is modified from Comer, 2008.

Available Data

This analysis is based on detailed analyses of two subsurface cores (well 1 and well 3) from both hydrocarbon producing and non-producing wells coupled with field data from a number of wells that will be used to understand the geologic history of the studied area. Visual core descriptions along with thin sections were analyzed for petrographic analyses. Pieces of the core were also analyzed under Scanning Electron Microscope (SEM). High-resolution sampling (roughly 2 ft sampling interval) was done for petrophysical measurements including mineralogical composition through FTIR technique, porosity, Φ_{He}, through LPP (low pressure porosimetry) method, bulk density, ρ_b, grain density, ρ_g, mercury injection capillary pressure curve, total organic carbon

content, TOC through LECO method, and rock-eval pyrolysis. Acoustic velocities (one P- and two S-wave velocities) as well as nuclear magnetic resonance, NMR, measurements were made were performed on 82 horizontal plugs. The TOC and rock-eval measurements were collected at the Weatherford laboratories while rests of the data were collected at the University of Oklahoma's Integrated Core Characterization Center (IC^3). Core gamma ray measurements were made by Terratek and provided by the operator. Wireline logs such as gamma ray, acoustic velocities (V_P, V_S), ECS, ρ_b, PEF, resistivity were also used in this study.

Lithofacies and petrographic characteristics

Overall, the Woodford Shale core appears from dark brown to black in color. I have identified 6 lithofacies based on visual description (Figure 58) of two subsurface cores: (1) black shale, (2) cherty, shiny black shale, (3) greyish shale, (4) yellowish-black shale, (5) highly organic rich shale and (6) yellowish grey shale. The black shale and shiny black shale facies constituted about 80% of the Woodford interval while minor presence of the remaining four lithofacies. Further analyses of different lithofacies were then performed through microscopic and sub-microscopic observations of these rocks. Thin sections of the black shales do not only provide a means for petrographic analyses but also to visualize megascopic sedimentary features which are otherwise impossible to recognize due to dark color of the studied rock. These megascopic features can then be correlated to microscopic and submicroscopic features seen by SEM analysis.

The framework elements of the studied rock are grouped into four primary components: (i) very fine clay matrix, (ii) silty particles, (iii) organic matter, and (iv) fractures. The silty material is composed of flattened Tasmenities cysts, mineralized

fossils (primarily Tasmenities cysts, along with some benthic foraminifera), detrital quartz and dolomite particles, and pyrite. Petrographic inspections of the dominant black shale facies further group this facies into two: fossil-rich mudstone and laminated mudstone (Figure 59). While both types of black shale are present in the two studied wells, well 3 contains much smaller amount of both the fossils and detrital silt-materials and greater quantity of clay. Measured mineralogy data also indicates that average clay content of well 1 is 40 wt.% and of well 3 is 60 wt.% (as described in chapter 1 of this thesis). Petrographic observations also reveal that Tasmenities are present throughout the Woodford interval and served as primary source of organic matter in the study area. Tasmenities were mineralized to different extent depending on the availability of silica with dissolution of radiolarians serving as the primary source of silica (Schieber, 1996).

In some intervals the lamination of the black shale facies is completely destroyed by bioturbation activity. Bioturbated intervals could easily be identified through mottled fabric, destroyed lamination (Figure 60a, and Figure 60b) distinguishable under petrographic microscope. Identification of bioturbated intervals on hand specimen is possible through careful inspection of water-wet surface (Figure 60c, and Figure 60d). Presence of pyrite streaks also indicates bacterial activity at the sediment-water interface that might have been flattened due to compaction. Pyrite is also present as nodules, pyritized microfossils as well as in the form of framboids. The cherty facies (second dominant lithology) is present at many scales, ranging from lamina to beds to layer. The irregular boundary of this lithofacies at any scale indicates that deposition of this lithofacies was associated with some kind of current action (Figure 62). Other

sedimentary structures in the studied rock include: fining upward sequences (Figure 61), slump structures (Figure 63), and fractures.

The Woodford Shale is affected by both natural and drilling induced fractures (Figure 64) with natural fractures identified by the presence of authigenic minerals. Natural fractures are present within the brittle cherty facies while no natural fractures could be distinguished within the ductile black shale facies. Natural fractures vary in orientation (vertical to near horizontal), filling material (such as: dolomite, silica, pyrite) and also filling property (completely filled versus partially filled). Deformed nature of both fractures (Figure 64a) and adjacent host layers indicate these fractures were developed prior to complete lithification of the unconsolidated sediments. Comer (2008b) proposes these dolomite filled fractures to be possible hydrocarbon primary migration pathways that probably were generated during hydrocarbon generation. Figure 58 is a representative image showing the fracturing intensity, which made it impossible to collect core plugs over highly fractured/broken areas. Mineralogy data (Figure 65) indicates that overall, well 3 has higher clay content and are less fractured compared to well 1 that has lesser amount of clay and is broken into pieces at many intervals (Figure 58). Mineralogy data (Figure 65) also indicates fracture intensity (Figure 58) increases in areas with higher amount of brittle minerals (quartz, carbonates for example). Within well 1, the presence of dolomite filled fractures subdivide the lower Woodford (LW) interval into a lower, highly fractured interval and an upper interval with lower fracture intensity. The lower interval is badly broken due to dense silica-filled fractures, which may have been enhanced by the drilling activity. There were fewer natural and induced fractures present in the upper part of the LW, which contains comparatively higher clay content compared

to the lower part. Most of the middle Woodford (MW) is characterized by medium fracture intensity. At the base of MW very few fractures were present followed by a 10 ft thick missing interval. Medium fracture intensity is observed in X0570ft-X0605ft, followed by high fracture intensity above. Only part of the upper Woodford (UW) was present in this core. The UW was highly fractured (both natural and drilling induced) for much of the interval such that core was not recovered in several intervals. The black shale facies present near the very top had very few fractures.

No pore spaces are visible through petrographic microscopic observation owing to the nanometer-scale characteristic pore size (as described in chapter 2 of this thesis). SEM imaging has revealed organic pores as the most common pore types in the studied shale (Figure 66).

The rich diversity of sedimentary features illuminated through these multi-scale analyses indicates a range of geologic processes during Woodford deposition. All of these petrographic and lithologic characteristics observed at multiple scales are used to investigate the depositional history and stratigraphic changes during the Woodford Shale deposition.

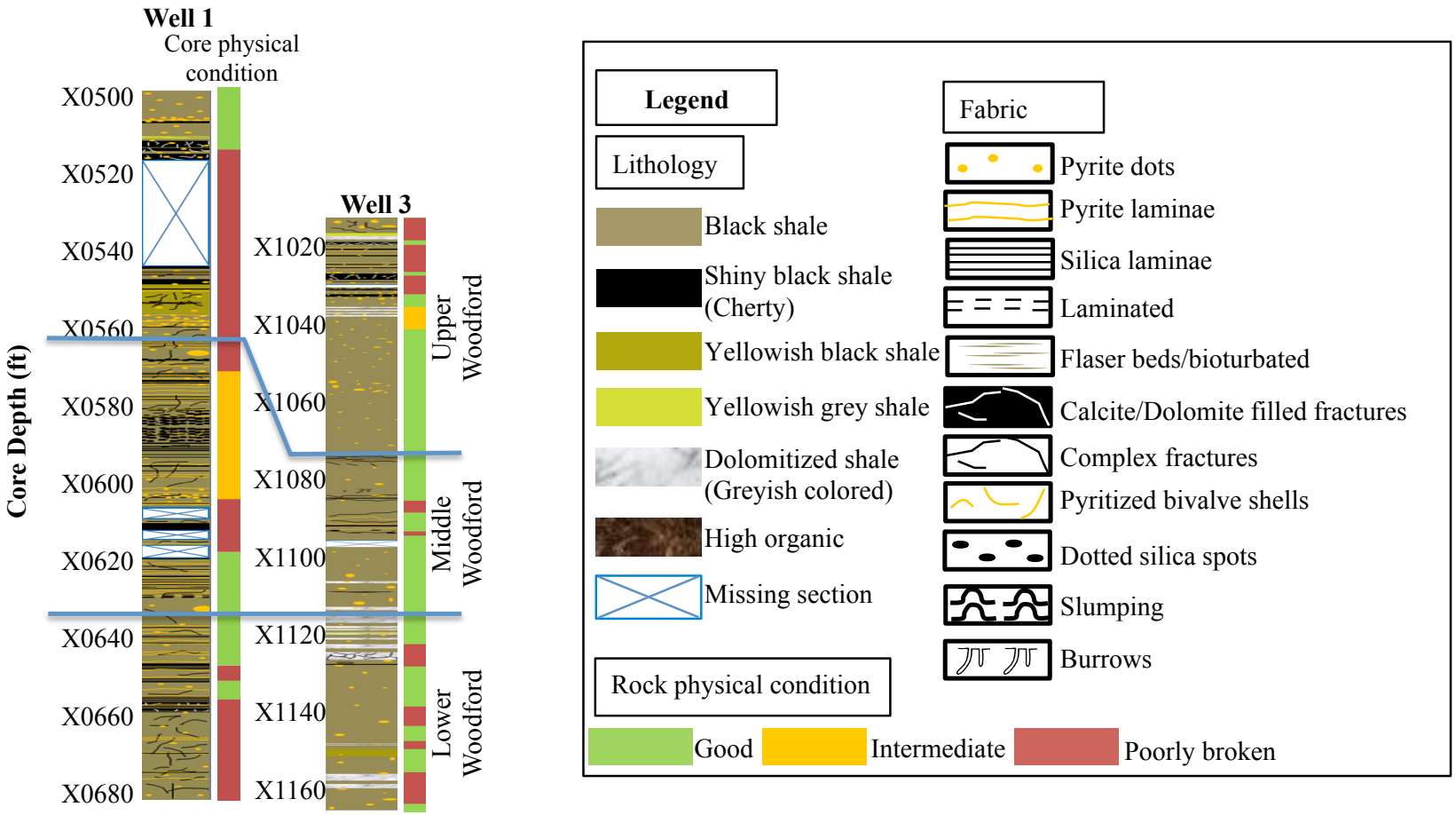

Figure 58: Schematic core description of wells 1 and 3.

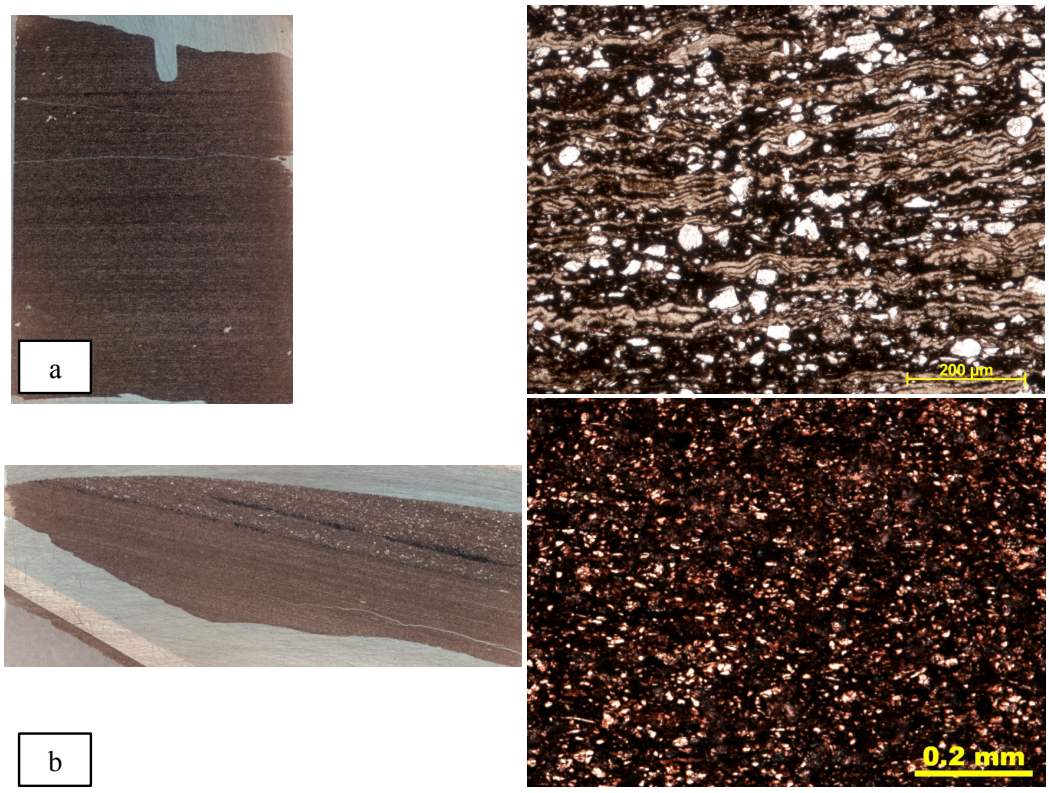

Figure 59: Two types of black shale: (a) organic rich shale, and (b) laminated shale. High-resolution scan of the thin section is shown on the left and photomicrograph under plane polarized light is shown on right.

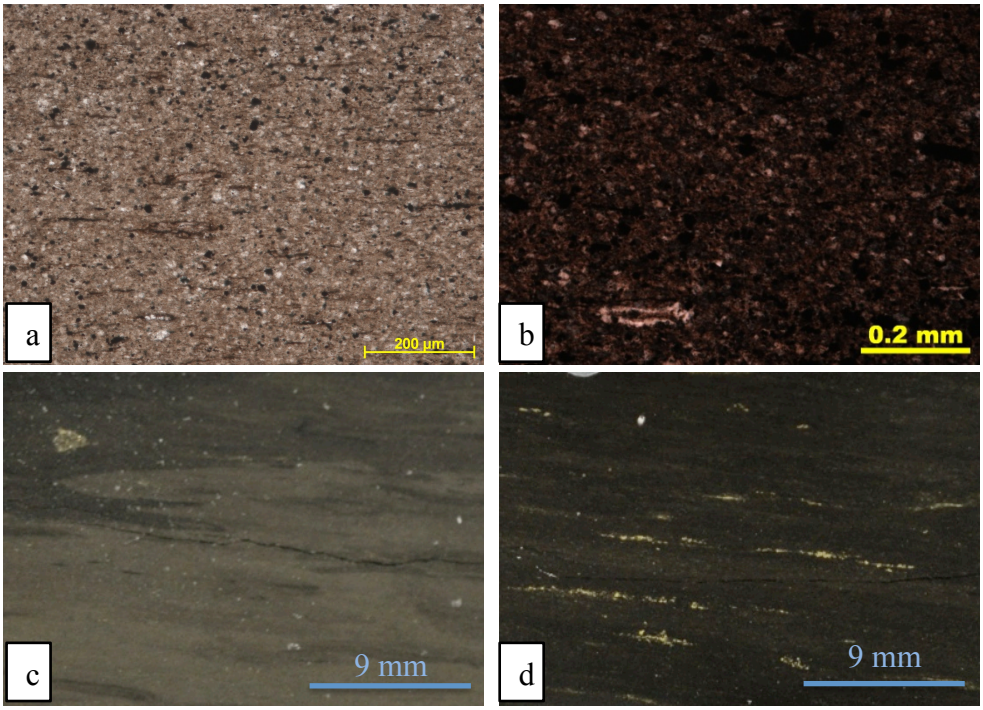

Figure 60: Photomicrograph under plane polarized light showing mottled fabric of highly bioturbated samples from well 1 (a) and well 3 (b). (c, d) Water-wet surface of core showing bioturbated rocks in hand specimen. These features are distinguishable on water-wet surface of the sample and through enhancing the contrast of the picture.

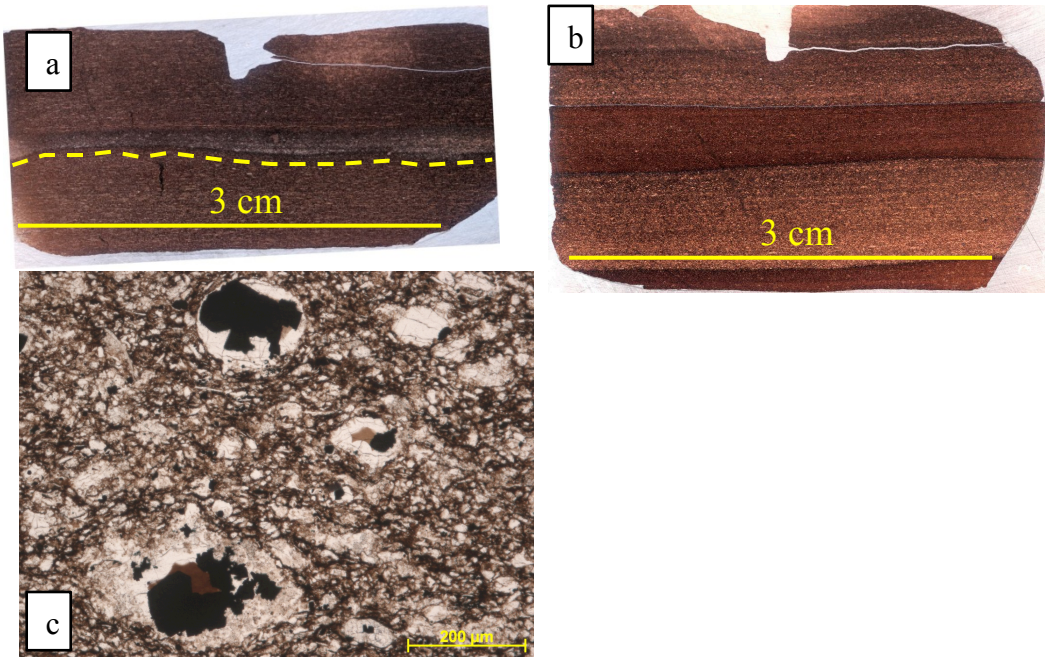

Figure 62: (a, b) High resolution scan of thin sections showing different thicknesses of the cherty lithofacies. The millimeter thick cherty layer is highlighted by yellow dashed line on Figure 9a. (c) Photomicrograph under plane polarized light showing the cherty facies.

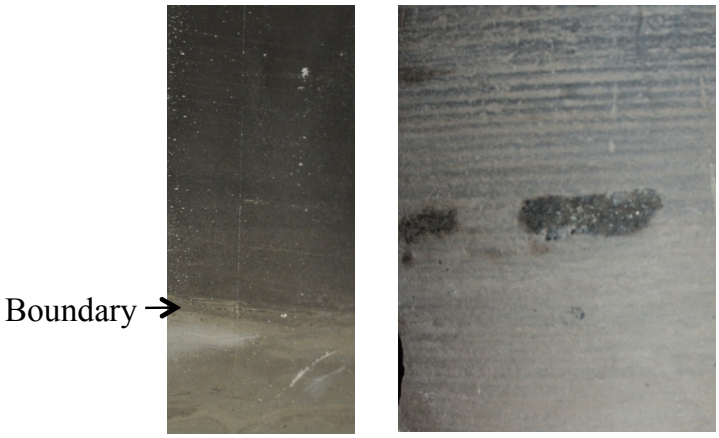

Figure 61: Picture of the water-wet hand specimen showing boundary between the underlying bioturbadated mudstone and overlying black shale. A fining upward sequence can be observed just above the boundary. Presence of pyrite rich clay clasts (shown in the figure on right) at this boundary possibly indicative of transgressive lag.

Figure 63: Slump visible at the high resolution scanned image of a thin section.

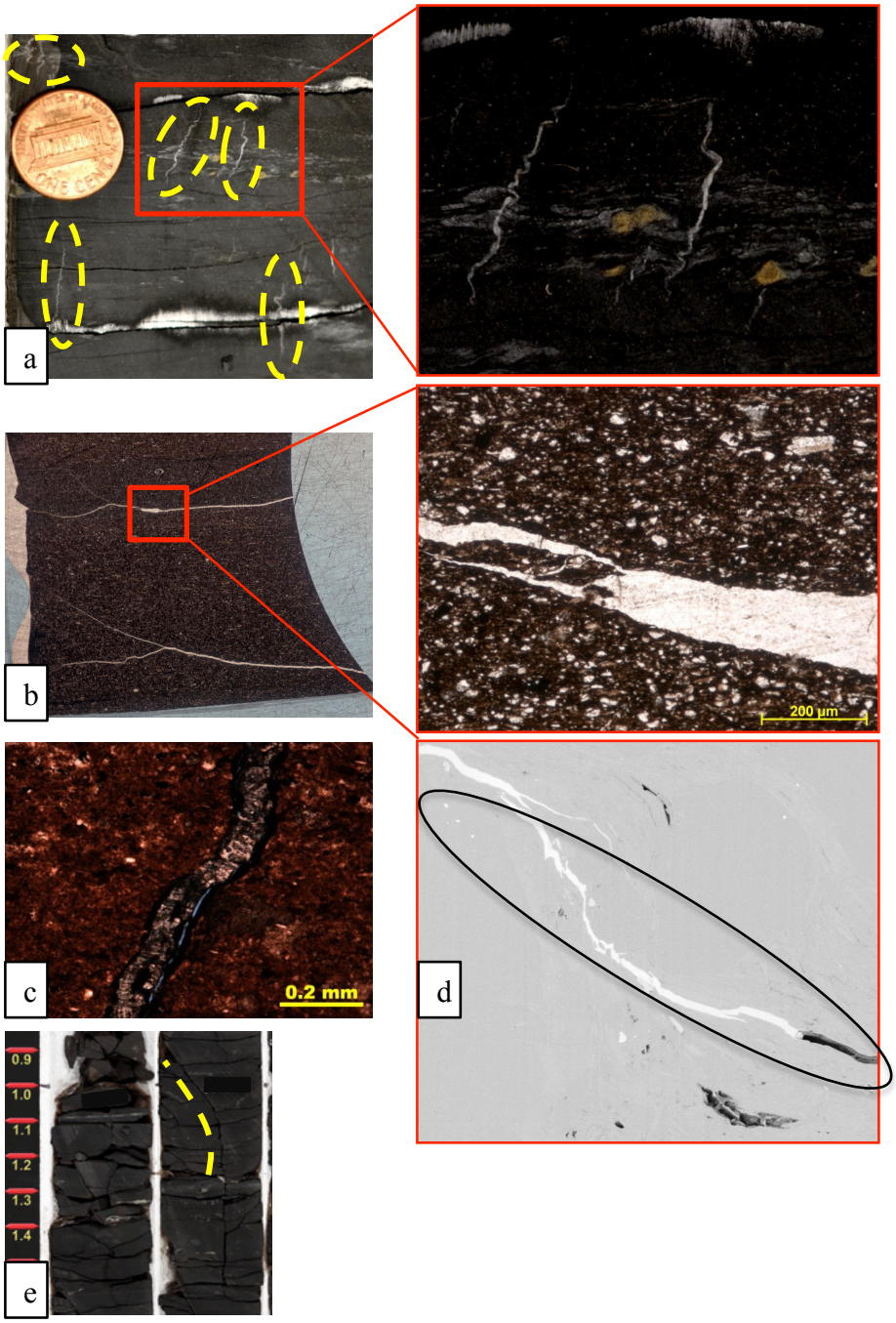

Figure 64: (a) Picture of a piece of core showing almost vertical dolomite filled natural fracture, (b) Images of a thin section showing low angle dolomite filled natural fractures, (c) Thin section showing partially filled natural fracture, (d) SEM image showing pyrite filled natural fracture highlighted by ellipse, (e) Picture of a core. Yellow line highlights drilling induced natural fracture.

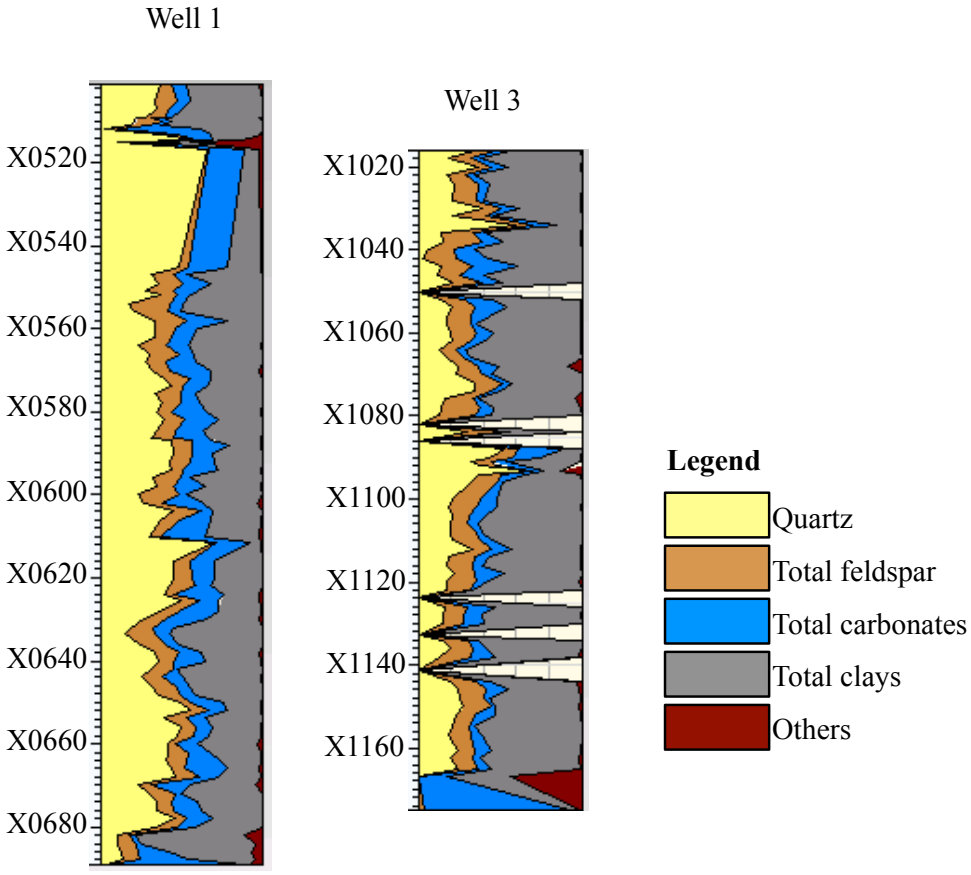

Figure 65: Mineralogic variations with depth for wells 1, and 3 showing that well 3 has higher clay content compared to well 1.

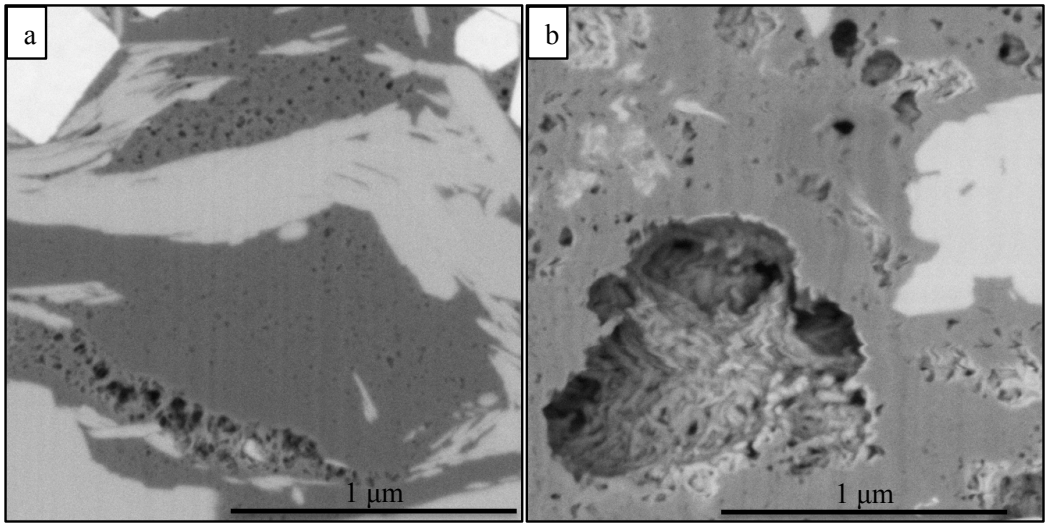

Figure 66: FIB-SEM images of samples from well 1 (a), and well 3 (b) showing organic pores which are the most common pore types in the studied rock. Dark grey areas indicate organic matter, darker areas within the organic matter indicate pores within the organic matter.

Depositional history

The overall silty nature, random orientations of clay and silt grains, disrupted shale laminae, episodic storm deposits identified through episodic thin alternating layers of clay and silt lamina suggests episodic sedimentation) (Figure 59) indicate Woodford deposition occurred above storm-weather wave-base, probably within a shallow-shelf depositional environment. Petrographic analyses and petrophysical properties coupled with the knowledge about the paleogeography of North America (Comer, 2008a) indicate that the Woodford Shale was deposited in an epeiric sea during a eustatic sea-level rise punctuated by a number of higher order depositional cycles. Arid paleoclimate, indicated by the south 15° latitudinal position of North America, limited the amount of detrital supply to the basin, which resulted into high clay concentration in both near shore and far offshore areas (Comer, 2008a). The slow rate of deposition (50Ma represented within 200ft rock record) results in high frequency variations in the lithostratigraphic column

which means thin intervals of rocks represent individual depositional cycles. Moreover, the fine-grain nature, and overall dark color reduce the ability of proper sampling for tracking the record of all the depositional cycles. Mineralogy seems to be one of the primary parameters changing in response to geologic processes and sea-level changes. Overall, the mineralogical constituents are: 10%-50% quartz except few samples from cherty intervals where the quartz component approaches to 70%, 0%-20% feldspar, 3%-32% total carbonate, 20%-60% total clays and 0%-14%% other minerals which include anhydrite, apatite and pyrite (Figure 65 and Figure 67). Illite is the dominant clay minerals in both the wells which correspond to the high thermal maturity ($450°C<T_{max}<500°C$) of the studied rocks. However, the complex nature of lithostratigraphic changes indicates that no one parameter can adequately be used to track the depositional history. Among a set of petrophysical properties collected for this study, positive changes in bulk density correlate with increase in clay content or rather, more specifically increase in illite content (illite is the most dominant clay types in both the wells) and a general decrease in quartz content. Such changes in bulk density also matches with significant changes in the lithologic unit, as observed through microscopic and sub-microscopic observations of samples collected from frequent depth intervals. Hence, I have used positive changes in bulk density in combination with other petrophysical parameters to recognize 14 depositional cycles within the Woodford interval with lower Woodford having 6 (named as LW1 through LW6 from base to top), middle Woodford having 4 (named as MW1 through MW4 from base to top) and the upper Woodford having 4 (named as UW1 through UW4 from base to top) cycles in well 1. Well 3 has a comparatively thinner Woodford and individual Woodford members

contain 5, 4, and 4 depositional cycles from base to the top respectively. In the studied wells, the LW, MW and UW are 58.4ft, 75.8ft, and 59.2ft thick respectively in well 1 and 45 ft, 38 ft, and 57 ft in well 3 respectively (Figure 68). Photomicrographs indicate increasing bioturbation, presence of cherty facies near the top of most of these depositional cycles. All of these including increasing gamma ray at the boundary of most of the depositional cycles indicate that there is a possibility that these depositional cycles are indicating parasequences within the study area. The three informal members (lower, middle and upper member) of the Woodford Shale have been identified based on the wireline log signatures and correlation to the other wells in the field.

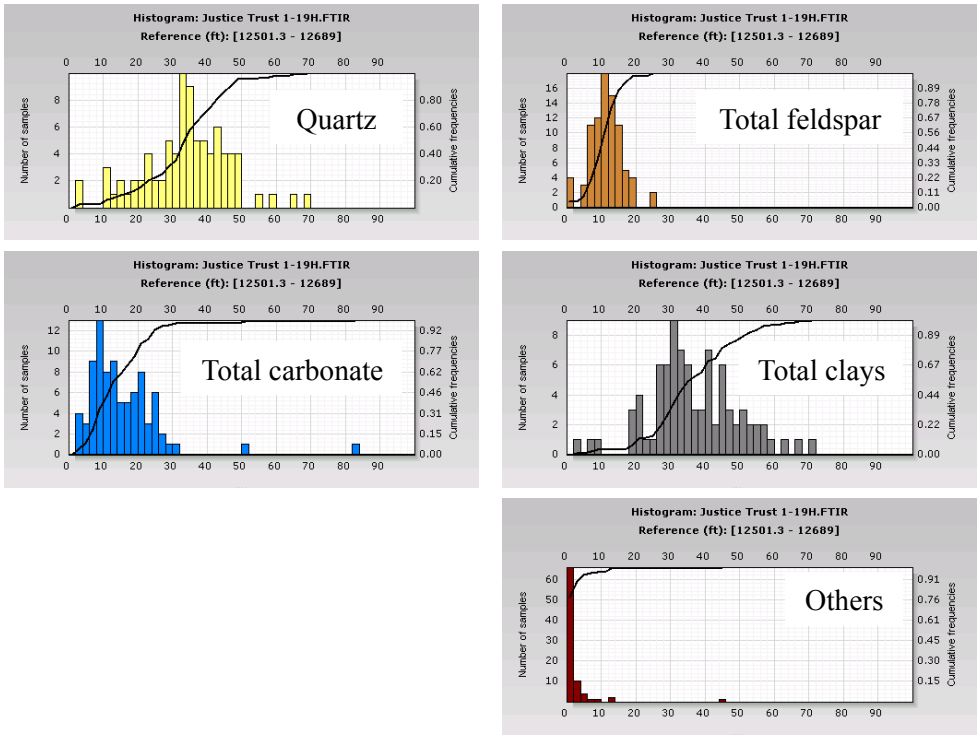

Figure 67: Histogram and cumulative frequencies of individual minerals shown in the depth plot in Figure 13.

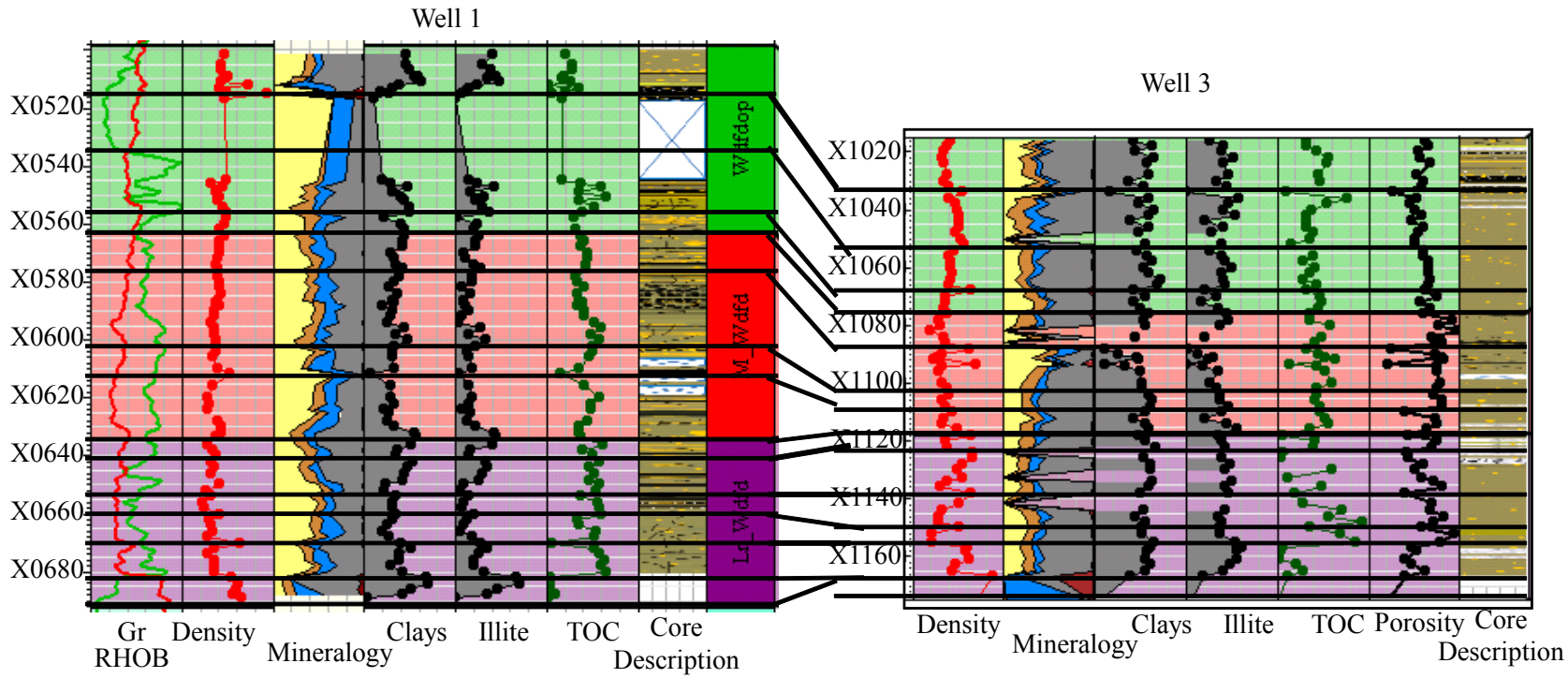

Figure 68: Depositional cycles for well 1 and well 3.

Lower Woodford

The base of the Woodford is defined by an unconformity and the sharp change from the limestone to black shale (Figure 69). Following is a brief description of each depositional cycles.

LW1: X0688.4 ft to X0680 ft in well 1. Total thickness: 8.4ft. This cycle is present in well 1 only. This is a unique cycle at the base of the Woodford, containing a carbonate turbidite at the top of this cycle. The upper boundary of this cycle is defined by sudden jump in quartz content, TOC, porosity and sudden drop in clay content. Randomly oriented, partially silica filled natural fractures are common in this cycle; highly broken rocks indicate more of such fractures. Few drilling induced fractures are also present.

LW2: X0680 ft to X0670 ft in well 1, X1167 ft to X1156 ft in well 3. The upper boundary of this cycle is marked by increase in bulk density and clay content. Photomicrograph suggests increase in bioturbation (Figure 60a) at the top of this depositional cycle.

LW3: X0670 ft to X0660 ft in well 1, X1156 ft to X1150 ft in well 3. The upper boundary of this cycle is marked by increase in bulk density and clay content. Like the cycle below, photomicrograph suggests increase in bioturbation at the top of this depositional cycle.

LW4: X0660 ft to X0650 ft in well 1, X1150 ft to X1138 ft in well 3. The upper boundary of this cycle is marked by increase in bulk density and clay content. Overall, high TOC and porosity values in well 1 and both TOC and porosity decreases upward in well 3.

LW5: X0650 ft to X0641 ft in well 1, X1138 ft to X1124 ft in well 3. The upper boundary of this cycle is marked by increase in bulk density and clay content. Again photomicrograph suggests increase in bioturbation at the top of this depositional cycle.

LW6: X0641 ft to X0633 ft in well 1, X1124 ft to X1117 ft in well 3. The upper boundary of this cycle is marked by increase in bulk density and clay content. Again photomicrograph suggests increase in bioturbation at the top of this depositional cycle. Upper boundary of this cycle matches with the boundary between the lower and the middle Woodford member and hence is traceable across the basin.

Middle Woodford

MW1: X0633 ft to X0618 ft in well 1, X1117 ft to X1110 ft in well 3. The upper boundary of this cycle is marked by increase in bulk density and clay content. Again photomicrograph suggests increase in bioturbation at the top of this depositional cycle.

MW2: X0618 ft to X0602 ft in well 1, X1110 ft to X1115 ft in well 3.

MW3: X0602 ft to X0578 ft in well 1, X1115 ft to X1091 ft in well 3. Photomicrograph from well 3 indicates period of non-deposition or formation of hard ground (Figure 70) near the top of this cycle.

MW4: X0578 ft to X0562 ft in well 1, X1091 ft to X1078 ft in well 3. The upper boundary of this cycle matches with the boundary between the middle and the upper Woodford and hence, is traceable throughout the basin.

Upper Woodford

The core was not recovered for part of the upper Woodford in well 1. Hence, the wireline bulk density is used to determine the depositional cycles in the upper Woodford.

UW1: X0562 ft to X0555 ft in well 1, X1078 ft to X1068 ft in well 3. Figure 71 shows high-energy current related deposit present just above the top of this boundary. The upper boundary of this cycle matches with the highest gamma ray count within the Woodford interval, indicating a flooding surface and the rock indicates a transgressive lag (Figure 71).

UW2: X0555 ft to X0526 ft in well 1, X1068 ft to X1051 ft in well 3.

UW3: X0526 ft to X0515 ft in well 1, X1051 ft to X1034 ft in well 3.

UW4: X0515 ft to top of the Woodford in well 1, X1034 ft to top of the Woodford in well 3. The base of this cycle indicates a regional slumping event (Figure 63) followed by shallowing of the water column. Characteristic feature of this unit include: bioturbated rock (Figure 72), fossil assemblages dominated by benthic organisms (for example, benthic foraminifera) (Figure 73).

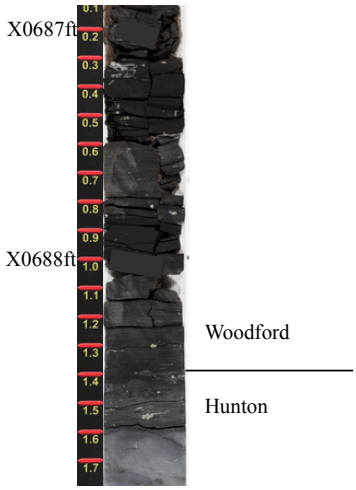

Figure 69: A piece of core showing the erosional unconformity between the Hunton Limestone and the overlying Woodford Shale.

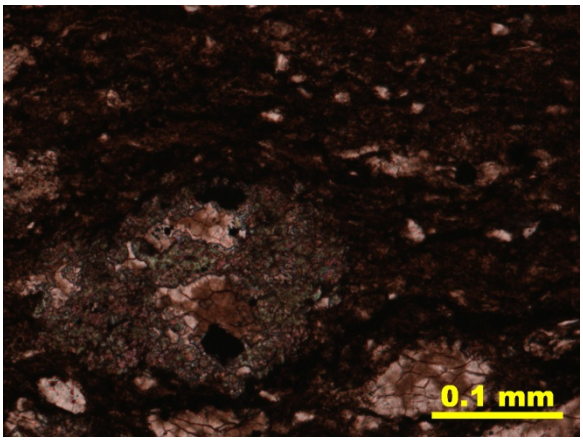

Figure 70: Photomicroph under plane polarized light showing hard ground present at X1091 ft in well 3.

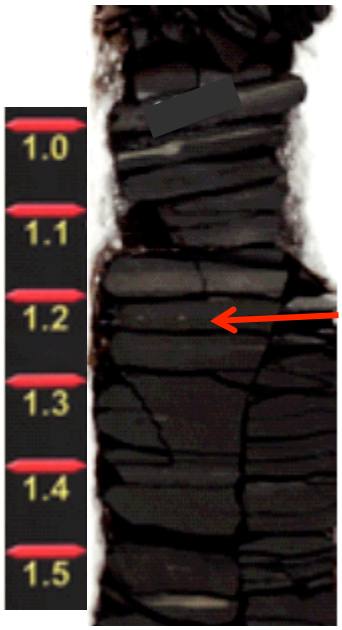

Figure 71: A piece of core showing the contact at X0555 ft in well 1(marked by red arrow).

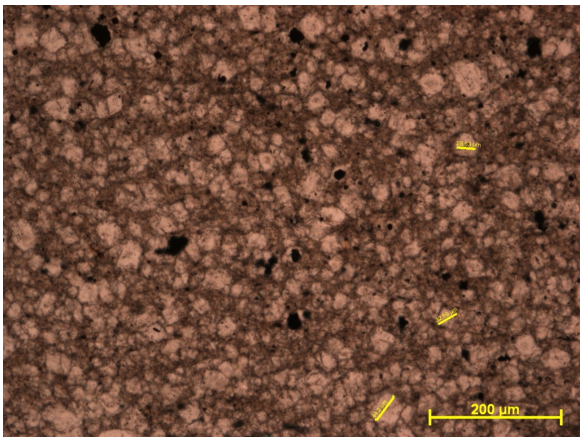

Figure 72: Photomicrograph of a sample from well 1 showing highly bioturbated, dolomitic layer (at X0511.8ft) under plane polarized light. Original laminations are completely disrupted by the bioturbation.

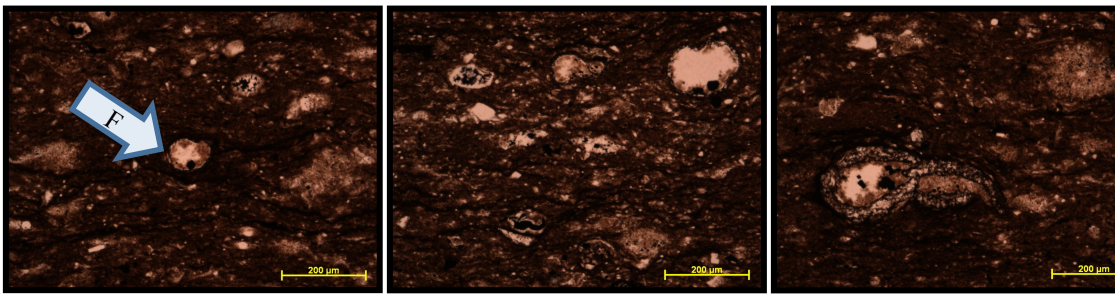

Figure 73: Photomicrographs of samples from well 1 indicate completely different fossil assemblage of the upper Woodford at X0513ft compared to the rest of the Woodford interval containing primarily algal laminae, Tasmenities spores etc. Agglutinated foraminifer is marked on the left figure with white arrow (F).

Correlation to the regional changes

Gamma ray (GR) is the most common tool used for the stratigraphic correlation across long distances. However, gamma-ray model by Paxton et al. (2006) suggested that high radioactivity in the resource shales might result from organic matter richness as well as slow sedimentation rate and association of uranium with clay minerals at the sediment water interface. Hence, GR correlation is dangerous for the resource shales except for very high peaks, which are likely to be related with big basin wide events and are expected to be present in any part of the basin. The Woodford Shale is characterized by overall high gamma ray and only few very high GR peaks correlatable across basins and most likely indicate global events. Johnson et al. (1985) proposed a eustatic sea-level curve for the late Devonian-early Mississippian time, which was later modified by Sandberg et al. (2002). The later developed modified sea-level curve and correlation between well 1 to the Amis 1-3 well have been used to identify sea-level changes in the study area. Figure 74 contains the descriptions of the 18 late Devonian events, as described by (Sandberg et al., 2002). Paxton et al. (2006) correlated the gamma ray from the Amis 1-3 well with the eustatic sea level curve by Johnson et al. (1985). Figure 75 shows the locations of the wells used in this study. Paxton et al (2006) correlated the base of the Woodford Shale with the Tahini onlap. Both correlations to the eustatic sea-level and petrographic analyses that broadly the lower Woodford (LW) was deposited at earlier part of transgression, middle Woodford (MW) was deposited when the transgression reached the maximum. At the upper Woodford (UW) time the sea level began to fall. Lambert (1993) also concluded (based on regional work) that the lower, middle, and upper shale members of the Woodford and Chattanooga represent the transgressive and

early and late highstand systems tracts of the sequence. The highest gamma ray peak near the MW-UW boundary probably matches with the maximum flooding surface (MFS) and is the highest Gr peak within the Woodford interval in all the studied wells (well 1, Amis 1-3 and Wyche-1) (Figure 76). The slumping event in the upper Woodford (UW4) is correlated with the period of collapse of shelf margin at event 11 in the eustatic sea-level curve. The high TOC content of UW4 matches with the post-biotic radiation reported at the event 12 on the eustatic sea-level curve.

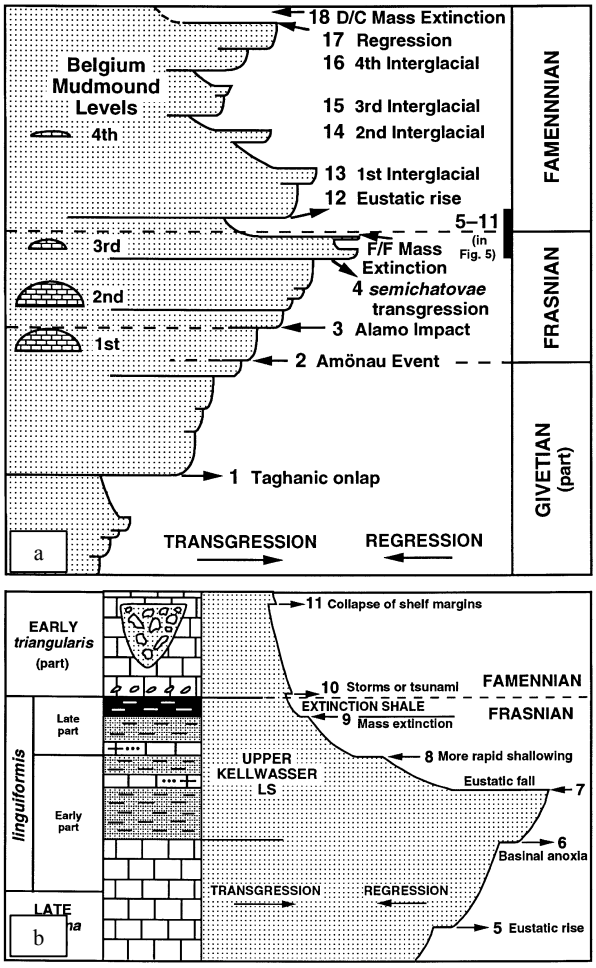

Figure 74: Eustatic sea-level curve during late Devonian time and associated events proposed by Sandberg et al., 2002.

No. of events	c Event Descriptions
18	Late Famennian mass extinction within eustatic fall; loss of many Devonian species including Lazarus fauna
17	Start of major eustatic fall at climax of Southern Hemisphere glaciation; biotic decline begins
16	Eustatic rise at start of 4th interglacial episode; Etroeungt Lazarus fauna suddenly appears in Northern Hemisphere
15	Eustatic rise at start of 3rd interglacial episode; annulata black basinal shales deposited in Germany
14	Eustatic rise at start of 2nd interglacial episode; Baelen mudmound formed in Belgium
13	Eustatic rise at start of 1st interglacial episode; Cheiloceras dark shales deposited
12	Eustatic rise, producing initial post-extinction biotic radiation
11	Carbonate-platform margins collapse due to glacioeustatic lowering of seas; widespread coarse tsunamite breccias result
10	Storms and (or) tsunami scour or remove Frasnian-Famennian boundary beds in France, Germany, and Nevada
9	Late Frasnian mass extinction within eustatic fall; widespread layer of abiotic extinction shale deposited; start of Southern Hemisphere glaciation
8	Rapidly increased shallowing; storm deposits; stepwise extinction of some deep-water species as shallow-water species move into deeper water; spore floras change
7	Eustatic fall; start of global cooling; reduction in number and diversity of deep-water faunas
6	Continued eustatic rise; stratification of water column, resulting in widespread basinal anoxia; start of rapid evolution of deep-water entomozoan ostracods
5	Eustatic rise producing dysoxia in deep basins; start of events leading to mass extinction
4	Major semichatovae transgression producing biotic changes and stress
3	Alamo Impact in Nevada, coinciding with eustatic rise and demise of 1st level of Belgian mudmounds
2	Amo¨nau Event, coinciding with onset of impact-induced(?) volcanic activity in central Germany and with eustatic rise at start of Frasnian
1	Taghanic onlap at start of plate-tectonic movements in Northern Hemisphere; end of faunal provincialism

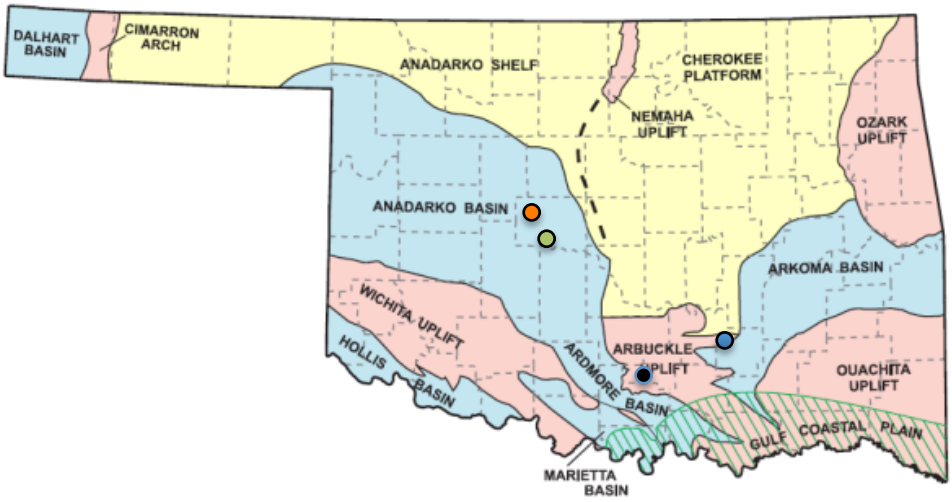

Figure 75: Major geologic provinces of Oklahoma shown by different colors (modified from Johnson et al., 2010) with dots showing the well locations used in this study. Red, and green dots indicate two cored wells, well 1 and well 3 respectively. Black dot indicates Amis 1-3 well, and blue dot indicates Wyche well; both located near the Arbuckle uplift.

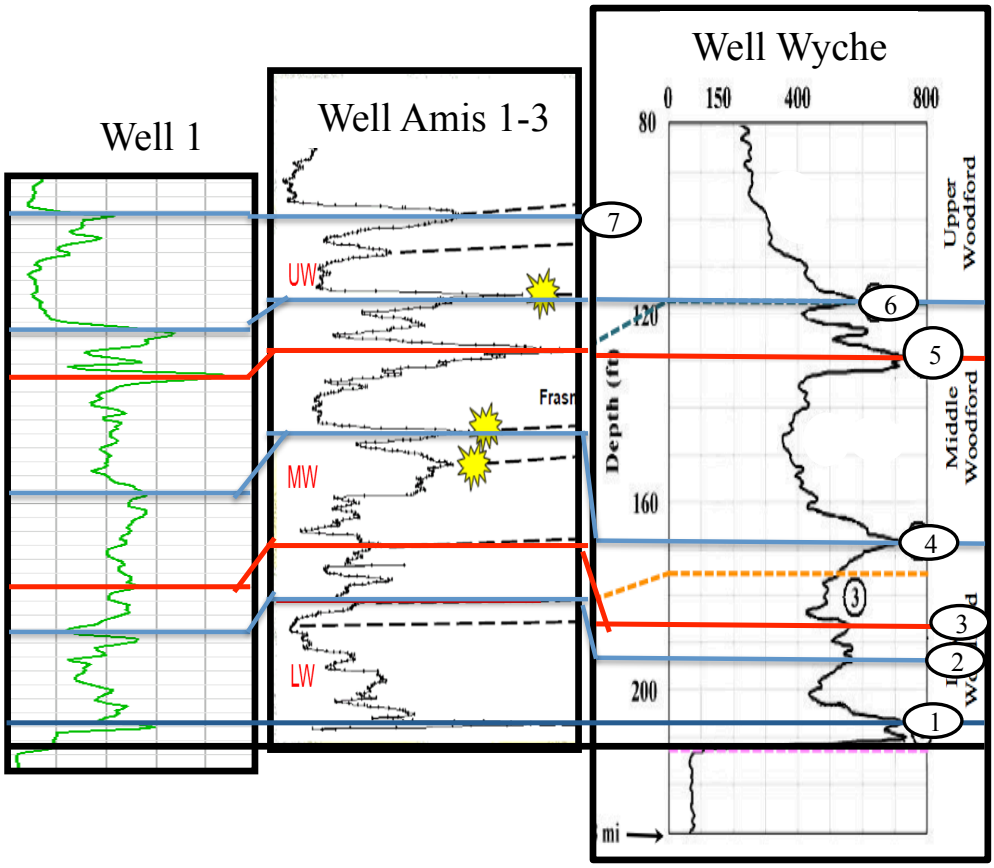

Figure 76: Gamma-ray correlations. Blue dashed lines are correlation lines, the numbers are the correlated points. Red correlation lines are the boundaries between lower-middle Woodford and middle-upper Woodford respectively. The boundary between LW and MW was originally placed at correlation point 2, in the Amis 1-3 well, in the original paper (Paxton et al., 2006).

Depositional model

Seismic data indicates that the Woodford deposition took place on a very irregular surface (Geophysics paper) of the Hunton Limestone. Comparatively depression areas on the Hunton Limestone were inundated earlier and the remnant highs were inundated at later stage of the Woodford deposition and contain comparatively thinner Woodford Shale. Overall thin Woodford interval along with missing lower most depositional cycle in Well 3 indicates that the Woodford deposition started later in well 3 compared to well 1. Hence, the Woodford deposition started later in the well 3 compared to well 1 and also well 3 is located in one of the remnant highs on the basin floor. Well 1 contains both the black shale lithofacies and the brittle cherty lithofacies, which was associated with high-energy flow. Such high-energy flow might have resulted from a number of events, for example, storm related current, debris flow all of which preferably followed the depressions on the basin floor. Little presence of the cherty facies in well 3 also supports the location of the well 3 on a local basin floor high. Seismic attribute analysis indicates that the depressions on the basin floor are characterized by high curvature values, collapse features (low similarity values), all potentially indicating zones of natural fracture concentrations. Highly fractured well 1 compared to less fractured well 3 again confirms the relative locations of these two wells on the basin floor. Based on these observations, following is a proposed depositional model for the Woodford shale (Figure 77). The core from well 3 indicates frequent bioturbated interval indicating lot more benthic organic activities compared to well 1.

The organic matter in the Woodford Shale is sourced from highly mobile planktonic organisms (for example, Tasmenities, radiolarian etc.). Intermediate basin

locations, typical areas for upwelling are likely to have high population of such organic matter and are potential areas for higher amount of hydrocarbon accumulation. The upper Woodford member is expected to be highly organic rich in deeper part of the basin as eustatic sea-level curve indicates a major sea-level drop at this stage of the Woodford deposition, making the deeper part of the basin likely areas for upwelling, nutrient supply and planktonic organic matter concentrations.

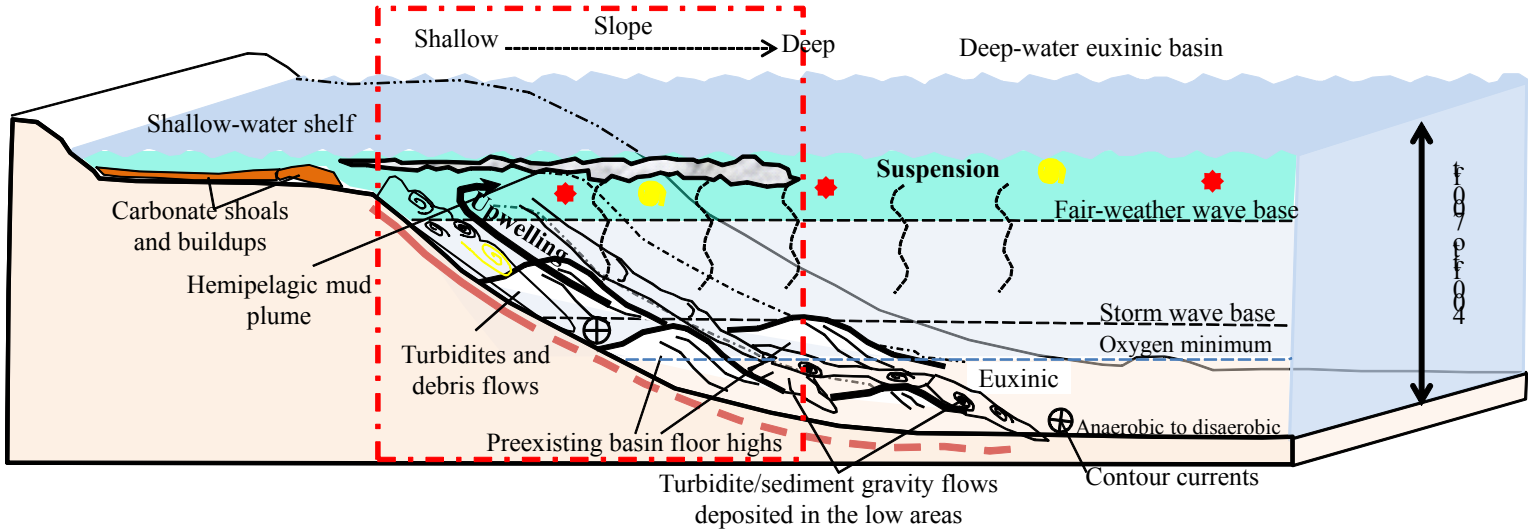

Figure 77: Proposed depositional model for the Woodford Shale.

Conclusions

The Woodford Shale recorded a prolonged period of complex and variable sedimentation. Paleo-climate and physiogeographic conditions allowed very little terrigeneous input, and provided a warm climate and upwelling resulting in high biologic productivity. These three factors favored the deposition of an organic rich black shale. Restricted terrigeneous input allowed high concentration of clay even in the shallow part of the basin. Petrographic observations provide the ground truth for tracking the sedimentologic changes and then to identify the critical petrophysical parameters, which can be used in the uncored wells to track such changes. Petrographic analyses need to be performed at microscopic and sub-microscopic scales; very little can be seen megascopically due to dark color and fine-grained nature.

Both petrographic observations and petrophysical properties indicate the cyclic nature of the Woodford deposition. Such cyclic deposition resulted into alternating cherty facies and TOC-rich ductile rock. Most of the depositional cycles are comprised of a lower organic-rich, high gamma-ray interval, and cherty facies near the top. This provides the brittle-ductile rock couplet critical for the exploration within the resource shale.

Good correlations between changes in bulk density, clay content, TOC and actual rock architecture indicate that it is possible to track the fine-scale stratigraphic changes using the petrophysical proxies in the uncored areas.

Depositional history indicates that the Woodford Shale was deposited on top of the irregular unconformity surface that controlled the accumulation of the Woodford Shale in local scale. Basin floor topography controlled thicker Woodford accumulation in

depression areas and thinner Woodford in areas of basin floor highs. This also indicates that thickness of the Woodford Shale may vary over considerably small distances, as seen in well 1 and well 3. Moreover, basin floor depressions are areas likely to receive any high-energy turbidity current related deposits compared to basin floor highs, which receive only the suspension fall-out. Basin floor highs are the areas for clay-rich sediments, which can have high TOC but contain limited cherty facies, which provides brittleness critical for initiating fractures within these rocks.

Presence of frequent high-energy deposits indicate that the Woodford Shale was deposited above storm wave base (tens of meters) in the study area. High organic productivity and deposition of the huge organic ooze maintained low oxygen or reducing conditions. This has favored the thick accumulation of the Woodford Shale.

References

Bjolykke, K., 1998, Clay mineral diagenesis in sedimentary basins-a key to the prediction of rock properties. Examples from the North Sea Basin: Clay minerals, v. 33, p. 15-34.

Cardott, B. J., and M. W. Lambert, 1982, Thermal maturation by vitrinite reflectance of Woodford Shale, Anadarko basin, Oklahoma: AAPG Bulletin, v. 69, p. 1982–1998.

Comer, J., B., 2008a, Distribution and Source-Rock Characteristics of Woodford Shale and Age-Equivalent Strata: AAPG Annual Convention and Exhibition.

Comer, J., B., 2008b, Reservoir characteristics and production potential of the Woodford Shale: World Oil, v. 229.

Comer, J. B., 1992, Potential for producing oil and gas from the Woodford Shale (Devonian-Mississippian) in the southern mid-continent, USA, Medium: X; Size: Pages: 574 p.

Fertl, W. H., and G. V. Chilingarian, 1990, Hydrocarbon resource evaluation in the Woodford shale using well logs: Journal of Petroleum Science and Engineering, v. 4, p. 347-357.

Gier, S., 2000, Clay mineral and organic diagenesis of the Lower Oligocene Schoneck Fishshale, western Austrian Molasse Basin: Clay minerals, v. 35, p. 709.

Hester, T. C., and J. W. Schmoker, 1983, Tectonic Controls on Deposition and Source-Rock Properties of the Woodford Shale, Anadarko Basin, Oklahoma—Loading, Subsidence, and Forebulge Development: US Geological Survey bulletin.

Hester, T. C., J. W. Schmoker, and H. L. Sahl, 1990, Log-derived regional source-rock characteristics of the Woodford shale, Anadarko Basin, Oklahoma.

Johnson, K. S., 1988, Geologic evolution of the Anadarko basin, in K. S. Johnson, ed., Anadarko basin Symposium: Circular 90, Oklahoma Geological Survey, p. 3-12.

Kvale, E. P., and B. Coffey, 2010, Depositional Model for the Devonian Woodford Shale, SE Oklahoma, USA: AAPG Annual Convention and Exhibition.

Lambert, M. W., 1993, Internal stratigraphy and organic facies of the Devonian-Mississippian Chattanooga (Woodford) Shale in Oklahoma and Kansas: Source rocks in a sequence stratigraphic framework: AAPG Studies in Geology, v. 37, p. 163–176.

Passey, Q. R., K. Bohacs, W. L. Esch, R. Klimentidis, and S. Sinha, 2010, From Oil-Prone Source Rock to Gas-Producing Shale Reservoir - Geologic and

Petrophysical Characterization of Unconventional Shale Gas Reservoirs, International Oil and Gas Conference and Exhibition in China, Beijing, China.

Paxton, S. T., A. M. Cruse, and A. M. Krystyniak, 2006, Detailed Fingerprints of Global Sea-level Change Revealed in Upper Devonian / Mississippian Woodford Shale of South-Central Oklahoma: AAPG Annual Meeting.

Raucsik, B., A. Varga, Z. Hartyêni, and V. Szilêgyi, 2002, Changes in Facies, Geochemistry and Clay Mineralogy of a Hemipelagic Sequence (Pliensbachian-Toarcian, Mecsek Mts., S Hungary) - a Possible Palaeoenvironmental Interpretation: International Geological Journal, v. 53, p. 5.

Sandberg, C. A., J. R. Morrow, and W. Ziegler, 2002, Late Devonian sea-level changes, catastrophic events, and mass extinctions, in C. Koeberl, and K. G. MacLeod, eds., Catastrophic Events and Mass Extinctions: Impacts and Beyond: Geological Society of America Special Paper 356, Geological Society of America, p. 473–487.

Schieber, J., 1996, Early diagenetic silica deposition in algal cysts and spores; a source of sand in black shales: Journal of Sedimentary Research, v. 66, p. 175-183.

Schieber, J., and W. Zimmerle, 1998, Petrography of shales: A survey of Techniques, in J. Schieber, W. Zimmerle, and P. Sethi, eds., Shales and Mudstones: Petrography, Petrophysics, Geochemistry, and Economic Geology, v. 2, Schweizerbart'sche Verlagsbuchhandlung, p. 3-12.

Sloss, L. L., 1963, Sequences in the Cratonic Interior of North America: Geological Society of America Bulletin, v. 74, p. 93-114.

Sullivan, K. L., 2006, Organic facies variation of the Woodford Shale, in western Oklahoma, The University of Oklahoma.

Chapter 5

Conclusions

Detailed analysis of cores collected from different end members are critical for understanding the characteristics of the resource shales and track major changes affecting the rock physical and chemical properties. Such analysis also helps to recognize critical petrophysical parameters affecting the rock properties. Analysis of a set of petrophysical properties indicate that quartz and clays along with TOC and porosity are good for identifying different petro-types within the Woodford Shale in the study area. TOC and porosity are correlated with reservoir quality and thus are critical for evaluation of any self-sustained resource shale. The highly quartz rich cherty rocks, although characterized by poor reservoir quality (low porosity, low TOC), provide the brittleness needed to initiate hydraulic fracturing for producing hydrocarbon. Rocks with intermediate clay and quartz content indicate the best reservoir rocks where TOC shows subtle increasing trend with increasing quartz. However, overall ductile nature of the TOC rich rocks (indicated by elastic moduli) demand intervening brittle rocks in order to initiate hydraulic fracturing and produce hydrocarbon from the apparently ductile and hydrocarbon rich intervals.

Microstructural analysis through high magnification SEM imaging reveals most of the pore spaces lie within organic matter (organic pores). Modal analyses of organic pores visible on SEM images and laboratory-measured porosity also indicate good correlation. Organic pores increases with increasing thermal maturity. However,

distributions and development of such pores are controlled by the relative distributions of different forms of organic carbon, such as: extractable organic carbon, convertible carbon and residual organic carbon.

Attributed assisted seismic stratigraphic and geomorphologic analyses indicate that the Woodford Shale was deposited on a very irregular surface controlling both lateral and vertical distributions of different petro-types. Sequential seismic geomorphologic analyses indicate stratigraphic changes during the Woodford deposition. A set of seismic attributes (coherent energy, mu-rho) highlights the distributions of ductile clay-rich rocks and comparatively brittle quartz-rich rocks at different level of Woodford deposition. Petrophysical properties extracted through simultaneous inversion of the pre-stack seismic data promises for petro-typing at regional scale.

Geologic history indicates that the Woodford Shale was deposited as organic rich black shale aided by a number of palaeo-climatic and palaeo-geographic conditions. Petrographic analyses indicate that planktonic organisms were the primary source of organic matter within the Woodford Shale. Both petrographic observations and petrophysical properties indicate cyclic nature of the Woodford deposition. Presence of frequent high-energy deposits indicate that the Woodford Shale was deposited above storm wave base (tens of meters) in the study area. Good correlations between bulk density, clay content, TOC and actual rock architecture indicate that these parameters can be used as proxies to track fine-scale stratigraphic changes. The upper part of the upper Woodford member records major changes in the depositional history, starting with slumping, followed by shallowing of the Woodford sea and then again a gentle sea-level rise indicating a possibility of TOC-rich upper Woodford in the deeper part of the basin.

The slumping event is correlatable with the global event of storm-tsunami and collapse of shelf margin.